

# Broadband Acoustic Liner Optimization Study Using Novel Poro-Elastic Materials

Kelsey Mitchell

Thesis submitted to the faculty of the  
Virginia Polytechnic Institute and State University  
In partial fulfillment of the requirements for the degree of

Masters of Science

In

Aerospace Engineering

Christopher R. Fuller, Chair

Michael Philen, Co-Chair

Doug Nark

Todd Lowe

May 5<sup>th</sup>, 2015

Blacksburg, VA

Keywords: Acoustic Liners, Finite Element Model, Impedance, Melamine, Microperforated  
Plate (MPP)

# Broadband Acoustic Liner Optimization Study Using Novel Poro-Elastic Materials

Kelsey Mitchell

Christopher R. Fuller, Chairman

Vibrations and Acoustics Laboratories

(ABSTRACT)

With the continual challenges associated with reducing aircraft engine noise, there is need for acoustic liner configurations that target broadband performance. This thesis experimentally and analytically investigates passive noise control methods to improve broadband frequency attenuation through various acoustic liner designs. The inclusion of acoustic metamaterials within these liners is examined and optimized. The metamaterials studied consist of resonant and non-resonant materials which include porous foams, microperforated plates (MPP), and embedded aluminum masses. Through finite element analysis, the understanding of the physics behind acoustics as well as aeroacoustics inspire their design. Sensitivity studies on the overall liner shape, facesheet properties, poro-elastic material properties, MPP's, as well as size and placement of embedded masses assist in successfully achieving broadband attenuation. Within the finite element study, an optimization tool will provide additional assistance in quantifying critical system parameters within the designs by minimizing the sum of the transmitted sound intensity over the design frequency bandwidth and hence maximizing attenuation. Broadband frequency absorption and attenuation is successfully achieved within the frequency range of 400-2600 Hz through the design of a varying depth optimized acoustic liner as well as a metamaterial-inspired liner.

## Acknowledgements

I would like to thank my advisor, Dr. Chris Fuller, for his guidance through this project. Not only for his knowledge but for his belief in my ability to complete and excel in this field has been much appreciated. I would also like to give a special thanks to my committee members Doug Nark and Mike Jones for their academic support and willingness to always help.

This project was supported and funded by NASA Langley through the Graduate Research Assistantship Program at Virginia Tech. An additional thank you goes out to Gail Coe and Cathy Hill for providing me with any assistance I need.

Additional support was provided by the National Institute of Aerospace and the Structural Acoustics Branch at NASA Langley. Without the availability of the 3-D printer at the NASA along with materials provided in the lab, this project would not have been possible. I would also like to thank the branch head, Dr. Kevin Shepherd, and assistant branch head, Dr. Ran Cabell, for providing me a work space and any resources I needed.

An additional thank you to Dr. Noah Schiller for always willing to answer any question I could ever think to ask. Whether trying to figure out a COMSOL issue or just taking a break for small talk, thank you for taking the time to assist with me growing as an academic as well as a person.

I finally would like to thank my good friends Jacob Bean and Nick Pera for their encouragement and graceful humor. Your ability to make me laugh when I was frustrated or just to listen when I need to complain is truly appreciated. I will miss you all very much.

As well, I would not have gotten anywhere without the support from my family. I strive to make you all proud and hope to touch as many lives as you all have. I love you all to pieces.

# Table of Contents

1. INTRODUCTION .....	1
1.1 Problem Statement .....	1
1.2 Background on Noise Control.....	3
1.2.1 Acoustic Liners .....	3
1.2.2 Acoustic Metamaterials.....	4
1.3 Research Aims/Objectives .....	5
1.4 Radiation Theory and Literature Review .....	6
1.4.1 Sound Radiation and Duct Acoustics.....	6
1.4.2 Literature Review.....	7
1.5 Thesis Outline .....	13
2 FINITE ELEMENT SIMULATION .....	15
2.1 Introduction.....	15
2.1.1 Basic Theory of Finite Element Methodology .....	15
2.1.2 Baseline Components.....	17
2.2 Physics Modeling with No Flow.....	18
2.2.1 Pressure Acoustics .....	18
2.2.2 Poroelastic Waves.....	21
2.3 Physics Modeling with Flow.....	21
2.3.1 Compressible Potential Flow (CPF), Stationary Domain .....	21
2.3.2 Linearized Potential Flow (LPF), Frequency Domain .....	23
2.4 Liner Boundary Conditions.....	26
2.4.1 Surface Impedance .....	26
2.4.2 3-D CAD.....	27
2.5 Optimization Module .....	28
2.6 Mesh Properties .....	29
2.7 Design Equations .....	30
3 EXPERIMENTAL VALIDATION .....	32
3.1 Experimental Test Section Description.....	32
3.1.1 Grazing Flow Impedance Tube.....	32
3.1.2 Normal Incidence Tube (NIT) .....	35
3.2 Experimental Validation Models .....	38
3.3 Plane Wave Radiation with $M=0$ in GFIT .....	43
3.3.1 Sound Pressure Level Plots.....	43
3.3.2 Phase Plots .....	45

3.4 Plane Wave Radiation with melamine embedded and $M=0$ in GFIT .....	48
3.4.1 Sound Pressure Level Plot and Phase plot .....	48
3.5 Plane Wave Radiation with and without melamine and $M=0.3$ in GFIT .....	49
3.5.1 Surface Impedance SPL and Phase plots .....	50
3.5.2 Full 3D CAD SPL plots without Melamine .....	51
3.5.3 Full 3D CAD SPL and phase plots with melamine embedded .....	53
3.6 Plane Wave Radiation in NIT .....	54
3.6.1 Surface Impedance Sound Pressure Level and phase plots .....	54
3.6.2 3D CAD Sound Pressure Level and phase plot .....	55
4 PRELIMINARY STUDIES OF SYSTEM COMPONENTS .....	60
4.1. Shape and Optimization Study .....	60
4.1.1. Constant Depth Extrusion .....	60
4.1.2 Single Section Angled Study .....	62
4.1.3 Four Section Angled Study .....	64
4.1.4 Sine Profile Study .....	65
4.1.5 Quadratic Profile Study .....	66
4.1.6 Conclusions of Shape Study .....	69
4.2 Porous Material Implementation .....	70
4.2.1 Melamine Foam .....	70
4.2.2 Polyimide Foam .....	71
4.2.3 Sensitivity and Optimization Study on Porous Material Properties .....	72
4.3 Microperforated Plate (MPP) .....	85
4.4 Acoustic Metamaterial .....	85
4.4.1 Embedded Masses .....	85
4.5 Microperforated Acoustic Metamaterials .....	94
4.5.1 Facesheet Studies .....	97
4.5.2 Microperforated Panel (MPP) Studies .....	98
4.5.3 Additional Foam Designs .....	102
5 ADDITIONAL OPTIMIZATION STUDIES USING A SUMMED INTENSITY OBJECTIVE FUNCTION .....	107
5.1 Power output .....	107
5.1.1 Optimized MPP location .....	107
5.1.2 Optimized Sphere location .....	109
5.1.3 Optimized MPP and Sphere Location Design .....	111
5.1.4 Optimized Sinusoidal Shape .....	113

5.1.5 Optimized Flow Resistivity Value .....	115
6 AEROACOUSTIC STUDIES .....	118
6.1 Flow Design Studies .....	118
6.2 Optimum Flow Design Comparison .....	122
7 CONCLUSIONS.....	125
8 FUTURE WORK.....	128
APPENDIX.....	129
REFERENCES .....	129

# List of Tables

Table 1. Mesh Properties for acoustic problem .....	30
Table 2. Constant depth liner geometrical parameters.....	39
Table 3. Variable depth liner geometrical parameters .....	40
Table 4. Partial variable depth liner geometrical parameters.....	41
Table 5. Parameters of the optimized NIT sample.....	43
Table 6. Objective table displayer iteration through COMSOL for model 1 and 2 .....	63
Table 7. Design chart and corresponding amount of TL over a certain frequency range .....	69
Table 8. Porous Material and embedded mass properties.....	70
Table 9. Optimized flow resistivity values to give maximum TL .....	73
Table 10. Optimized porosity values for maximum TL.....	75
Table 11. Optimized tortuosity values and corresponding TL.....	78
Table 12. Optimized permeability values and corresponding TL.....	80
Table 13. Optimized study showing the density value and corresponding TL .....	82
Table 14. Facesheet parameters for study .....	98
Table 15. Geometrical parameters for MPP.....	99
Table 16. Optimized location for MPP and corresponding TL.....	102
Table 17. Optimization solver for optimum MPP location and corresponding intensity level.....	108
Table 18. Optimization solver for sphere location and corresponding intensity level.....	110
Table 19. Optimization solver for sphere location with constant MPP and corresponding intensity level .....	112
Table 20. Optimization solver for optimum design point and corresponding intensity level.....	114
Table 21. Optimization solver for optimum flow resistivity and corresponding intensity level.....	116



# List of Figures

Figure 1. Turbojet engine showing acoustic liner placement [3].....	2
Figure 2. Conventional liner showing perforate over honeycomb core.....	4
Figure 3. Spring mass damper analogy for Helmholtz resonators.....	9
Figure 4. Physical simulation process flow chart.....	16
Figure 5. Duct in COMSOL displaying grazing flow duct geometrical constants.....	17
Figure 6. Normal Incidence Tube setup in COMSOL showing geometric constants.....	18
Figure 7. Incident and exit boundary conditions in COMSOL model.....	20
Figure 8. Boundary conditions used for COMSOL models incorporating flow.....	26
Figure 9. Location of surface impedance boundary on duct for COMSOL model.....	27
Figure 10. Boundary conditions in COMSOL demonstrating liner surfaces.....	28
Figure 11. COMSOL boundaries showing where pressure surfaces are taken for TL and $\alpha$ .....	31
Figure 12. Grazing Flow Impedance Tube (GFIT): (left) Main floor of GFIT with flow from left to right; (right) microphone instrumentation.....	33
Figure 13. Artist’s depiction of Grazing Flow Impedance Tube.....	34
Figure 14. GFIT GUI displaying the control of the test section in conjunction with LabView code.....	34
Figure 15. Normal Incidence Tube with supporting instrumentation.....	37
Figure 16. Section of facesheet showing geometric parameters.....	38
Figure 17. Photograph of constant depth liner with aluminum backing plate along with schematic diagram .....	39
Figure 18. Variable depth liner with backing plate along with schematic diagram of dimensions.....	40
Figure 19. Partial variable depth liner with backing plate with schematic diagram of dimensions.....	41
Figure 20. Constant depth liner in test section with melamine embedded in test section (left) back by aluminum plate (right).....	42
Figure 21. 3D printed 2x2 inch optimized NIT sample (left) with printed facesheet (right).....	42
Figure 22. Sound pressure level down the duct for frequencies 600, 1200, and 1800 Hz for the constant depth liner.....	44
Figure 23. Sound pressure level down the duct for frequencies 600, 1200, and 1800 Hz for the variable depth liner.....	44
Figure 24. Sound pressure level down the duct for frequencies 600, 1200, and 1800 Hz for the partial variable depth liner.....	45
Figure 25. Phase down the duct for frequencies 600, 1200, and 2000 Hz for the constant depth liner.....	46
Figure 26. Phase down the duct for frequencies 600, 1200, and 1800 Hz for the variable depth liner.....	47
Figure 27. Phase down the duct for frequencies 600, 1200, and 1800 Hz for the partial variable depth liner .....	47
Figure 28. Sound pressure level for the constant depth liner with melamine embedded.....	48
Figure 29. Phase plot for constant depth liner with melamine embedded.....	49
Figure 30. Sound pressure level plot of the surface impedance model with M=0.3 flow.....	50
Figure 31. Phase plot for the surface impedance model with M=0.3 flow.....	51
Figure 32. Sound pressure level plot for 3D geometry without melamine with M=0.3 flow.....	52
Figure 33. Phase plot for 3D geometry without melamine with M=0.3 flow.....	52
Figure 34. Sound pressure level plot for 3D geometry with melamine and M=0.3 flow.....	53

Figure 35. Phase plot for 3D geometry with melamine and $M=0.3$ flow .....	53
Figure 36. Sound pressure level plot for surface impedance NIT model.....	54
Figure 37. Phase plot for surface impedance NIT model.....	55
Figure 38. Sound pressure level plot for full 3D CAD NIT model.....	56
Figure 39. Phase plot for full 3D CAD NIT model.....	57
Figure 40. Resistance (top) and reactance (bottom) comparing the experimental to COMSOL results.....	58
Figure 41. Sound pressure level 2D plot for NIT sample at 2500 Hz.....	59
Figure 42. Constant depth extrusion liner .....	61
Figure 43. Transmission loss plot of constant depth extrusion study .....	61
Figure 44. Single section angled designs with geometric parameters shown on right.....	62
Figure 45. Transmission loss comparing models 1 and 2 for single sectioned angle study.....	64
Figure 46. Four step design COMSOL model .....	64
Figure 47. Transmission loss for four section angled design.....	65
Figure 48. Sine model displaying optimization variable amplitude movement.....	65
Figure 49. Three sine wave models used in wavelength study .....	66
Figure 50. Transmission plot showing wavelength study .....	66
Figure 51. Model 1 geometry (left) and new curvature geometry (right) .....	67
Figure 52. Transmission loss of model 1 vs. new curvature model .....	67
Figure 53. Models in the curvature study .....	68
Figure 54. Transmission loss of quadratic optimization study .....	68
Figure 55. Melamine foam.....	71
Figure 56. Polyimide foam .....	71
Figure 57. Transmission loss of flow resistivity of melamine sweep .....	73
Figure 58. Sensitivity study to porosity for transmission loss (upper) and absorption coefficient (lower) 75	75
Figure 59. Sensitivity study to Young's modulus for transmission loss (upper) and absorption coefficient (lower).....	76
Figure 60. Sensitivity study to tortuosity for transmission loss (upper) and absorption coefficient (lower) .....	77
Figure 61. Sensitivity study to permeability for transmission loss (upper) and absorption coefficient (lower).....	79
Figure 62. Sensitivity study to density for transmission loss (upper) and absorption coefficient (lower)..	81
Figure 63. Sensitivity study to Biot-Willis coefficient for transmission loss (upper) and absorption coefficient (lower).....	83
Figure 64. Sensitivity study to Poisson's ratio for transmission loss (upper) and absorption coefficient (lower).....	85
Figure 65. Liner domain and schematic figures from three views. Spheres highlighted in purple (one per cell) .....	86
Figure 66. Transmission loss of 1 aluminum sphere embedded in melamine foam model .....	87
Figure 67. Absorption coefficient of 1 aluminum sphere embedded in melamine foam model .....	87
Figure 68. Liner domain and schematic figures from three views. Spheres highlighted in purple (two per cell) .....	88
Figure 69. Transmission loss for 2 aluminum spheres embedded in melamine foam model .....	88
Figure 70. Absorption coefficient for 2 aluminum spheres embedded in melamine foam model .....	89
Figure 71. Liner domain with spheres highlighted in purple (3 per cell).....	90
Figure 72. Transmission loss for 3 aluminum spheres embedded in melamine foam model .....	90

Figure 73. Absorption coefficient for 3 aluminum spheres embedded in melamine foam model .....	91
Figure 74. Liner domain with spheres highlighted in purple (4 per cell).....	92
Figure 75. Transmission loss for 4 aluminum spheres embedded in melamine foam model .....	92
Figure 76. Absorption coefficient of 4 aluminum spheres embedded in melamine foam model .....	93
Figure 77. Transmission loss of 1-4 aluminum spheres embedded in melamine foam .....	93
Figure 78. Absorption coefficient of 1-4 aluminum spheres embedded in melamine foam .....	94
Figure 79. Partial variable depth with 2 inches of melamine embedded .....	95
Figure 80. (a) Constant Depth liner embedded with melamine (b) Variable depth liner embedded with melamine and (c) Partial variable depth liner embedded with melamine .....	96
Figure 81. CD, VD, VD all embedded with melamine vs. polyimide .....	97
Figure 82. Transmission loss plot for constant depth plate thickness sweep (left) and porosity sweep (right) .....	98
Figure 83. Constant depth MPP study examining MPP placement without melamine .....	100
Figure 84. Constant depth MPP study examining MPP placement with melamine .....	100
Figure 85. 1 MPP embedded within liner (left) and two MPP's embedded within liner equally spaced (right) .....	101
Figure 86. Constant depth MPP study with single and multiple MPP layers with and without melamine .....	101
Figure 87. Model 1 (left) and Model 2 (right) with melamine highlighted in purple along with schematic diagram .....	103
Figure 88. Transmission loss (left) and absorption coefficient (right) comparing models 1 and 2 with 0.25" and 0.5" melamine .....	103
Figure 89. Optimized design with MPP highlighted in purple .....	105
Figure 90. Transmission loss and absorption coefficient of optimized design .....	105
Figure 91. Total pressure propagation down the duct for optimized design at 2000 Hz .....	106
Figure 92. Intensity level across all frequencies for optimized MPP placement study.....	108
Figure 93. Transmission Loss of optimized MPP design .....	109
Figure 94. Intensity across all frequencies for optimized sphere placement study.....	110
Figure 95. Transmission Loss of optimized sphere location.....	111
Figure 96. Intensity across all frequencies for optimized sphere placement study.....	112
Figure 97. Transmission loss plot showing the optimum sphere and MPP design.....	113
Figure 98. Intensity level across all frequencies for optimized point for sinusoidal design .....	114
Figure 99. Transmission Loss of optimized sinusoidal design .....	115
Figure 100. Intensity plot across all frequencies for optimized flow resistivity design.....	116
Figure 101. Transmission Loss of optimized flow resistivity result.....	117
Figure 102. Transmission plot of the constant depth liner (left) and the variable depth liner (right) for speeds of $M=0-0.3$ .....	118
Figure 103. Transmission loss plot of the partial variable depth liner for speeds $M=0-0.3$ .....	119
Figure 104. Transmission loss plot of constant depth liner with porosity sweep .....	120
Figure 105. Absorption coefficient of constant depth liner with porosity sweep .....	120
Figure 106. Transmission loss plot of constant depth liner with plate thickness sweep.....	121
Figure 107. Absorption coefficient plot for the constant depth liner with plate thickness sweep .....	121
Figure 108. Transmission loss plot for optimized design at $M=0$ and $M=0.3$ flow.....	122
Figure 109. Absorption coefficient plot for optimized design at $M=0$ and $M=0.3$ flow .....	123
Figure 110. Total pressure for $f=1200$ Hz with flow (above) and without flow (below) .....	123

Figure 111. COMSOL interface of optimization solver ..... 132

# 1. INTRODUCTION

## 1.1 Problem Statement

Aircraft engine noise pollution has been an ongoing issue for decades. With continuous commercial aircraft disturbances, innovative noise suppression treatments are in high demand. There is a need for more powerful engines, with overall lighter output engine noise. The most desirable trait to any noise defeating technology is its secure ability to withstand multiple conditions. The FAA recognizes that this issue is highly complex and therefore pursues a program of aircraft control in collaboration with the aviation community. In February 2013, the International Civil Aviation Organization's (ICAO) Committee of Aviation Environmental Protection (CAEP) set a new global reduction standard. A goal of their active program, The Continuous Lower Energy, Emissions, and Noise (CLEEN), is to develop tools to reduce noise levels by 32 dB cumulative [1].

From porous fuselage walls to zero-splice intake liners, there are already multiple strategies to help suppress overall aircraft noise [2]. In addition, there has been significant progress in reducing aircraft noise not just by using increased bypass-duct engines, but by implementing passive treatments on the interior of the engine nacelle walls. These treatments do not require additional mechanical reconstruction on the engine's basic structure and therefore can be explored widely and easily. This application of acoustics liners has been around for years, but there is a paramount need to develop novel, more effective liners.

A liner design that is operative for multiple flight conditions such as take-off, cruise, and landing requires a design approach that considers broadband sound absorption. Acoustic treatment in addition must be lightweight and cost-effective. An example of a turbofan jet engine with an

embedded acoustic liner is shown below in figure 1 for demonstration. The apparent physical space limitations represent a large design challenge given the wide range of targeted noise spectra.

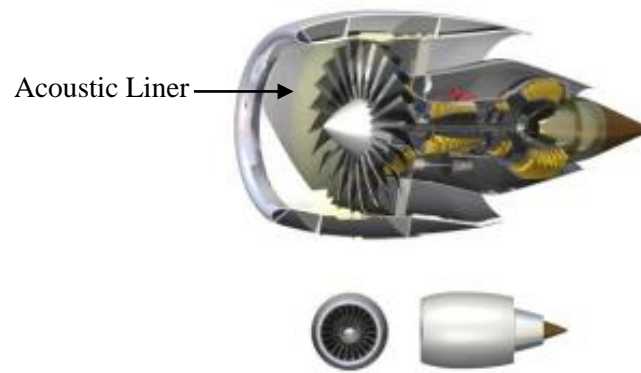


**Figure 1.** Turbojet engine showing acoustic liner placement [3]

Further improvement to conventional liners is desired by not only creating more efficient designs, but by incorporating passive noise control strategies that have been successfully used in similar noise applications.

The aim of this work is to validate, explore, and design new acoustic liner concepts for the application of engine noise treatment in the frequency range of 400-2600 Hz. The addition of flow up to speeds  $M=0.3$  will be analyzed as well. Acoustic metamaterials using microperforated plates, embedded masses, and porous foams will be explored in achieving this goal. While it has not yet been effective to include such porous materials inside an engine due to the harsh aeroacoustic thermal environment, it is beneficial to demonstrate the behavior of alternative suppression techniques such as metamaterials. By exploring material properties, future work can be completed to examine materials that have similar attenuating effects that enables the usage of alternative material. This method requires the investigation of both grazing flow experiments as well as normal incidence testing. In order to ensure an optimized liner, propagation prediction tools are

required and therefore explored through finite element analysis as well. These research efforts strive to improve the performance of acoustic liners for broadband absorption.

## 1.2 Background on Noise Control

Engine noise is composed of multiple contributions from the various internal mechanisms. Since the total energy in the form of sound does not change, it must be redirected to alternative forms. The two methods used for reducing undesirable sound consist of passive and active noise control. Passive noise control (PNC) technique converts this acoustic energy into heat through friction. This does not require additional control energy and is therefore relatively cheap to employ. This technique is apparent in the behavior of insulation, sound absorption and damping, and silencers [4]. A current example of passive noise control is seen by the use of poro-elastic foams that cause a loss of momentum through the pores [5]. In addition, acoustic liners dissipate sound energy through resisting and reacting porous facesheets and changes in acoustic impedance. Active noise control (ANC) methods create an exactly  $180^\circ$  out of phase signal to destructively interfere with a noise source. Typically this technique is more appropriate for lower frequencies [4]. Additionally, Helmholtz resonators can be used when the focus is on attenuating a narrow frequency bandwidth.

### 1.2.1 Acoustic Liners

Typical conventional liners consist of a perforated sheet covering a layer of honeycomb or square cells with a solid backing plate. There are single degree of freedom liners (SDOF) as well as double degree of freedom liners (DDOF) [6]. Each cell arrangement behaves as its own resonator, which is the basic mechanism in reducing propagating sound [7]. The liner's effectiveness is greatly dependent upon the ability to predict its acoustic impedance prior to its construction. In general, the more complex the geometry is, the more difficult it is to predict its

impedance. A typical image of a SDOF liner is shown below in figure 2 including the porous facesheet and honeycomb core.

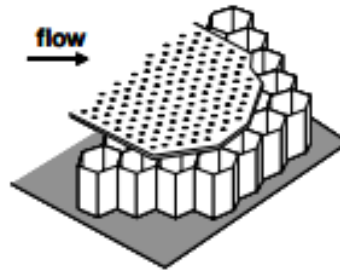


**Figure 2.** Conventional liner showing perforate over honeycomb core

While its ability to attenuate sound is useful for some landing conditions, its ability to completely absorb sound always has room for improvement. In order to achieve broadband absorption, a certain cell depth is necessary for low frequency absorption that might not be physically possible to design due to lack of design space. For high frequency absorption, it is generally difficult to attenuate sound due to the addition of multiple modes in the pressure field. Certain parameters such as cell depth, liner length, facesheet parameters, as well as overall geometric dimensions of the extruded core can be manipulated to dramatically affect the behavior and therefore be designed and optimized.

### 1.2.2 Acoustic Metamaterials

Acoustic metamaterials are man-made materials that possess properties that cannot be found in nature [8]. There has been an explosion of interest in this field due to its ease of manipulability and widespread applications [9]. The two types of acoustic metamaterials include resonant and non-resonant materials. Non-resonant materials consist of a periodic arrangement of embedded elements that are usually spaced less than a wavelength apart. This method creates energy loss by the scattering and disruption of waves through the material. Resonant metamaterials



as well contain a periodic arrangement of elements smaller than the acoustic wavelength of the material they are embedded in [8]. However, by changing the arrangement, spacing, and density of their interior elements, the material can be dynamically tuned and behavior of the wave propagation to be altered. These materials are generally called heterogeneous (HG) metamaterials and will be briefly explored in this research.

### 1.3 Research Aims/Objectives

The primary objective of this research is to analyze and design conventional, broadband acoustic liners as well as liners that include a passive acoustic metamaterial-inspired design to reduce noise produced by engines. The secondary aims are as follows:

- Understand current liner behavior by analyzing already-accumulated data
- Develop a finite element model of a small-scale impedance duct that predicts pressure acoustics as well as aeroacoustics
- Validate the finite element model by comparing to tested data with grazing and incident plane wave radiation with and without flow using sound pressure level and phase plots
- Perform simulations for multiple liner designs that target broadband frequency range performance between the frequency range of 400-2600 Hz using two performance metrics including transmission loss and absorption coefficient
- Develop new metamaterial design embedded within acoustic liner
- Perform sensitivity studies on components of metamaterial-inspired design
- Use an optimization tool in the finite element modeling to then design and build best-performing design
- Provide recommendations for future work

## 1.4 Radiation Theory and Literature Review

An overview of previous work relating to research conducted on acoustic liners and metamaterial as a means of improving their performance will be presented beginning with a discussion of sound radiation and duct acoustics. A short history of the progression of this technology is then explored as well as the fundamentals of their behavior. The major components including acoustic metamaterials, poro-elastic materials, conventional liners, standing wave tube measurements, as well as finite element modeling on previous work will be discussed as well.

### 1.4.1 Sound Radiation and Duct Acoustics

Throughout this research, a rectangular duct of constant cross-section will be the consistent test domain. The reduced acoustic wave or Helmholtz equation may be solved for by means of a series expansion called modes [10]. The general modal solution of sound propagation in a rectangular hard-walled duct can be found as follows.

Separation of variables in the equation

$$p(x, y, z) = F(x)G(y)H(z) \quad \text{Eq. (1)}$$

applied to the equation

$$\nabla^2 p + \omega^2 p = 0 \quad \text{Eq. (2)}$$

in the duct for which  $0 \leq x \leq a$  and  $0 \leq y \leq b$ , results into the equations

$$F_{xx} = -\alpha^2 F, G_{yy} = -\beta^2 G, \text{ and } H_{zz} = -(\omega^2 - \alpha^2 - \beta^2)H \quad \text{Eq. (3)}$$

where  $\alpha$  and  $\beta$  are eigenvalues to be solved for from the hard-wall boundary conditions. After further solving, the general solution for the pressure down a hard-wall duct is computed as

$$p(x, y, z) = \sum_{n=0}^{\infty} \sum_{m=0}^{\infty} \cos(\alpha_n x) \cos(\beta_n y) (A_{nm} e^{-ik_{nm}z} + B_{nm} e^{ik_{nm}z}) \quad \text{Eq. (4)}$$

where  $A$  and  $B$  are modal amplitudes and  $\alpha_n$ ,  $\beta_n$ , and  $k_{nm}$  are solutions to the equations  $F(x)G(y)H(z)$ . They are given as

$$\alpha_n = \frac{n\pi}{a}, \beta_n = \frac{m\pi}{b}, \text{ and } k_{nm} = (\omega^2 - \alpha_n^2 - \beta_m^2)^{1/2} \quad \text{Eq. (5)}$$

When the duct is lined with sound absorbing material such as an acoustic liner, the material is denoted as being locally reacting and is given a certain impedance  $Z(\omega)$  as a function of frequency (scaled on  $\rho_0 c_0$ ). Usually lining is applied in an attempt to reduce the sound level by dissipation and transform energy into alternate forms. The simplest approach would be to look at which impedance gives the greatest reduction. This, however, varies with the source of the sound, frequency contribution, geometry, etc. In order to obtain the most reduction, the time-averaged intensity at the wall directed into the wall must be minimized. This equation is simplified as:

$$\langle I \cdot e_r \rangle \propto \text{Im}(\alpha_{m\mu}^2) \quad \text{Eq. (6)}$$

where  $I$  is intensity [ $\text{W}/\text{m}^2$ ] and  $\alpha_{m\mu}$  is a solution to the imaginary impedance. The intensity is also calculated as

$$I = \frac{\int P dA}{v} \quad \text{Eq. (7)}$$

where  $P$  is the sound pressure and  $v$  is the particle velocity. With the two metrics being dependent only on the pressure, this value at the exit of the duct will be minimized to give maximum attenuation.

#### 1.4.2 Literature Review

Intuitively speaking, the most efficient location to target aircraft noise control is in the engine. While engines have been effectively quieter each year, design alone does not enable it to operate at acceptable noise levels. As early as the mid-1970's, engineers began publishing work that focused on the design and optimization of acoustic liners [11]. Boeing and NASA-Langley

initiated a research program for the study of turbofan nacelle modifications to minimize engine noise on 707-type airplanes. By analyzing effects of acoustic and geometric parameters of liners, the program was able to come to conclusions regarding the resulting attenuation. They had stated that the attenuation “depended on a number of parameters, the most important being: the length of treatment, duct size, lining cavity depth, cavity-cell size, and the resistive and reactive impedance” [12]. Throughout the years, more research was completed regarding these parameters relationship to each other. A study was done on the effects of the liner geometry on acoustic impedance in 2002 at NASA Langley Research Center. Conclusions were made such as a decrease in porosity of the facesheet increases the resistance and reactive component of the impedance [12]. In addition, the cavity depth increase creates a shift to lower resonance frequencies [12].

In 2002 NASA Ames developed deep acoustic lining for the 40 by 80 ft. wind tunnel test section [13]. The resulting acoustic lining was nominally 42 inches deep encircling the 83 ft. long test section. The primary design goal was to operate from 80 Hz to 20 kHz with a minimum of 90% energy absorption. This was a significant step in large-scale modeling and the advancement of exploring unusual designs over such a broad frequency range. The finality of this project gave confidence that the preferred design would meet the acoustic, aerodynamic, and structural objectives desired. The large test section, near-anechoic environment, and subsonic speed capabilities were then able to support testing from takeoff to landing configurations of transports [13].

The basic mechanism that allows acoustic liners to attenuate sound mimics the behavior of a Helmholtz Resonator (HR) [3]. The two main components are the cavity volume and the opening to the neck. One analogy that an HR is commonly compared to is a spring-mass damper system. The air in the neck is treated as a single unit and hence mass of the system. The air in the remaining

volume can be viewed as a spring where other parameters make up the dampening. An image of this analogy is shown below in figure 3.

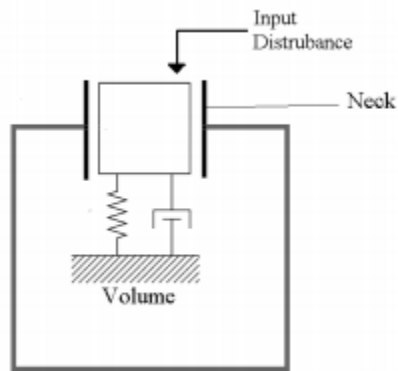


**Figure 3.** Spring mass damper analogy for Helmholtz resonators

The inclusion of porous materials within a noise suppressing device has received much attention recently. Wave propagation through an inhomogeneous poroelastic material and the solution of the full wave equation is examined by Gautier [14]. This study focused on the solution in which the acoustic and elastic properties of the material vary in 1D. By obtaining the reflection coefficient on a porous material, the scattered field can then be calculated. Results obtained by this method are compared to the classical transfer matrix and discussion about the absorption coefficient for various porous is further explained. The expansion into studies regarding porous material properties is a crucial step in better predicting attenuation behavior for full 3D scale.

An additional method of sound reduction is the implementation of absorptive materials that combine multiple noise control methods. Passive and active control methods have been seen in many applications such as in motors or fans. Low frequency noise has been an issue for these mechanical systems and a need for substantial absorber treatments was apparent. An advanced passive treatment was created in a study by Fuller and Harne [4] discussing a Heterogeneous (HG) material with embedded vibration absorbers. The HG blanket provided melamine foam layers, with tunable masses in a frequency range of about 60-250 Hz. Distributed Vibration Absorbers

(DVAs) [15] proved to act as a low frequency absorber giving losses on the order of 10 dB at frequencies below 200 Hz. Further, a study was performed in 2004 on these DVAs and was advanced to playing an active role in sound absorption. This control had been developed to monitor radiation in the lower frequencies up to 1000 Hz, where conventional passive techniques were inefficient [15]. One of the main conclusions from this research suggested that the stretching of the foam layer was the main mechanism of energy dissipation around the tuned frequency. The DAVA system not only outperformed the ACLDs but required less variables for the analytical model, which reduced the overall computational load.

Acoustic metamaterials have been incorporated in applications such as sensor detection, solar power management, classic optics, and material sciences. Recently, work was carried out in the investigation of HG metamaterials focusing on low frequency noise reduction in normal incidence impedance tubes [8]. Investigating passive and active control methods, successful tonal and broadband noise was achieved using a feedforward, filtered-x LMS control algorithm [8]. By combining microperforated panels, embedded masses, and porous materials, transmission loss was increased in critical low frequency ranges below 500 Hz.

Moreover, the concept of metamaterial extends beyond the control of noise radiation. For example, the invisible cloak is proposed to render the hidden object undetectable under the flow of light or sound by guiding the controlling the wave path through an engineering space that surrounds the object [16]. The cloak is constructed with serial inductors and shunt capacitors. It is able to bend the ultrasound waves around the hidden object and should be scalable to different acoustic frequencies.

The control of aircraft interior noise has been an issue as well as the control of exterior engine noise suppression. By using the HG blanket concept, Idrisi [17] explained the two passive

control mechanisms that potentially controls a very wide frequency range. Using damping and dynamic absorption, the HG blanket concept evolved from a single-point absorber, extended to multiple absorbers coupling together, and finally to a full broadened HG concept. A single-bay double panel system (DPS) is mathematically modeled and experimental measurements validate the predicted responses of this system. Idrisi concluded from this analysis that by tuning the masses inside the HG blanket, the vibration levels of both the fuselage and the trim panels were able to be reduced [17]. It was also shown that the HG blanket achieved low frequency control while maintaining high frequency performance (in frequencies above 500 Hz).

A foam-metal liner was developed and tested on a low speed fan in order to observe different placement effects on overall performance. Higher attenuation levels were achieved by placing the liner in closer proximity to the rotor rather than the nacelle [18]. The acoustic performance of the liner achieved up to 4 dB of broadband attenuation. If designed correctly, foam-metal liners can survive in the environment and can attenuate by providing a pressure release surface and emitted farfield noise [18].

In order to evaluate radiation behavior, standing wave tubes (SWTs) have been around for years. SWTs are used worldwide in acoustics for calibration and acoustic measurement purposes [19]. Nichols experimented with a SWT by using a sinusoidal signal to excite a piezoelectric transducer to create standing waves in a cylindrical tube. The main objective of this work was to validate the theory of a pressure wave in the standing wave tube to experimental data collected. A noteworthy feature of the results is that the dissipative effects present in the tube is highly dependent upon the atmospheric effects, especially humidity. The dissipative constant used in the theoretical calculations must be chosen so that the resonant widths appear to be the same in the data collected. The main inconsistency between the two type's procedures is the behavior of the

peak amplitude. In theory, the peak amplitude remains constant across the frequency spectrum, while the measurements showed an increasing amplitude right above 1500 Hz. It was concluded that the signal frequency approaches the first resonance of the piezoelectric driver, which manifests as the pressure amplitude increases.

To address the challenge and cost of recreating a test model using a test rig, analytical tools that predicted noise radiation were in high demand as well. In 1996 a numerical method extracting liner impedance data was tested and validated. The initial evaluation examined the method's capability to converge to known normal-incidence impedance values. Having this tool then sparked interest in examining the addition of flow and higher frequencies not before tested. An additional acoustic propagation code known as CDUCT-LaRC was built to study benchmark cases with plane wave sources [20]. This code is based on the CDUCT code developed by Dougherty and extended by Lan [21]. It will also be used for some impedance prediction behavior with the finite element tool.

Finite element modeling for acoustics is a commonly used numerical prediction technique that is based on two concepts: transformation of the original problem to a comparable integral formulation, and an approximation of the field variable distributions and the geometry of the continuum domain in terms of small subdomains or 'finite elements' [22]. The weighted residual concept provides an equivalent integral formulation of the Helmholtz equation that defines a steady-state acoustic pressure field in a bounded fluid domain. The fluid domain is then discretized into the finite elements there the field variable, i.e. the pressure, is approximated as an expansion in terms of a number of prescribed shape functions. The prediction accuracy depends on the number of elements, noting that the accuracy systematically improves as the number of elements increases [22].



An additional study of plane wave acoustic phenomena in ducts was performed by Betts [23] examining certain finite element factors such as shape functions, mesh refinement, as well as element distortion and their effects. It was concluded that the higher order shape function eight-node quadrilateral element resulted in considerably better results than did the four-node quadrilateral element. The average error was nearly 30% for a mesh refinement for about 14 elements per wavelength at 100 Hz frequency. The study also showed that the type of boundary condition used had a substantial effect on the accuracy of the final solution. Another early study was conducted looking at the mesh refinement to predict transmission loss and reflection coefficients. It was concluded that improved solutions were obtained by performing evaluations at gauss points rather than nodal points [23].

### 1.5 Thesis Outline

Chapter 1 provides the problem statement behind this work along with an introduction to multiple types of noise control. The theory of acoustic liners is introduced as well as the introduction of acoustic metamaterials and their past usage. It also provides the list of research aims and objectives.

Chapter 2 introduces the Multiphysics Finite Element tool known as COMSOL that is used to analytically validate and design the models. The basic boundary conditions are discussed as well as a brief explanation of the physics with and without flow. The design equations that are the primary measure of performance are introduced as well.

Chapter 3 provides a description of the initial experimental validation work. The Normal Incidence Tube (NIT) along with Grazing Flow Impedance Tube (GFIT) at NASA Langley will be the test facilities utilized during this project. The experimental validation work is compared to

the analytic results to enable the continuation of the design stage. In addition, the baseline acoustic liners that will constantly be referred to throughout the thesis are familiarized.

Chapter 4 explores the results of the preliminary studies of the project. Beginning with just a liner shape study, a buildup of the components eventually ending with an acoustic metamaterial design is explored. Optimization studies will be performed in this section as well.

Chapter 5 discusses additional optimization studies that minimize the sum of the transmitted sound intensity over the design frequency bandwidth at the exit plane of the duct. The models used in this chapter are identical to the models used in the alternative optimization approach.

Chapter 6 discusses the addition of flow into the design study and explores sensitivity studies on speeds up to  $M=0.3$ .

Chapter 7 summarizes the overall conclusions and presents the potential future work of this research.

## 2 FINITE ELEMENT SIMULATION

### 2.1 Introduction

Finite element analysis is a suitable technique to validate and explore physical liner designs due to its prediction capabilities and success in previous work. This method accurately reduces complex partial and ordinary differential equations to a set of easily solvable linear equations. In this research, all analytical investigations are performed using COMSOL Multiphysics version 5.0. By coupling different physics through dependent variables, COMSOL allows multiple physics simulations [24]. There are numerous physics modules contained in COMSOL such as mechanical, chemical, fluid and electrical. With its widespread modeling capabilities specifically in the acoustics domain, COMSOL is able to capture and measure acoustic wave propagation with and without flow.

There are multiple physics in COMSOL utilized throughout this research. These include Pressure Acoustics, Poroelastic Waves, Linearized Potential Flow, and Compressible Potential Flow. The physics are coupled through their own dependent variable(s), allowing a full demonstration of the propagation of acoustic waves through fluid domains. In addition, an optimization module is employed at the end to further optimum designs. Proper boundary condition treatment plays an essential role in the accuracy of the model. Once each boundary condition within the model is defined, the elliptical tool is allowed to behave as accordingly to solve the problem at hand.

#### 2.1.1 Basic Theory of Finite Element Methodology

Finite element analysis was developed in 1943 by R. Courant, who initially utilized the Ritz method of numerical analysis. The basic concept in the physical interpretation of finite

element modeling is the subdivision of the model into non-overlapping component of simplified geometry called elements [25]. The elements are then connected at nodes to form an approximate system of equations modeling the whole structure. The system of equations is then solved for at the nodes for certain quantities, such as displacement. An energy functional is minimized in order to obtain these quantities. This energy functional consists of all of the energies associated within the particular model at hand. In order to minimize the energy functional, the derivative of the functional with respect to the unknown grid point potential is set to zero. Hence, the basic equation for finite element investigation is set to be

$$\frac{\partial F}{\partial P} = 0 \quad \text{Eq. (8)}$$

where  $F$  is the energy functional and  $p$  is the unknown point grid potential. Each finite element will have its own energy functional. This idea is based on the principle of virtual work, where the virtual work is zero when a particle is in equilibrium and set under a number of forces. A simplified view of the physical simulation process is shown in the figure below to demonstrate modeling terminology.

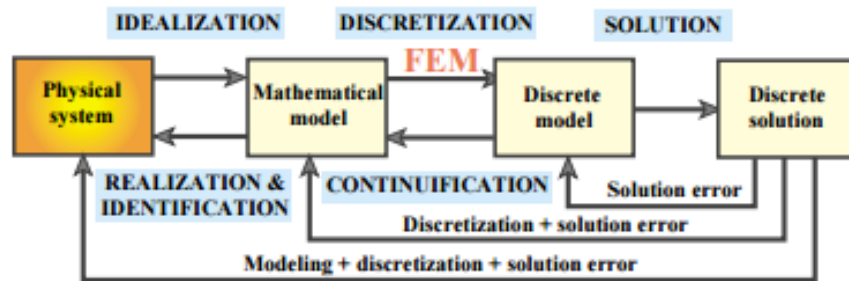


**Figure 4.** Physical simulation process flow chart

Idealization will pass the physical system to the mathematical model. The number of degrees of freedom are then reduced to a finite number in order to make the numerical simulation practical. Analytical solutions are then solved for as a closed-form solution. Finally, the last key strength of

the modeling is the ability for the program to handle interface conditions. Setting the proper boundary conditions between essential and natural is a crucial step in this systematic procedure.

### 2.1.2 Baseline Components

Geometrically speaking, throughout the study the main COMSOL test domain consists of a 40 inch length duct, with a width of 2 inches and height of 2.5 inches. This was chosen to match the shape of the Grazing Flow Impedance Tube at NASA Langley, which is supporting the experimental testing. The liner is consistently placed at a location of 8 inches aft the incident plane. The liner's length varies from 15.3 inches up to 16.8 inches, while varying its depth to a maximum amount of 3 inches, in order to keep within typical mechanical design constraints. The image below shows a simple constant depth liner as to demonstrate the basic geometrical properties of the COMSOL setup to simulate grazing flow.

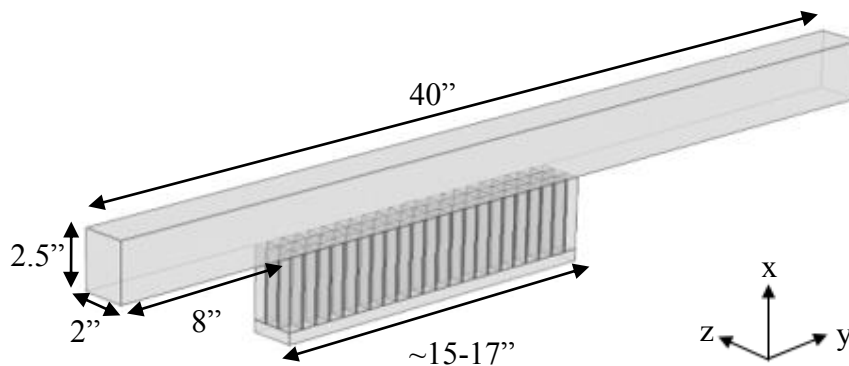


**Figure 5.** Duct in COMSOL displaying grazing flow duct geometrical constants

The additional setup in COMSOL is built to match the dimensions of the Normal Incidence Tube (NIT). As this model is only used for validation purposes, the source and exit planes are defined prior to running the code using the experimental results as input values. The complex pressure was set at  $x=6$  inches to bound this problem. The liner is placed below the duct to simulate normal incidence. The image below demonstrates this model.

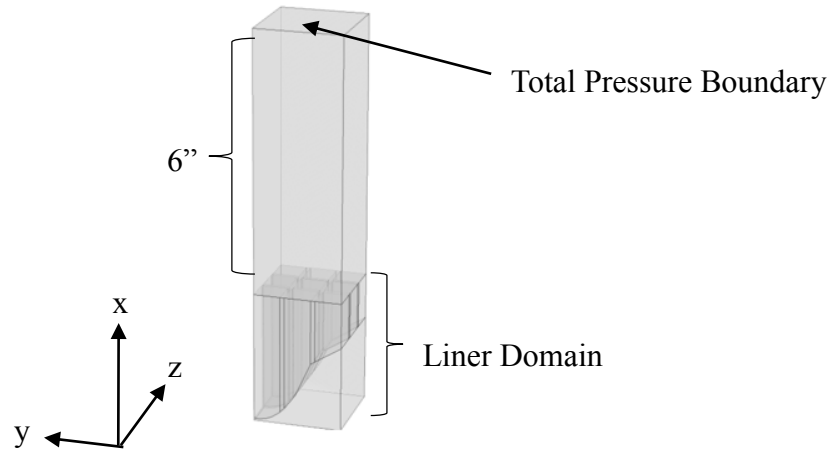


**Figure 6.** Normal Incidence Tube setup in COMSOL showing geometric constants

Before diving into the design stage, the properties of the finite element tool is further explained below.

## 2.2 Physics Modeling with No Flow

### 2.2.1 Pressure Acoustics

When modeling plane sound wave radiation with no flow, the single physics needed is Pressure Acoustics. For this approach, the linearized Euler equations reduce to the scalar convected Helmholtz equation to solve for the pressure as shown below:

$$\nabla \cdot \left( -\frac{1}{\rho c} (\nabla p - q) \right) - \frac{\omega^2}{\rho_0 c^2} p = Q \quad \text{Eq. (9)}$$

where  $p$  is the total pressure,  $\rho$  is the density of the fluid,  $Q$  is the possible monopole source,  $\omega$  is the angular frequency or  $2\pi f$ ,  $c$  is the speed of sound, and  $q$  is the possible dipole source. The speed of sound as the wave travels through air is 343 m/s. The frequencies studied **range from 400:10:2600 Hz**, as to satisfy the broadband aim of this research. In the homogenous case where the two source terms  $q$  and  $Q$  are zero in equation 9, one simple solution is the plane wave pressure defined as:

$$p = P_0 e^{i(\omega t - ky)} \quad \text{Eq. (10)}$$

where  $y$  is the position traveling down the length of the duct, and  $t$  is the time; where in this case is zero since only a time-independent, frequency domain is evaluated. Frequency analysis can be used for quantification of a noise problem, as the proposed controls are frequency domain, such as the sound pressure level and phase [26].

### Boundary Conditions for Pressure Acoustics

Within the pressure acoustics physics, there are multiple ways to define plane wave propagation. Beginning at the validation stages, the proper way to analytically bound the model to match the experimental results is performed in the following technique. The complex pressure is defined on the incident and exit boundaries of the duct to exactly match the experimental results. Using a pressure boundary condition, the total complex pressure is defined by an amplitude and corresponding phase. For example, at the incident plane or  $x=0$ , the amplitude of the wave in Pascal's from the experiment is defined as  $P(\omega)$ . The corresponding phase in radians is defined as  $\phi(\omega)$ . Using these two values, the total complex pressure value at the source plane is given as:

$$P_T(\omega) = P(\omega)e^{i\phi(\omega)} \quad \text{Eq. (11)}$$

The same procedure is repeated for the exit plane of the duct. Once the problem is fully bounded, the elliptical tool will then solve the acoustic wave equation. As this procedure demanded prior experimental results, this was only used for the validation stages. Once this was completed, the next method is utilized in order to begin the design process.

The basic and default way to initiate a plane wave is to set a plane wave radiation boundary. This allows for the input of the incident pressure magnitude, which will be 1 Pa for every design case. An additional incident pressure field node is added as well in order to define the field type.

At the exit of the duct, a perfectly matched layer (PML) is defined as a volume. This exit condition acts as an anechoic termination as to simulate no reflections. This crucial setup helps

keep consistency when comparing and examining final liner performances against each other. An image of a COMSOL model displaying the boundaries previously explained is shown below:

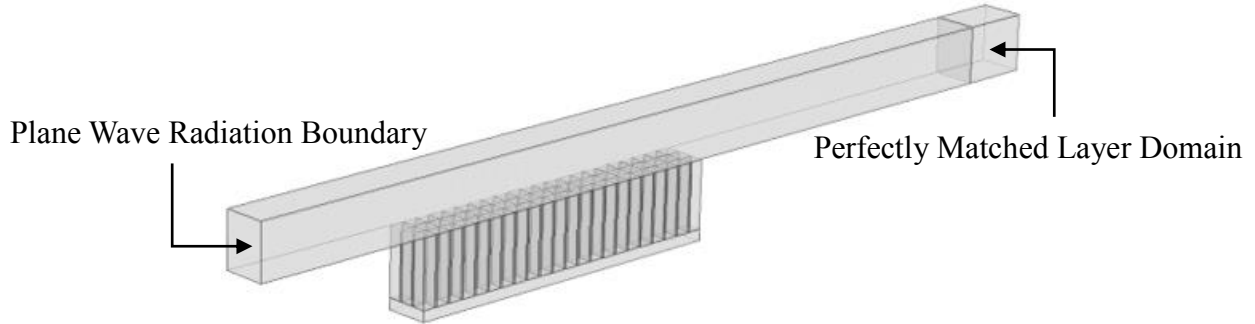


**Figure 7.** Incident and exit boundary conditions in COMSOL model

### Poroacoustics Modeling

When adding a porous material into the liner design; such as melamine or polyimide, an additional physics domain as part of pressure acoustics must be added. Known as poroacoustics, this system defines a fluid domain modeled in a homogenized way or equivalent fluid model.

The default model for this physics is known as the Delany-Bazley Miki model [24]. This model is based on the assumption that the porosity is nearly one. The porous material properties must be added initially in order to coalesce appropriately with the wave propagation through it. The only required parameter is the flow resistivity  $R_f$  (SI unit: Pa·s/m<sup>2</sup>) from the material. The surface impedance of foam predicted by the Delany- Bazley model takes into account the flow resistivity  $\sigma$  of the foam [27]. Equation 11 below solves for the impedance given as:

$$Z = R + jX = \rho_0 c \left[ 1 + 0.0571 \left( \frac{\rho_0 f}{\sigma} \right)^{-0.754} - j(0.087) \left( \frac{\rho_0 f}{\sigma} \right)^{-0.732} \right] \quad \text{Eq. (12)}$$

An additional requirement is for the flow resistivity to be within the range of 10-50 kPa·s/m<sup>2</sup>.



### 2.2.2 Poroelastic Waves

An additional way to model plane wave radiation with the incorporation of a porous material is by implementing the poroelastic waves physics. This physics differs from pressure acoustics in that it takes into account the shear waves rather than just the pressure waves. The Biot model includes an isotropic skeleton along with four parameters that include the elastic effects of the porous frame. As the foam is isotropic, the material will be independent of direction. The benefit in modeling any porous foam in this manner is the capability to input and adjust additional foam parameters such as the porosity, density, tortuosity, Young's modulus, Poisson's ratio, permeability, and the Biot-Willis coefficient. These parameters will come into play during sensitivity studies within the design stages.

#### Boundary Conditions for Poroelastic Waves

With the inclusion of a second physics to model plane wave radiation, additional boundaries must be set. The foam itself must be selected as a porous material. As well, if there are embedded aluminum or steel masses, these must be defined as a linear elastic material. The tool then has the ability to couple the physics with each other through a multiphysics node, as well as defining the type of dual interaction – hence an acoustic-porous boundary interaction.

### 2.3 Physics Modeling with Flow

With the addition of flow, two supplementary physics must be defined including compressible potential flow and linearized potential flow.

#### 2.3.1 Compressible Potential Flow (CPF), Stationary Domain

Assuming an ideal, barotropic, irrotational and inviscid fluid, this physics enables the user to define a velocity potential in a compressible potential flow field. The two dependent variables

include the mean flow velocity potential and the density. The general equation demonstrating this physics is shown below:

$$\nabla \cdot (\rho \nabla \phi) = 0 \quad \text{Eq. (13)}$$

where  $\rho$  is the density and  $\phi$  is the velocity potential. This study is done in the stationary domain as the field variables will not change over time. The solution of this equation for pressure as related to the velocity potential is given as

$$p(r, t) = -\rho \left( \frac{\partial \phi}{\partial t} + V \cdot \nabla \phi \right) \quad \text{Eq. (14)}$$

where the velocity potential is solved for as

$$\phi(r, t) = \phi(y, z) e^{i(\omega t - k_x x)} \quad \text{Eq. (15)}$$

Looking at this equation, the partial of  $\phi$  with respect to time must be solved for. This is given by the equation below as

$$\frac{\partial \phi}{\partial t} = i\omega \phi(r, t) \quad \text{Eq. (16)}$$

Finally, plugging the equation back in simplifies the pressure to

$$p(r, t) = -\rho(j\omega \phi(r, t) + V \cdot \nabla \phi) \quad \text{Eq. (17)}$$

When testing with flow, it is noted that since the velocity is not equal to zero, the pressure will depend on the gradient of the velocity potential [28]. Therefore, for the validation stages there will be necessary information needed a priori. If, however, there is a desired acoustic pressure at each surface, one can add a global equation that can update the applied velocity potential such that it will equal the anticipated pressure. Hence, the equations below demonstrates this scenario:

$$\phi_{source} = P_{ave,source} - P_{source} \quad \text{Eq. (18)}$$

$$\phi_{exit} = P_{ave,exit} - P_{exit} \quad \text{Eq. (19)}$$

Where the average pressure surfaces at the source and exit are iterated until they equal the inputted source and exit pressure calculated from the input potential velocity equation above.

### Boundary Conditions for CPF

Two nodes must be added to this physics including a mass flow and a normal flow. The normal flow node, set at the exit plane, implies that the tangential velocity is zero; corresponding to a constant velocity potential on the boundary. The mass flow node is set at the incident plane and gives a normal velocity  $V_n$  and fluid density at the boundary as  $\rho_{bnd}$ . The mass flow itself is defined by the product of these two values.

### 2.3.2 Linearized Potential Flow (LPF), Frequency Domain

This frequency domain interface is used to compute the acoustic variations in the velocity potential in the presence of a potential flow [29]. As termed potential, this physics has limitations up to  $M < 1$ . The dependent variable in this physics is the velocity potential which allows the coupling between CPF. The equation defined in the physics is shown below:

$$-\frac{\rho_0}{c_0^2} i\omega(i\omega\phi + \mathbf{V} \cdot \nabla\phi) + \nabla \cdot \left( \rho_0 \nabla\phi - \frac{\rho_0}{c_0^2} (i\omega\phi + \mathbf{V} \cdot \nabla\phi) \mathbf{V} \right) = 0 \quad \text{Eq. (20)}$$

Each term in this equation has been previously defined as the density, frequency, speed of sound, potential velocity, and velocity.

### Boundary Conditions for LPF for Validation

During the validation stages, prior data was collected and then inputted into COMSOL in the same manner as with no flow. Hence, the SPL (dB) and phase (rad) values on the wall opposite the liner were measured per frequency. To be specific, the following calculations were taken to convert these values into the corresponding velocity potential.

$$P_{source\ Pa} = 10^{(SPL_{dB}/20)} (20e^{-6})\sqrt{2} \quad \text{Eq. (21)}$$

$$P_{source} = P_{source\ Pa} * e^{i(phase)} \quad \text{Eq. (22)}$$

and finally, the velocity potential input became

$$\phi_{source} = P_{ave,source} - P_{source} \quad \text{Eq. (23)}$$

The same procedure is repeated for the exit plane.

### Facesheet Modeling

The facesheet can be defined by an interior impedance model as well. The value of the impedance however is determined by the standard two-parameter iterating model approximation [30]. This takes into account the changing RMS acoustic velocity, which varies per frequency and Mach number. The input equation for the impedance of the facesheet is:

$$Z_{facesheet} = \rho_{air} c_{air} [\theta_{linear} + \theta_{nonlinear} + \theta_{gf} + i(\chi_{fs})] \quad \text{Eq. (24)}$$

where

$$\theta_{linear} = \frac{a\mu t_p}{2\rho_{air} c_{air} \sigma C_D d_{hole}^2} \quad \text{Eq. (25)}$$

where  $\mu$  is the dynamic viscosity of air,  $t_p$  is the plate thickness,  $\sigma$  is the porosity,  $C_D$  is the discharge coefficient 0.771 by default,  $a$  is the implicit empirical constant of 64 by default, and  $d_{hole}$  is the hole diameter. The second unknown term is defined as

$$\theta_{nonlinear} = \frac{v_{rms}[\kappa_i + \kappa_e]}{2c_{air}(\sigma C_D)^2} \quad \text{Eq. (26)}$$

where  $v_{rms}$  is the iterated acoustic velocity, and  $\kappa_i$  and  $\kappa_e$  are the empirical constants for hole entrance exit effects (which are by default both 0.5). The third term is the grazing flow effect given by

$$\theta_{gf} = \frac{\frac{V_y}{c_{air}}}{\sigma(2 + \frac{1.256\Delta_{BL}}{d_{hole}})} \quad \text{Eq. (27)}$$

where  $V_y$  is the velocity vector in the direction of flow, and  $\Delta_{BL}$  is the boundary layer displacement constant being 1.75e-3(m). The last term in the impedance equation is the normalized mass reactance due to the perforate facesheet and is calculated as

$$\chi_{fs} = \frac{\omega}{c_{air}} \left( \frac{t_p + \varepsilon d_{hole}}{\sigma C_D} \right) \quad \text{Eq. (28)}$$

where  $\varepsilon d$  is the hole length end correction and

$$\varepsilon = 0.85 \left( \frac{1 - 0.7\sqrt{\sigma}}{1 + 305 \left( \frac{V_y}{c_{air}} \right)^3} \right) \quad \text{Eq. (29)}$$

These impedance values are then inputted into the interior perforated plate boundary node.

#### Boundary Conditions for LPF for Design

Once the validation stages are complete, the model setup is slightly altered. A velocity potential node must be set at the source plane as to generate a total velocity potential input. The units of this value should be m<sup>2</sup>/s. The equation used to determine these values are shown below, as taken from experimental data.

$$\tilde{\varphi} = \frac{\tilde{P}(M+1)}{-i\rho_0\omega} \quad \text{Eq. (30)}$$

where M is the Mach number, and  $\tilde{P}$  is the pressure amplitude.

The core of the liner must be interior sound hard as it was previously set in pressure acoustics. The final node that must be added is an additional linearized potential flow model to define the PML volume. The figure below shows the location of each boundary condition described above.

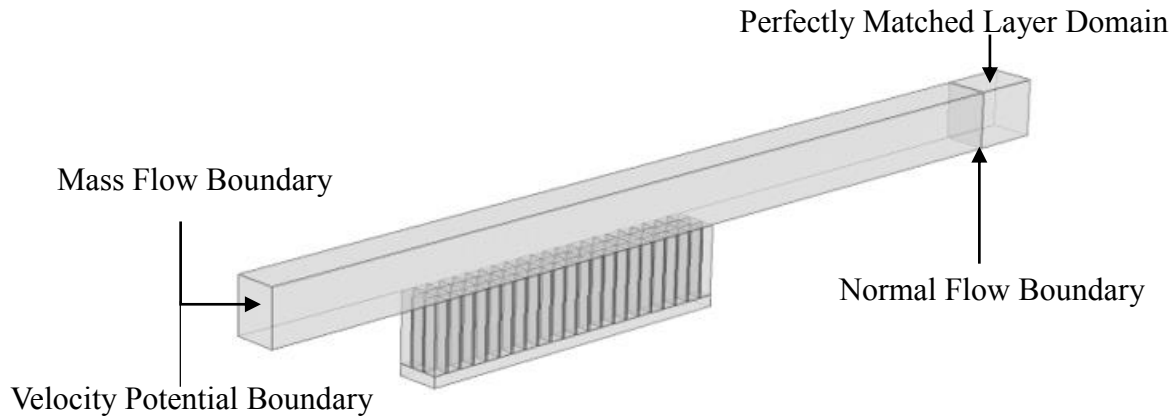


**Figure 8.** Boundary conditions used for COMSOL models incorporating flow

## 2.4 Liner Boundary Conditions

### 2.4.1 Surface Impedance

The liner itself can be modeled using an experimentally determined surface impedance value  $Z(\omega)$ ; however, this requires prior knowledge of these values from additional testing or outside information. In COMSOL, the surface impedance node allow for an input of the impedance as a real or complex number. The equation for the acoustic impedance is given as below [31]:

$$\frac{Z}{\rho c} = R + i\chi \quad \text{Eq. (31)}$$

where  $R$  is the resistance and  $\chi$  is the reactance. As the acoustic impedance is the most essential parameter in predicting the performance of the liner, it proves very sensitive to the overall analysis. The idea of a surface impedance can be looked at multiple ways depending on the liner that it is defining. For the validation case, a constant depth liner was evaluated where the impedance values were ‘smeared’ as to represent the impedance over the entire length and width of the liner [6]. This parameter will always vary for each frequency, but can be simplified in this manner for a liner thought of as being smeared. An image of the surface defined on the liner setup is shown below:

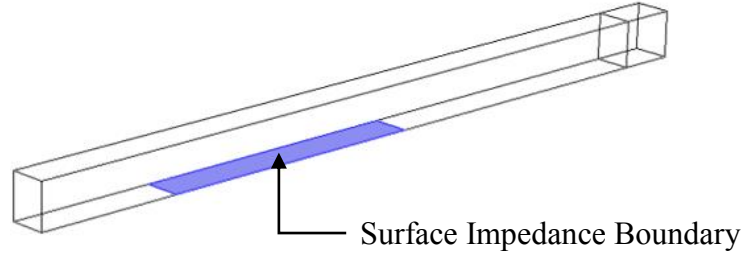


**Figure 9.** Location of surface impedance boundary on duct for COMSOL model

#### 2.4.2 3-D CAD

The most practical approach to modeling the liner however is to construct the 3-D CAD to exact dimension and material structure. As a typical liner system has a porous facesheet and single layer of cellular separator cells, there are multiple boundaries that need to be defined. With this method, the liner core or ‘wall thicknesses’ are defined by an interior impedance. For example, the material used during the validation cases was Accura 60 Plastic. This plastic has a density of 1210 kg/m<sup>3</sup> and Young’s Modulus E of 2895 MPa. The speed of sound traveling through the material is calculated as:

$$c = \sqrt{\frac{E}{\rho}} \quad \text{Eq. (32)}$$

Therefore, the interior impedance value given was  $\rho c$  as 187.187 kPa·s/m<sup>3</sup>.

The facesheet of the liner can be modeled in two different ways. As a built-in feature, an interior perforated plate can be defined that includes the input of the following parameters: area porosity, hole diameter, plate thickness, dynamic viscosity, end correction factor (0.25\*hole diameter), and flow resistance. If these parameters are known, it is must simpler to define the facesheet in this manner. An interior impedance node can be used as well by inputting the equation of the plate’s impedance which is given below as:

$$Z = \rho c \left[ \left( \frac{1}{\sigma} \sqrt{\frac{8\mu(\frac{\omega}{c})}{\rho c}} \right) \left( 1 + \frac{t_p}{dia_h} \right) + \theta_f + i \left( \frac{\omega}{c} \right) \left( \frac{t_p + \delta_h}{\sigma} \right) \right] \quad \text{Eq. (33)}$$

where  $\sigma$  is the porosity,  $\mu$  is the dynamic viscosity of air,  $c$  is the speed of sound,  $\omega$  is the frequency,  $dia_h$  is the hole diameter of the facesheet,  $\theta_f$  is the flow resistance,  $t_p$  is the plate thickness, and  $\delta_h$  is the end correction factor. As well as defining the facesheet in this manner, is it possible to define the micro-perforated plate (MPP) in this way. Depending on the fineness of the facesheet, the plate and holes can be physically built as well rather than defined in the previous way. Keeping in mind however that this creates additional mesh volume along with computation time, for simplicity reasons, the interior perforated plate will mostly be used while in this physics.

The remaining exterior walls of the duct along with liner are by default sound hard therefore signifying the lack of pressure wave transmission through those walls. Figure 10 below shows the typical defined boundaries of the liner.

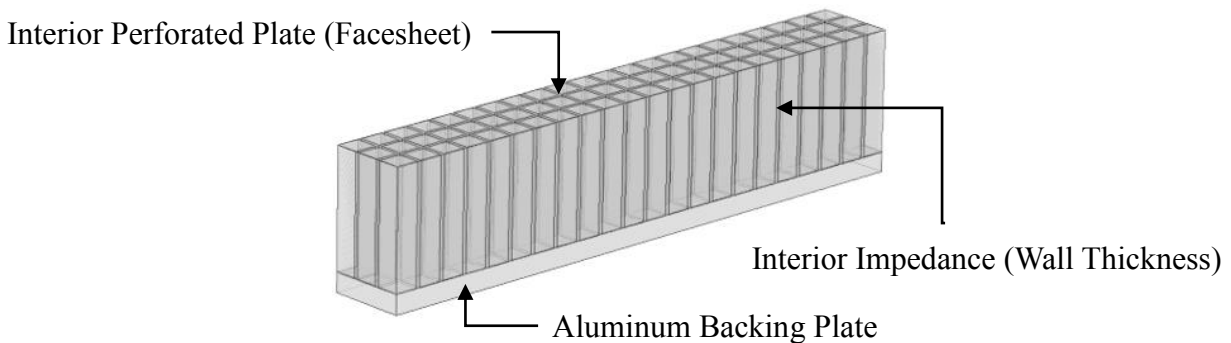


**Figure 10.** Boundary conditions in COMSOL demonstrating liner surfaces

## 2.5 Optimization Module

An additional optimization solver based on the Nelder-Mead method is used towards the end of the research. This solver is a derivative-free method that is appropriate for the optimization analysis explored [32]. In contrast to other optimization techniques, this direct-search method relies solely on the output of the objective function on a set of points. These calculations are therefore simple and more effective since they operate on the worst point rather than the best. Allowing for an input objective function, this tool can either minimize or maximize the function



given. The optimality tolerance chosen is 0.005 which is applied relative to each control variable after scaling with its corresponding specified scale. The maximum number of objective evaluations is set to 1000. Relying on a simplex of  $N+1$  points, where  $N$  is the number of control parameter, it aims at improving the worst point in the simplex by reflections. Moreover, it respects the lower and upper bounds in the control variable space by restricting the length of the reflections. To be more specific, the reflection is calculated as follows:

Compute the reflected point:

$$x_r = x_0 + \alpha(x_0 - x_{n+1}) \quad \text{Eq. (34)}$$

If the reflected point is better than the second worst, but not better than the best, i.e.

$$f(x_1) \leq f(x_r) < f(x_n) \quad \text{Eq. (35)}$$

then obtain a new simplex by replacing the worst point  $x_{n+1}$  with the reflected point  $x_r$  and reorder the values. This approach can be used to find optimum design features such as structural parameters for a given shape. The two objective functions that will be utilized in this optimization module are the transmission loss and the intensity. The transmission loss will be maximized while the sum of the sound intensity leaving the duct will be minimized.

## 2.6 Mesh Properties

A mesh quality can directly affect the accuracy of the results. When performing acoustic analyses in solving the Helmholtz equation, the maximum element size is a function of wavelength  $\lambda$ , the frequency computed  $f$ , and the number of cells. Only one time scale exists and it is set by the frequency  $T = 1/f$ . Several length scales exist such as the wavelength  $\lambda = c/f$ , the smallest geometrical dimension  $L_{\min}$ , the mesh size  $h$ , and the thickness of the acoustic boundary layer. As

a rule of thumb for acoustics, the recommended number of cells is between 5 and 10 elements [24]. This relationship is seen below in equation 35.

$$\text{Maximum Element Size} = \frac{\lambda = \frac{c}{f}}{\# \text{ of cells}} \quad \text{Eq. (36)}$$

Table 1. Mesh Properties for acoustic problem

<b>Maximum Element size</b>	343/2600/5 = 0.02638
<b>Minimum Element size</b>	343/2600/10 = 0.01319

## 2.7 Design Equations

The two main equations evaluated throughout the process to characterize performance are transmission loss (TL), and absorption coefficient ( $\alpha$ ). The TL accounts only for the pressure lost out the exit of the duct, while the absorption focuses in addition on the amount reflected out the incident direction. Transmission loss is calculated below from the following equation:

$$TL = 20 \log_{10} \left( \frac{P_0}{P_{transmitted}} \right) \quad \text{Eq. (37)}$$

where  $P_0$  is taken to be 1 Pa and  $P_{transmitted}$  is the transmitted pressure amplitude through the exit of the duct [33]. This setup in COMSOL uses an average operator on the exit surface that measures the average pressure, hence the transmitted pressure. Equating the absorption coefficient in COMSOL utilizes this average pressure surface and an additional average operator surface. The surface perpendicular to the liner right before it initiates is defined as  $p_1$ . Figure 11 below displays the location of this surface:

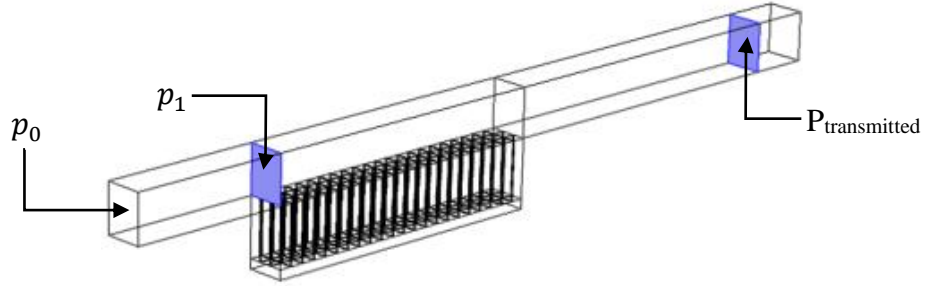


**Figure 11.** COMSOL boundaries showing where pressure surfaces are taken for TL and  $\alpha$ . Therefore, the equation shown below is used to solve for the absorption coefficient, noting that this value cannot be greater than 1.

$$\alpha = \frac{p_0^2 - p_r^2 - p_{transmitted}^2}{p_0^2} \quad \text{Eq. (38)}$$

where the reflected pressure amplitude squared is

$$p_r^2 = p_0 - p_1 \quad \text{Eq. (39)}$$

This absorption coefficient definition is used in additional work from Beck et al. [34]

There will be additional important plots such as the sound pressure level on the opposite wall of the liner as the wave travels down the duct, along with surface pressure plots and isosurface plots to examine how the wave travels not only out the exit but over the entire length of the duct. Using these it will be possible to optimize and advance the design of an acoustic liner.

## 3 EXPERIMENTAL VALIDATION

### 3.1 Experimental Test Section Description

All experimental testing supporting this study was performed using the Grazing Flow Impedance Tube (GFIT) as well as the Normal Incident Tube (NIT) at the NASA Langley Research Facility in Hampton, VA.

#### 3.1.1 Grazing Flow Impedance Tube

This GFIT facility has been used to evaluate acoustic liners in realistic aeroacoustic environments for over 20 years. It has the capability to operate in inlet and exhaust configurations to model flow as well as no flow. The flow path is comprised of a 2.0 inch by 2.5 inch cross-section, with a total duct length of 50 inches [35]. Liners up to 24 inches long and 3 inches deep can be evaluated. This geometry was chosen to ensure the control of higher-order modes, depending on the frequency desired. When the propagation angle deviated from the duct axis, these modes will propagate. This non-uniform pressure distribution propagates with a different wavelength along the central axis for a given excitation frequency. Each mode has a cut-off frequency below which the wavelength is imaginary and hence propagation is not possible [36]. The GFIT components include a source section consisting of eighteen 120-W acoustic drivers, the test section, a probe traverse section, and an upstream and downstream near-anechoic settling and termination chamber [37]. An image depicting the experimental setup and GFIT are shown below in figure 12.

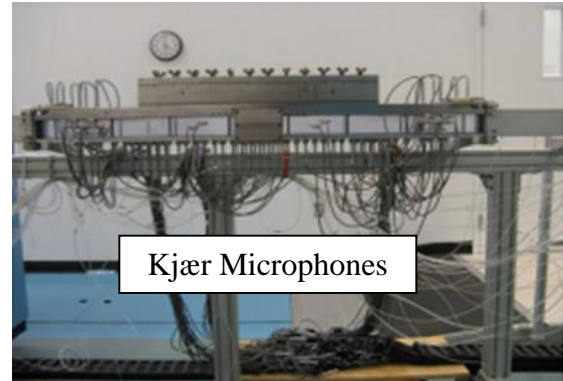


**Figure 12.** Grazing Flow Impedance Tube (GFIT): (left) Main floor of GFIT with flow from left to right; (right) microphone instrumentation

As seen from the figure in the above right, there are a total of 95 microphones spaced thoroughly 0.5-2 inches apart on the centerline wall opposite the liner. These Kjær Type 4938 microphones measure the complex acoustic pressures along the axial length. The pressure readings will be beneficial in creating sound pressure level and phase plots as to observe performance of the wave radiating down the duct.

When flow is tested, the waveguide can operate up to speeds of Mach 0.6 under ambient conditions. This is accomplished by balancing the pressure in the test section from high pressure air upstream of the test section and a vacuum blower downstream of the test section. By careful precision, the high-pressure air entering the test rig is heating to achieve an adiabatic wall condition. Therefore, no heat can enter or exit the duct once this pressure is balanced. The termination consists of a near-anechoic diffuser. With a total of 18 acoustic drivers, a sound pressure level up to 160 dB can be achieved in a frequency range of 0.4 to 3.0 kHz. An additional image of the GFIT is depicted in an artist's drawing below in figure 13.



**Figure 13.** Artist's depiction of Grazing Flow Impedance Tube

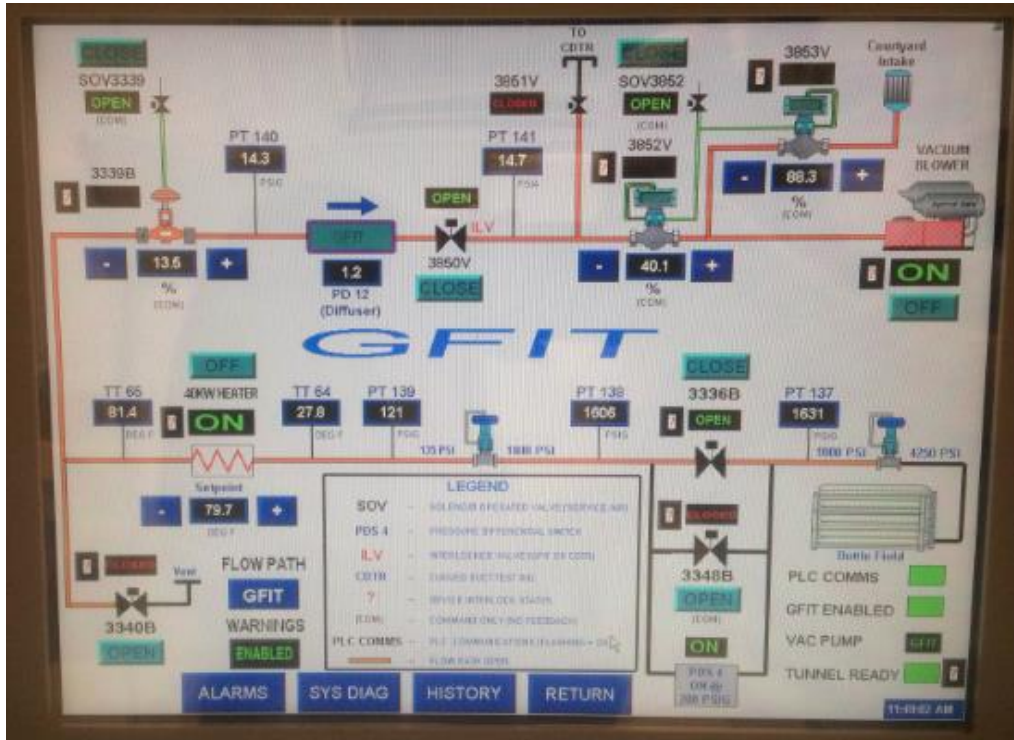


**Figure 14.** GFIT GUI displaying the control of the test section in conjunction with LabView code

Figure 14 above shows a diagram of the GUI interface of the flow path. The GUI is carefully monitored to keep consistent ambient temperature as well as pressure when the flow is turned on. A PC using LabView data analysis software performs the spectral analysis and computes the acoustic pressure at each microphone. Each frequency tested takes approximately 2 minutes to compute. Once the testing is completed, the data is outputted into an excel spreadsheet containing the readings from all of the microphones. The output file gives the sound pressure level and phase at each microphone reading that is then used as input into COMSOL for the total pressure setting at the source and exit planes. With the addition of flow, the output file will also

give the static pressure, total temperature, ambient temperature, average Mach, and Mach at the centerline on the wall opposite the liner. These are then used as input into the COMSOL modeling.

### 3.1.2 Normal Incidence Tube (NIT)

The NASA Langley Normal Incidence Tube (NIT) is a 0.5 m-long, 50.8 mm x 50.8 mm waveguide, used to measure the normal incidence acoustic impedance of the liner in the absence of flow [38]. For this current study, frequencies of 0.4-2.6 kHz in steps of 0.1 kHz were investigated. Six, 120-Watt drivers generate acoustic plane waves that travel down the duct and impinge the liner in the normal plane. There are a total of three microphones; one used as the reference microphone and the two others are for measurement purposes. By taking the average of two transfer functions between the microphones, the calibration factors values then allow for the progression onto the Two-Microphone Method (TMM) [38] that further reduces the impedance values. This method consists of a sample mounted at one end and a sound source at the other end as seen in figure 15 below. The sample is installed in an enclosure that does not allow any leakage of sound outside the test domain. An acoustic driver is mounted on one end to generate a plane wave, while the sound pressure level at the reference microphone is set to 120 dB for each frequency. Once these waves reflect from the liner, there are two microphones that measure the acoustic pressure. The frequency response function is computed between the two microphones and then is further used to calculate the reflection coefficient. In order to make this calculation, the location of the microphones as well as the atmospheric temperature must be used as well, solving for the reflection coefficient as

$$R = \frac{\hat{H} - e^{-jks}}{e^{jks} - \hat{H}} e^{j2k(l+s)} \quad \text{Eq. (40)}$$

where  $\hat{H} = E \left[ \frac{\widehat{G}_{12}}{\widehat{G}_{11}} \right]$  is the estimated complex frequency response function between the two microphones [39].  $E[\ ]$  is the expectation operator,  $\widehat{G}_{11}$  is the estimated auto-spectrum of microphone 1, and  $\widehat{G}_{12}$  is the estimated cross spectrum between the two microphones. In addition,  $k$  is the wave number,  $l$  is the distance from the sample to the nearest microphone, and  $s$  is the spacing between both microphones. Once this value is solved for, the normalized specific acoustic impedance is then calculated by

$$\xi = \theta + j\chi = \frac{Z_1}{Z_0} = \frac{1+R}{1-R} \quad \text{Eq. (41)}$$

where  $Z_1$  is the measured specific acoustic impedance of the sample,  $Z_0$  is the characteristic impedance of the medium through which the fluid travels,  $\theta$  is the normalized resistance, and  $\chi$  is the normalized reactance.

These acoustic impedance values are consistent when testing in the grazing flow impedance tube as well as any normal incidence tube. This is due to the fact that only the normal velocity component is used to calculate acoustic impedance; therefore any other directional velocity component as would be seen in the grazing flow duct can be disregarded. Many experiments are performed in this manner as to then compare the measured impedance data to analytically computed impedance measurements. A 2D schematic diagram of the NIT test rig is shown below in figure 15.



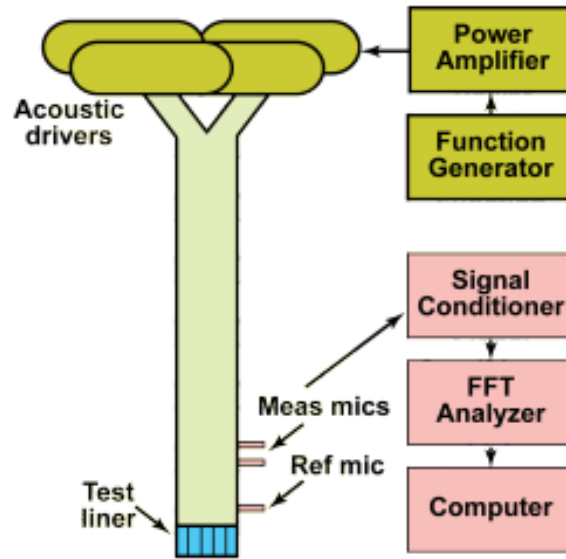


**Figure 15.** Normal Incidence Tube with supporting instrumentation

The experiment conducted in this test section includes an optimized model that will be explained further in sections to follow. By using the two-microphone method, the normal impedance values are measured first. Following this, the liner is modeled in COMSOL using these smeared acoustic impedance values. The sound pressure level and phase are measured on the sidewall as the wave propagates down the duct, and compared to the analytical results. Once these match up, the liner is modeled in COMSOL using full 3-D CAD to confirm that the model is producing the same sound behavior as did the smeared impedance values. Finally, the impedance spectra are measured on the surface of the 3D CAD to then be compared to the measured data in the NIT. This final step is completed in the following manner. COMSOL uses an average operator on the surface of the liner to measure the admittance, given by the equation below;

$$A = \frac{V_{normal}}{P_{total}} = c + is \quad \text{Eq. (42)}$$

where  $V_{normal}$  is the velocity component normal to the facesheet plane,  $P_{total}$  is the total pressure,  $c$  is the conductance and  $s$  is the susceptance [40]. This value is then normalized to  $\rho c$ . From here the admittance is inverted to compute the impedance as seen in equation 43 below.

$$Z = \frac{1}{A} = \frac{1}{c+is} = \theta + i\chi \quad \text{Eq. (43)}$$

### 3.2 Experimental Validation Models

There are three conventional acoustics liners used as the baseline of the validation process consisting of a constant depth (CD), variable depth (VD), and partial variable depth (PVD) design. To support the validation efforts, these liners were tested using plane wave radiation, incoming at a total SPL level of 130 dB in the GFIT. All liners were consistently placed at a location of 8 inches aft the source plane down the duct. There are 72 square chambers, each of 0.6 x 0.6 in<sup>2</sup> dimension, along with an interior wall of 0.1” thickness. The following photographs below depict their shape along with the corresponding tables giving other geometrical parameters. A schematic diagram of a section of the facesheet is shown below, which is constant for each baseline model.

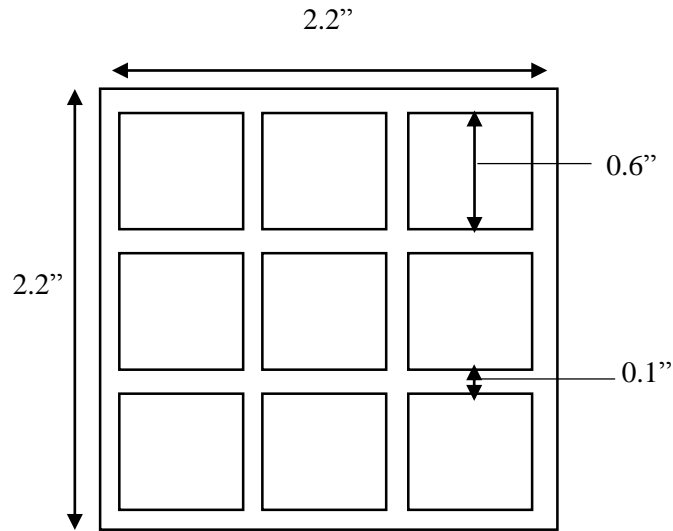


**Figure 16.** Section of facesheet showing geometric parameters

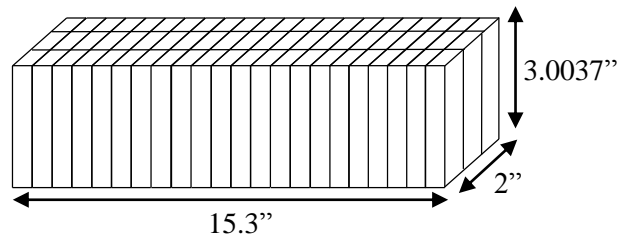
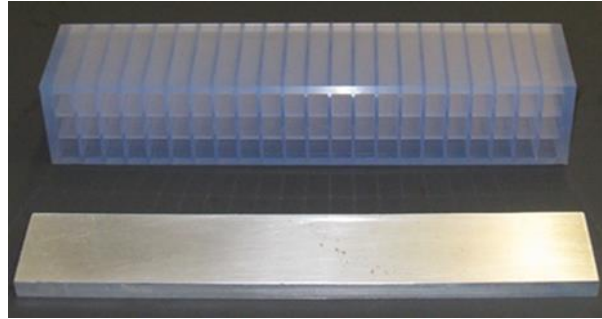


**Figure 17.** Photograph of constant depth liner with aluminum backing plate along with schematic diagram

Table 2. Constant depth liner geometrical parameters

<b>Facesheet</b>	<b>Chambers</b>	<b>Sample</b>
$t = 0.0313''$ $d = 0.0385''$ $N = 1452$ $\sigma = 0.055$	Depth = $3.0037''$ $\# = 3 \times 22$ Dimensions = $0.6'' \times 0.6''$ Interior wall = $0.1''$ thick	Length: Full = $16.0053''$ , Active = $15.3''$ Width: Full = $2.4834''$ , Active = $2.0''$

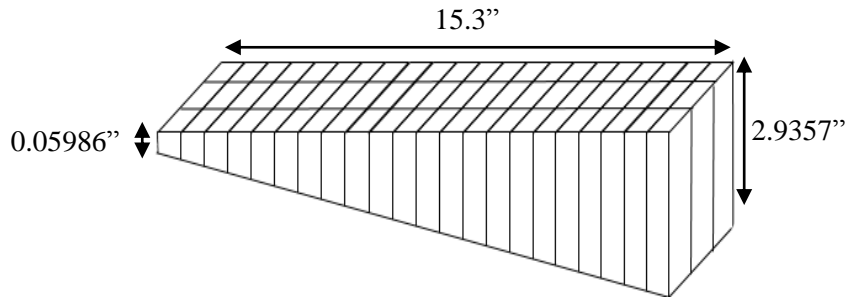


**Figure 18.** Variable depth liner with backing plate along with schematic diagram of dimensions

Table 3. Variable depth liner geometrical parameters

<b>Facesheet</b>	<b>Chambers</b>	<b>Sample</b>
$t = 0.0303''$ $d = 0.0385''$ $N = 1452$ $\sigma = 0.055$	Depth: LE of chamber 1: $2.9357''$ TE of chamber 22: $0.05986''$ $\# = 3 \times 22$ Dimensions = $0.6'' \times 0.6''$ Interior wall = $0.1''$ thick	Length: Full = $16.0051''$ , Active = $15.3''$ Width: Full = $2.4833''$ , Active = $2.0''$

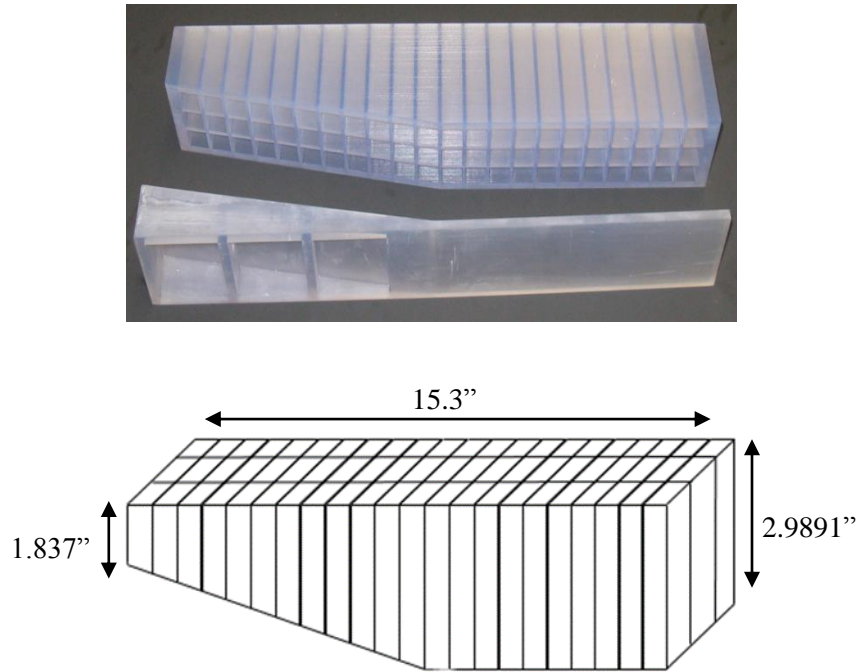


**Figure 19.** Partial variable depth liner with backing plate with schematic diagram of dimensions

Table 4. Partial variable depth liner geometrical parameters

Facesheet	Chambers	Sample
$t = 0.0337''$ $d = 0.0385''$ $N = 1452$ $\sigma = 0.055$	Depth: Chambers 1 – 11: 3.001'' LE of chamber 12: 2.9891'' TE of chamber 22: 1.8370'' # = 3x22 Dimensions = 0.6''x0.6'' Interior wall = 0.1'' thick	Length: Full = 16.0051'', Active = 15.3'' Width: Full = 2.4825'', Active = 2.0''

The constant depth liner was also embedded with melamine foam within each chamber in order to observe porous material behavior experimentally as to compare with the analytical tool. All models are backed by an aluminum plate as seen in figure 20.

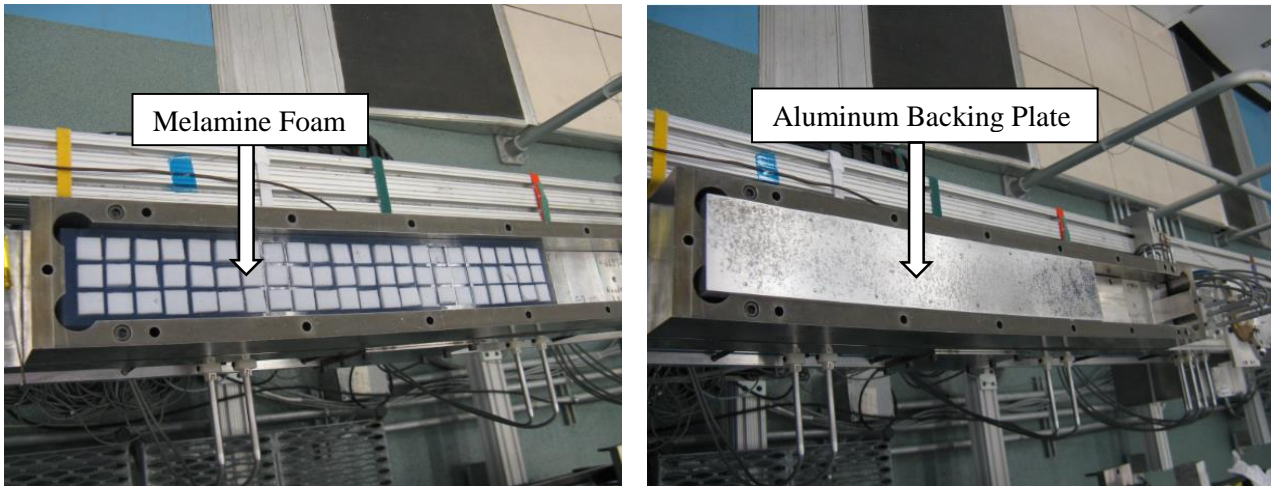


**Figure 20.** Constant depth liner in test section with melamine embedded in test section (left) back by aluminum plate (right)

In addition to the GFIT experiments, the NIT was utilized to measure impedance spectra on a specific optimized liner that will be discussed in chapter 4. The liner was built from the 3D printer at NASA Langley and is shown below in figure 21.

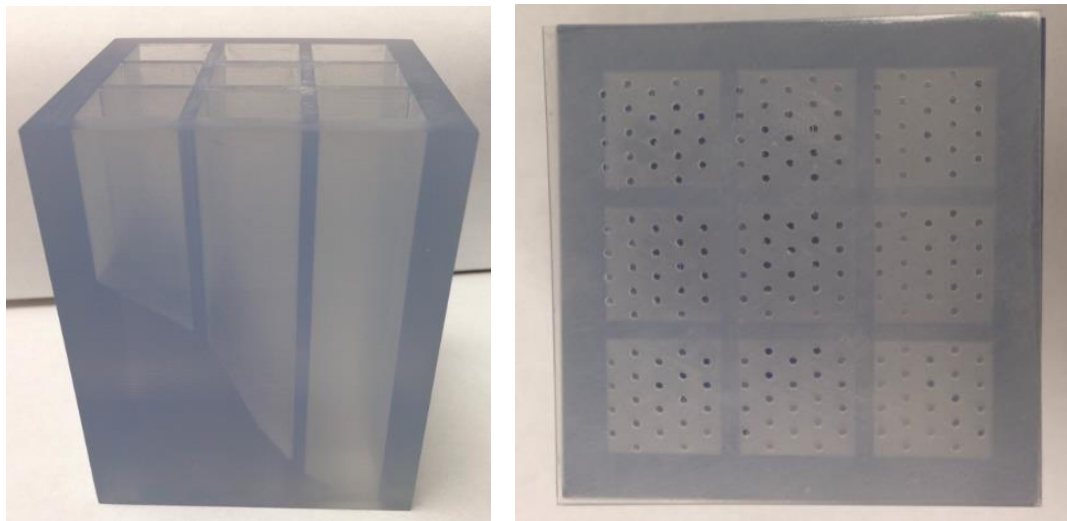


**Figure 21.** 3D printed 2x2 inch optimized NIT sample (left) with printed facesheet (right)

Table 5. Parameters of the optimized NIT sample

<b>Facesheet</b>	<b>Chambers</b>	<b>Sample</b>
$t = 0.03''$ $d = 0.038''$ $\sigma = 0.055$	Depth: LE of chamber 12: 1.43'' TE of chamber 22: 2.94'' # = 3x3 Dimensions = 0.6''x0.6'' Interior wall = 0.1'' thick	Length: Full = 3'', Active = 2.94'' Width: Full = 2.5'', Active = 2.0''

### 3.3 Plane Wave Radiation with M=0 in GFIT

In order to validate the finite element tool, the sound pressure level as well as phase plots are plotted against the experimental results.

#### 3.3.1 Sound Pressure Level Plots

The constant depth, variable depth, and partial variable depth liners are all initially tested with no flow and an incoming SPL level of 130 dB. The incident and exit pressure values are set in COMSOL so the problem is fully bounded at outlined above. Figures 22, 23 and 24 show the SPL plots for the three different liners at frequencies 600, 1200, and 1800 Hz.

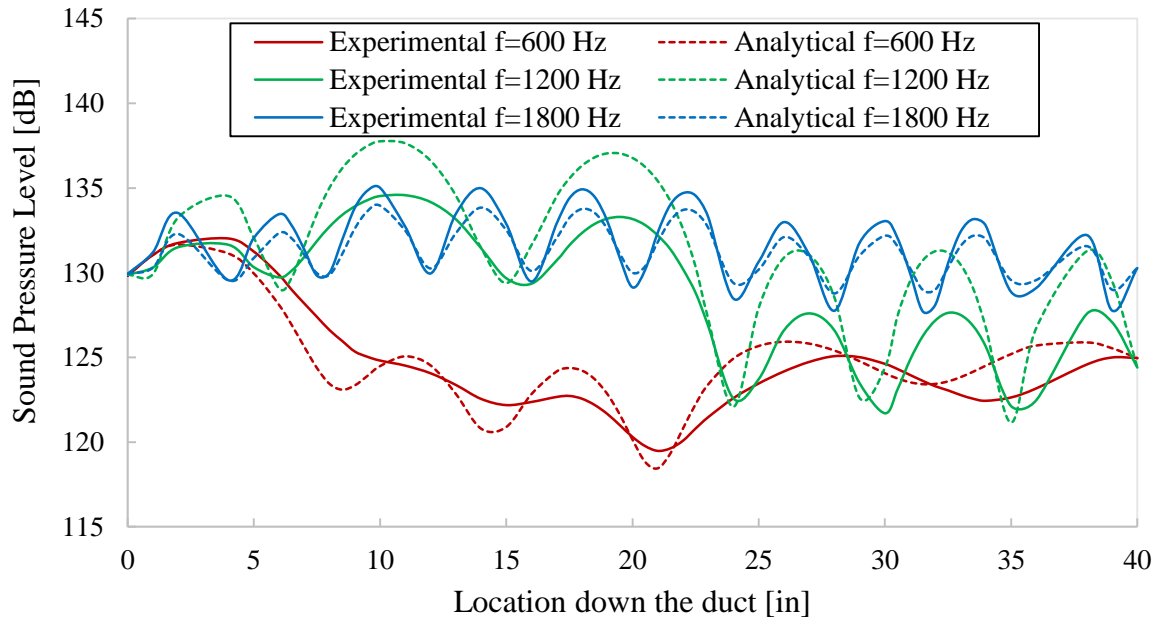


**Figure 22.** Sound pressure level down the duct for frequencies 600, 1200, and 1800 Hz for the constant depth liner

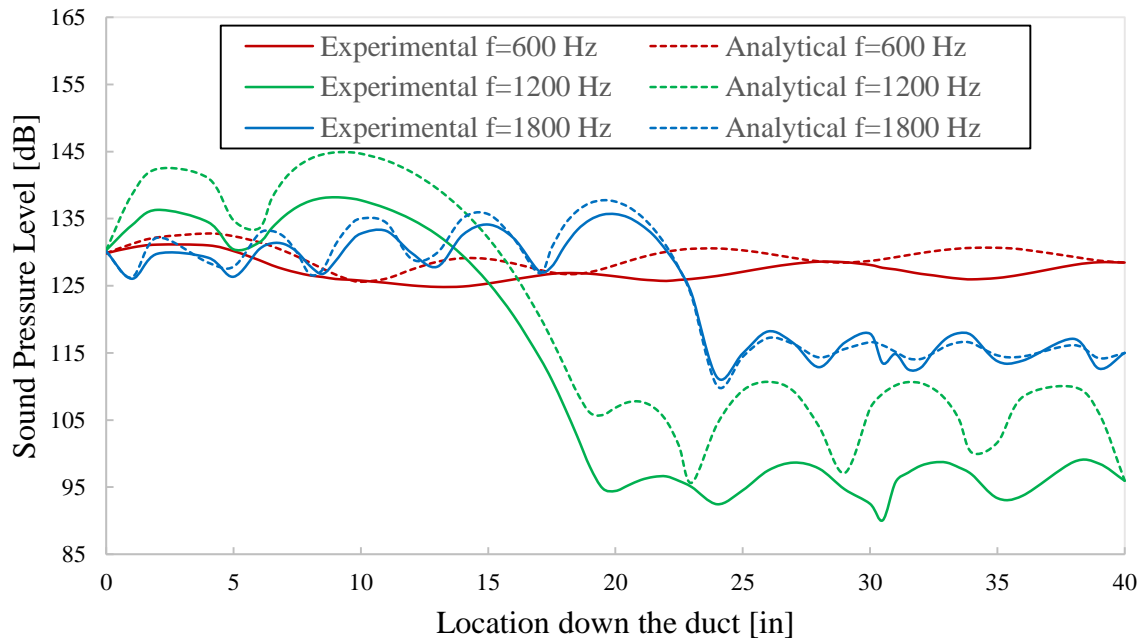


**Figure 23.** Sound pressure level down the duct for frequencies 600, 1200, and 1800 Hz for the variable depth liner



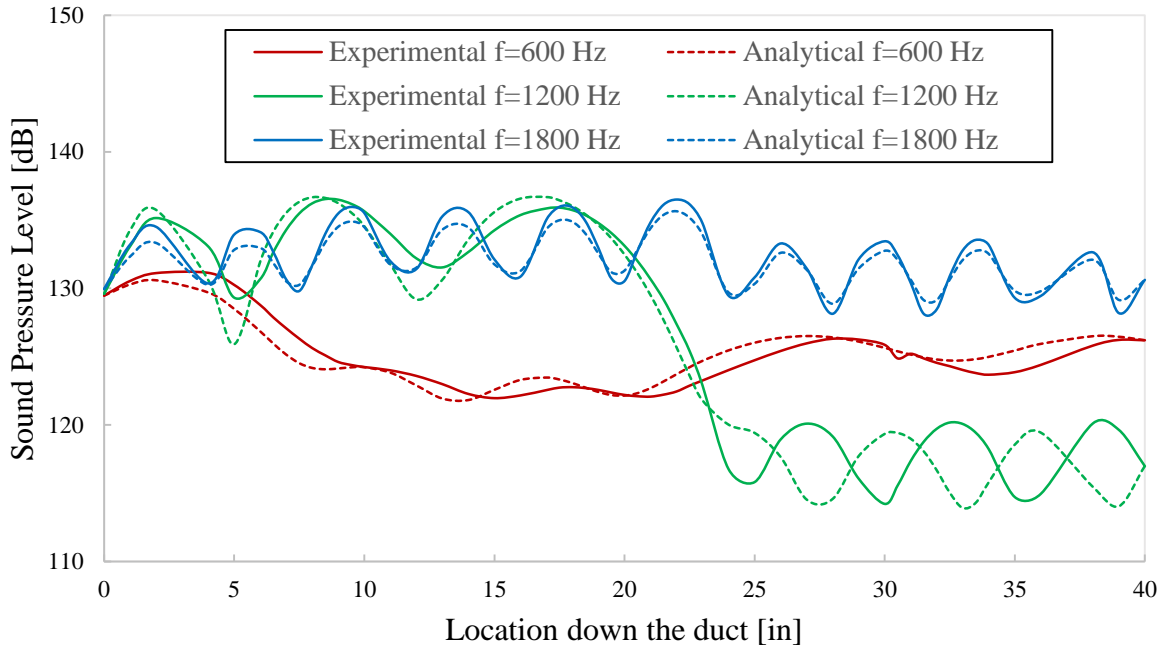


**Figure 24.** Sound pressure level down the duct for frequencies 600, 1200, and 1800 Hz for the partial variable depth liner

The COMSOL results compare favorably against the experimental results. There is no deviation in each graph greater than ~10 dB. In general, the standing waves' amplitude tends to be over-predicted by the analytical tool. This could be due to any sort of viscous effects that the experimental result would show, or error in the precision of geometric measurements. However, for the incident and exit pressure, the experimental and analytical results match up perfectly as they should.

### 3.3.2 Phase Plots

The phase is an important component to validate because it denotes a particular point in the cycle of a waveform. When there are multiple waves interacting, the phase plays a large role in being able to identify their characteristics. In addition, when focusing on active noise control, two identical waves of equal and opposite amplitude will be able to cancel each other out as long

as they are 180 degrees out of phase. The same frequencies are used to demonstrate the phase behavior as the wave travels down the duct and is shown below in figures 25, 26, and 27.

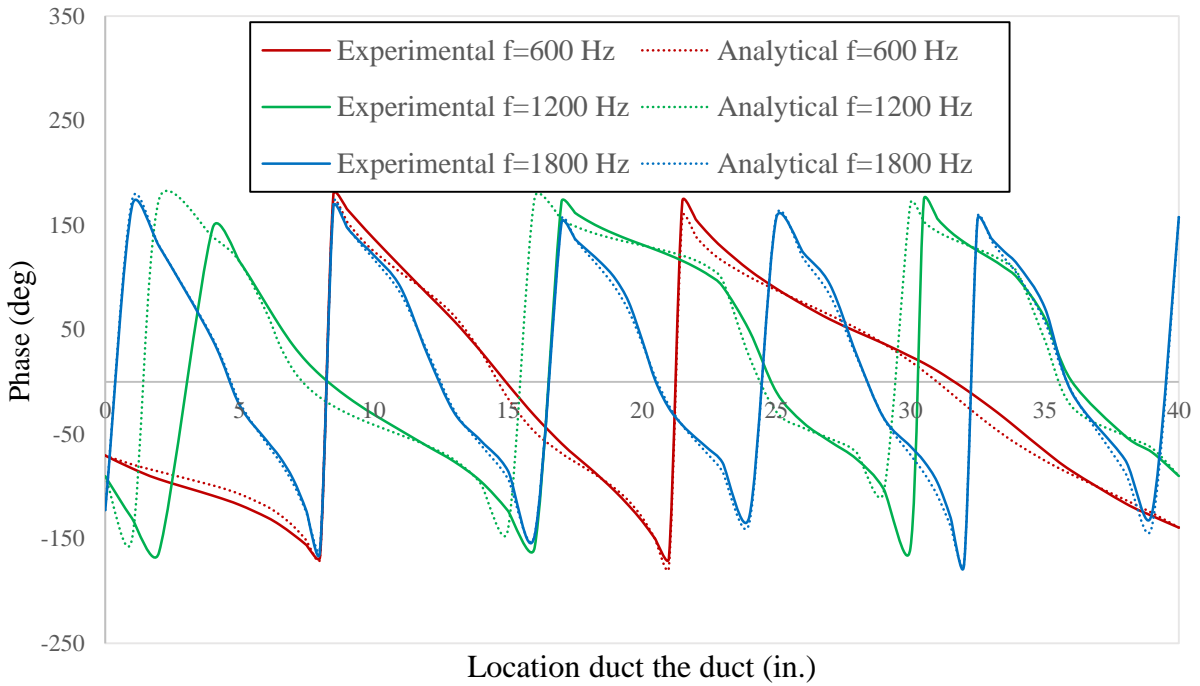


**Figure 25.** Phase down the duct for frequencies 600, 1200, and 2000 Hz for the constant depth liner

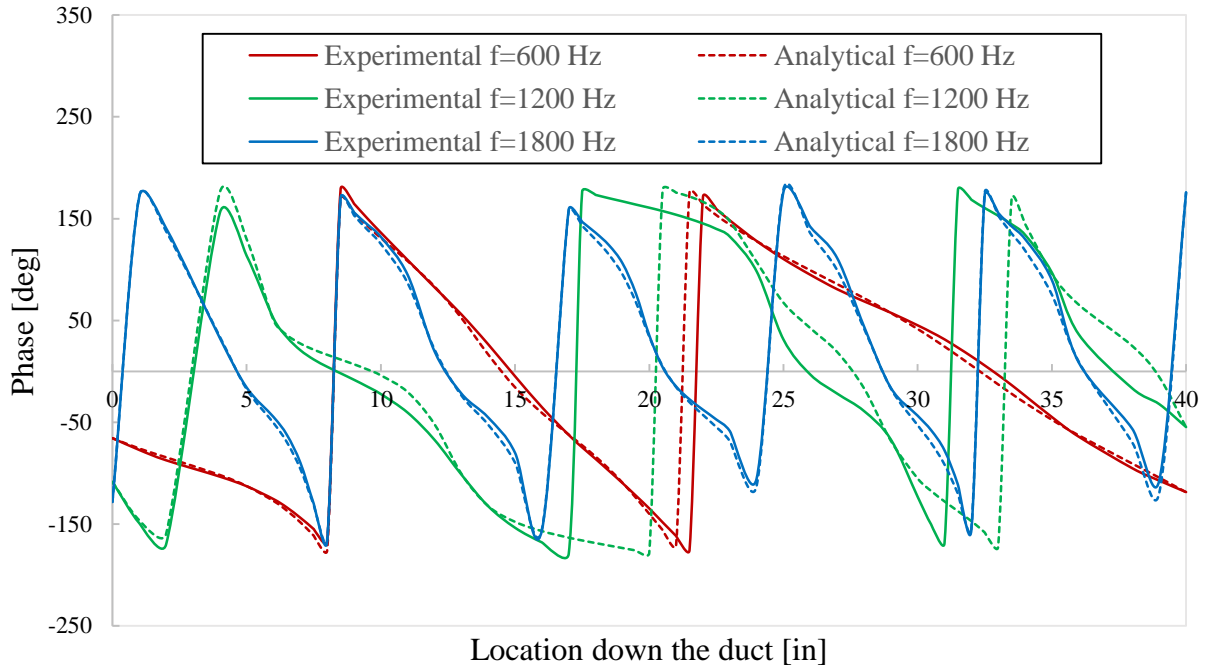


**Figure 26.** Phase down the duct for frequencies 600, 1200, and 1800 Hz for the variable depth liner

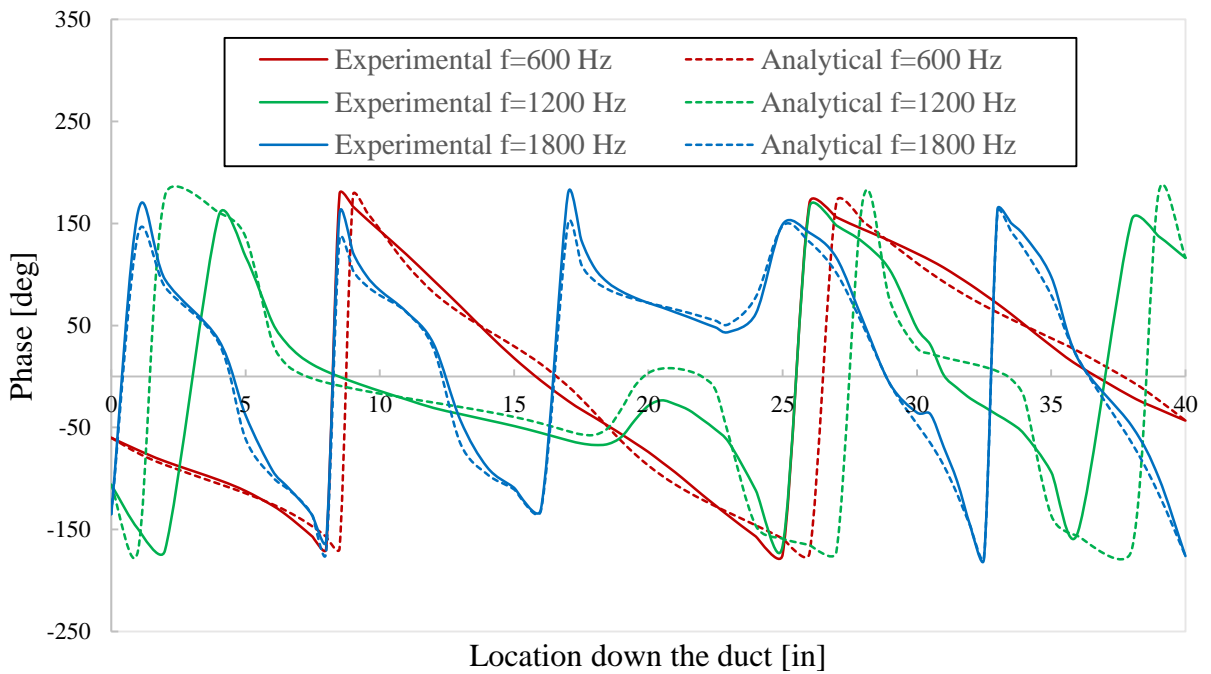


**Figure 27.** Phase down the duct for frequencies 600, 1200, and 1800 Hz for the partial variable depth liner

When the frequency is nearing resonance, a small variation in frequency results in a large phase shift. Looking at the CD and VD plots, nearing 1200 Hz where TL is at a maximum, the phase plots do not match up as well as other frequencies. As the overall results match up very well, the next step is to begin adding porous foam into the design to verify that additional physics are modeled as accurately.

### 3.4 Plane Wave Radiation with melamine embedded and M=0 in GFIT

#### 3.4.1 Sound Pressure Level Plot and Phase plot

The constant depth was then embedded with melamine and tested at 120 dB in order to validate the porous analytical model as well and is shown below. Within each liner core was a  $0.6 \times 0.6 \times 3 \text{ in}^3$  volume of melamine directly inside, giving the total volume of melamine to be  $72 \text{ in}^3$ . The corresponding SPL and phase plots examining 600, 1400, and 2200 Hz are shown below.

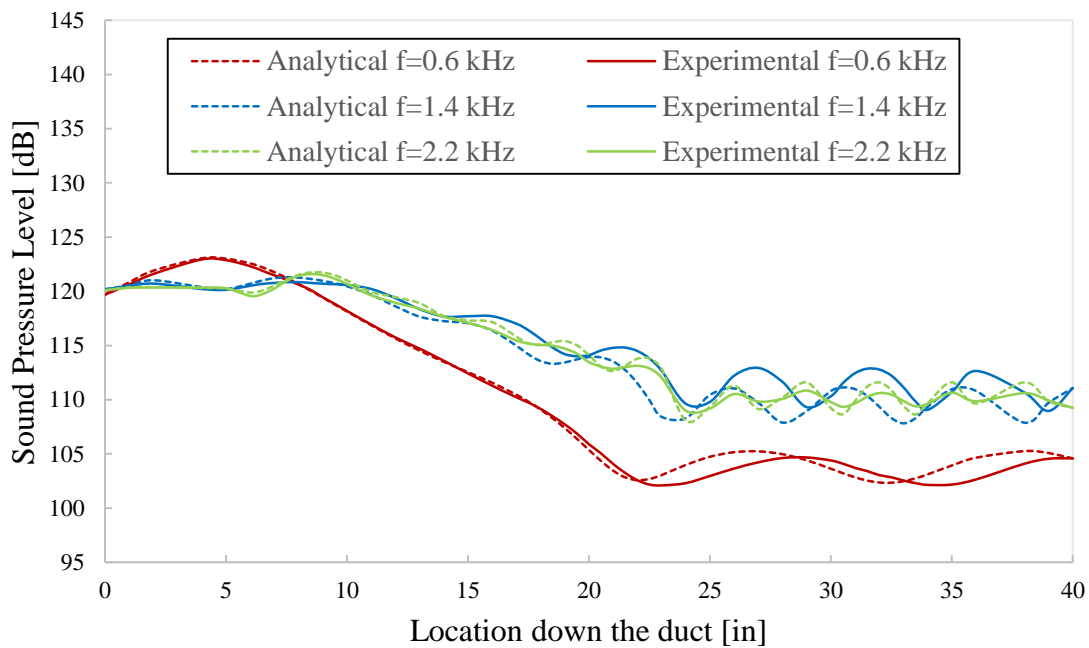


**Figure 28.** Sound pressure level for the constant depth liner with melamine embedded

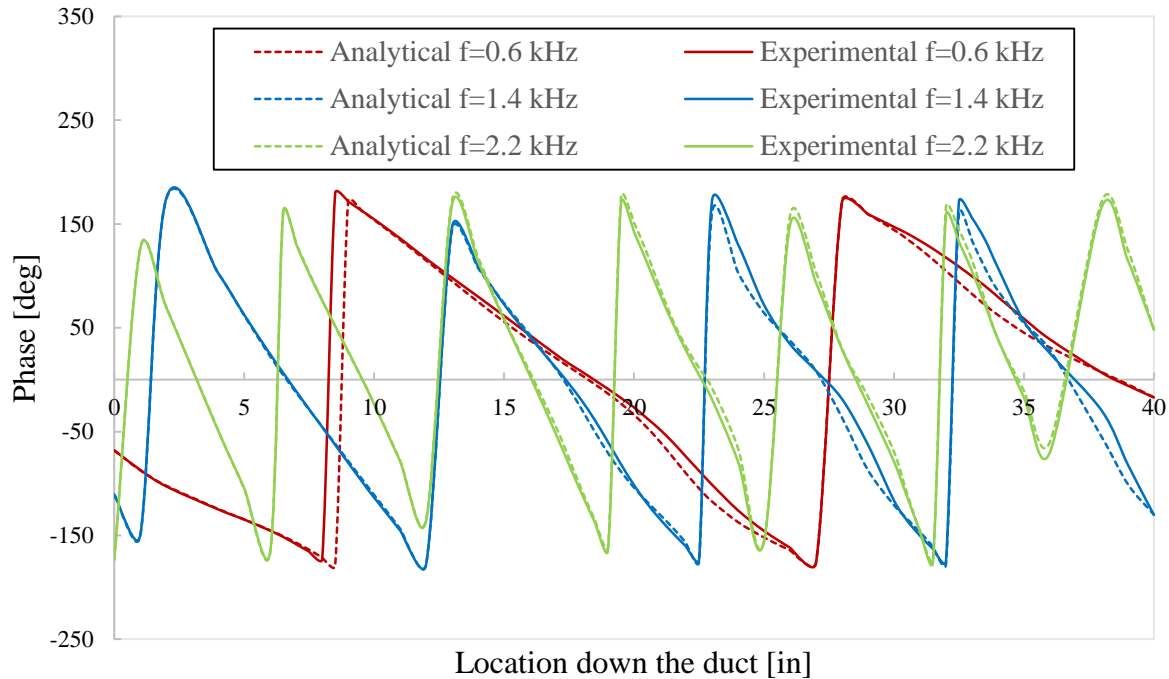


**Figure 29.** Phase plot for constant depth liner with melamine embedded

These results as well show strong agreement with experimental data. Observing just these frequencies, it can be seen that there is already more attenuation produced with the melamine inclusion than without. At 600 Hz, there is approximately 15 dB of attenuation, along with approximately 10 dB for 1400 and 2200 Hz. This is a key step that confirms the properties of melamine, as well as the precision of the poroacoustics physics inclusion.

### 3.5 Plane Wave Radiation with and without melamine and $M=0.3$ in GFIT

As it is crucial to understand the behavior of sound radiating over a liner; it is also important to understand the inclusion of flow and how it effects the liner's ability to attenuate. Two experiments will be performed using the constant depth liner with and without melamine embedded inside the liner cells. This aeroacoustics test is setup the exact same as the previous tests, just with the addition of flow of speed  $M=0.3$ .

In order to validate the analytical tool's ability to model flow properly, the baseline constant depth model was tested in  $M=0.3$  flow with and without melamine. Initially, the impedance values of the liner without melamine were computed using CDUCT [35]. These impedance values are then inputted into COMSOL as a surface impedance model before the full 3D geometry is setup and tested. The total pressure at the source as well as exit must match up in the COMSOL model as it was produced in the experiment. The SPL and phase plots showing frequencies 600, 1000, and 1400 Hz are shown below in figures 30 and 31.

### 3.5.1 Surface Impedance SPL and Phase plots

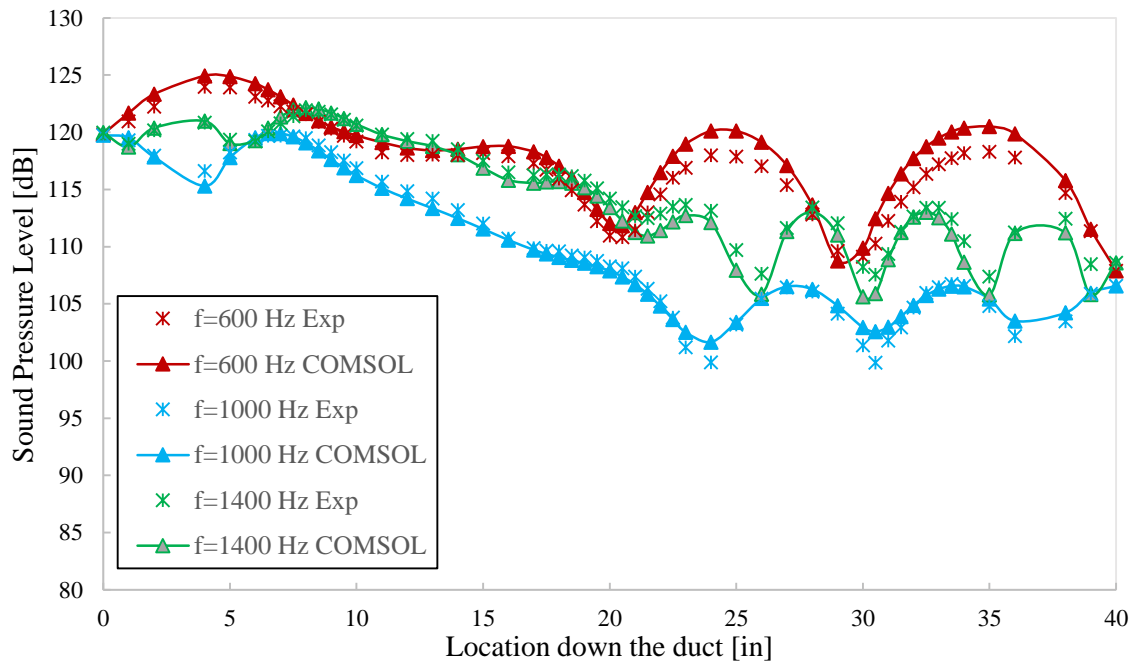


**Figure 30.** Sound pressure level plot of the surface impedance model with  $M=0.3$  flow

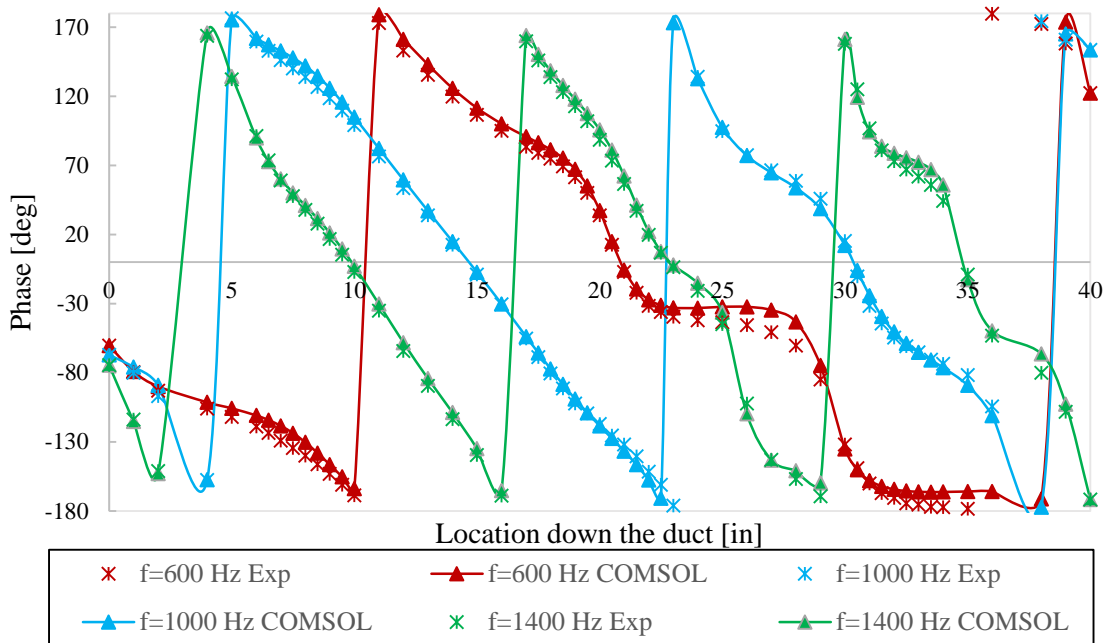


**Figure 31.** Phase plot for the surface impedance model with  $M=0.3$  flow

These results match up almost identically, as they should. In addition, using a surface impedance neglects any additional error due to incorrect geometrical setups. There is approximately 8 dB of attenuation for these specific frequencies. Even with the addition of flow the results prove consistent when comparing to the analytical results. Something important to note is that the incident and exit pressure and amplitudes match up as well. The calculated velocity potential was also an input to this pressure value; therefore the analytical tool solved the gradient of the potential correctly.

### 3.5.2 Full 3D CAD SPL plots without Melamine

The full 3D model was tested as well using the two-parameter approach to model the facesheet. The SPL and phase plots are shown below in figure 32 and 33.

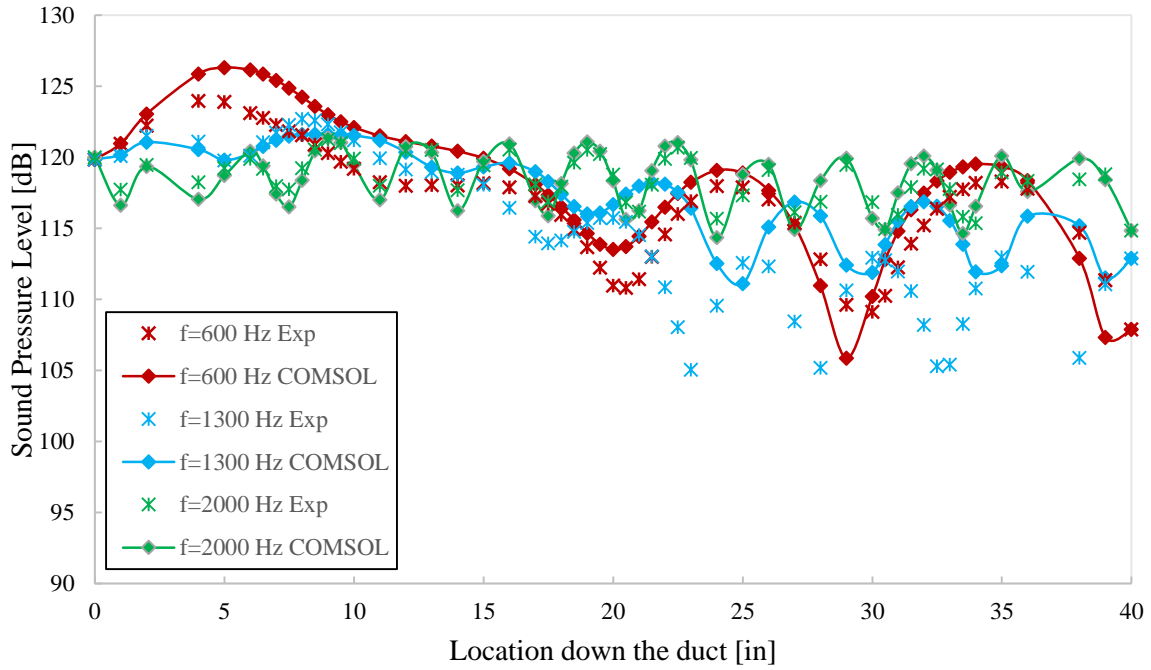


**Figure 32.** Sound pressure level plot for 3D geometry without melamine with  $M=0.3$  flow

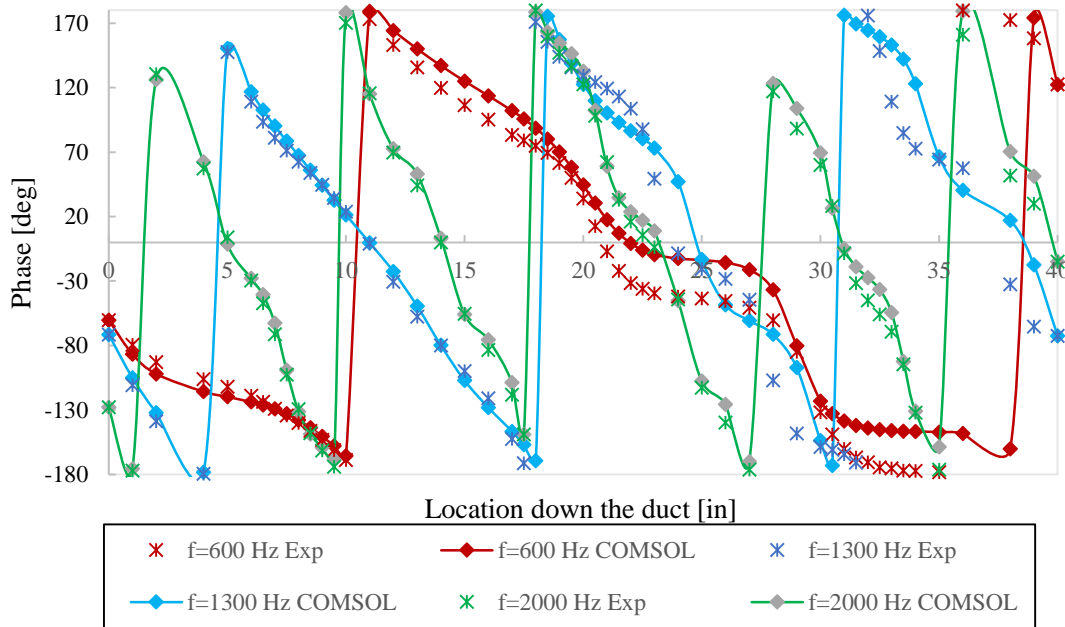


**Figure 33.** Phase plot for 3D geometry without melamine with  $M=0.3$  flow



### 3.5.3 Full 3D CAD SPL and phase plots with melamine embedded

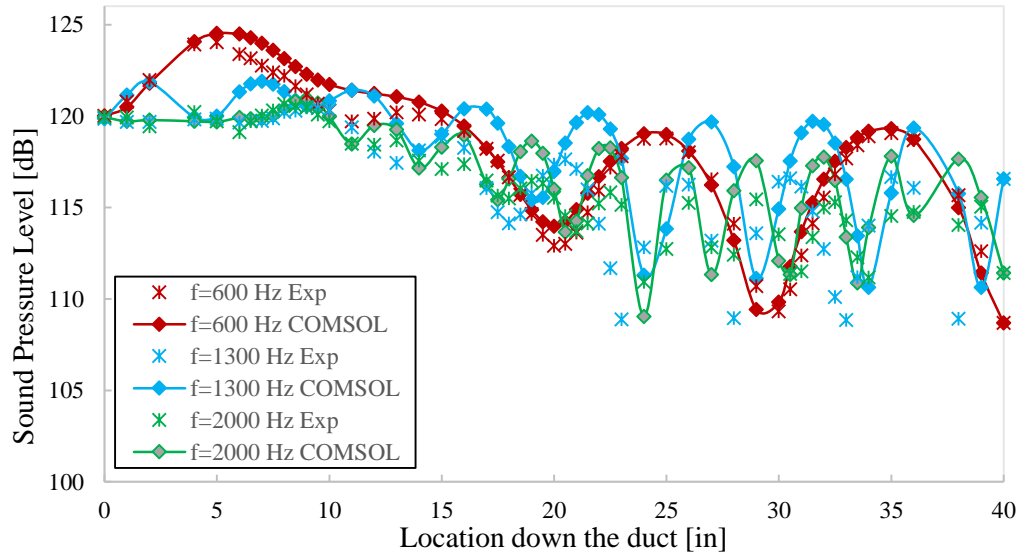


**Figure 34.** Sound pressure level plot for 3D geometry with melamine and  $M=0.3$  flow

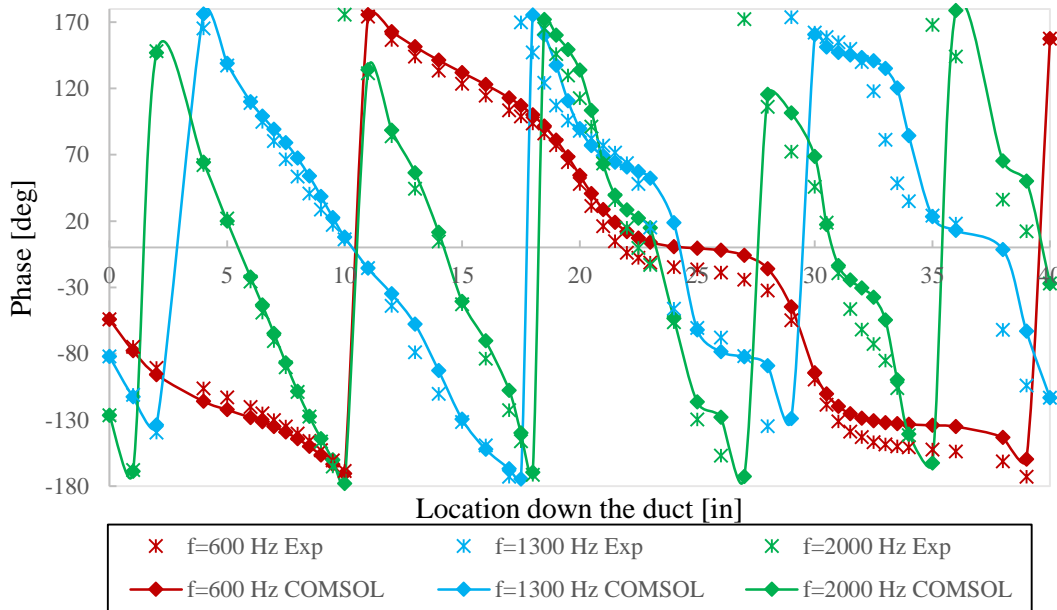


**Figure 35.** Phase plot for 3D geometry with melamine and  $M=0.3$  flow

Observing these graphs with the addition of flow, there shows to be consistent results with the experiment vs. analytical. As did the results without flow, the complex pressure matches up at the

incident and exit planes as well. Something to note is that the inclusion of flow creates less reflection off of the leading edge of the liner which therefore will decrease the peak amplitude of the standing wave right after it leaves the source plane. The amplitude of these waves also shows to be much larger the higher the flow speed. The phase plots show to be more accurate than the no flow cases.

### 3.6 Plane Wave Radiation in NIT

#### 3.6.1 Surface Impedance Sound Pressure Level and phase plots

Using a surface impedance model in COMSOL, the impedance values per frequency were inputted and assumed a smeared surface as the liner. The surface impedance is located as  $x=0$  inches, while the defined total pressure value is set at  $x=6$  inches. The sound pressure level plots for frequencies 400, 1000, and 1600 Hz are shown below.

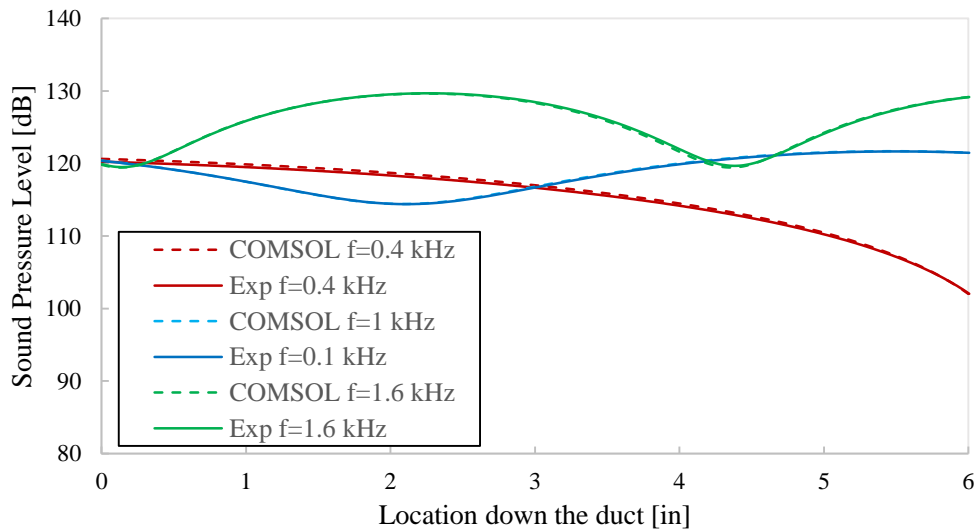


**Figure 36.** Sound pressure level plot for surface impedance NIT model

The SPL level right at  $x=6$  inches is perfectly matching due to the bounded problem. The SPL patterns match almost perfectly as the wave reflects off of the surface and travels back down the duct.

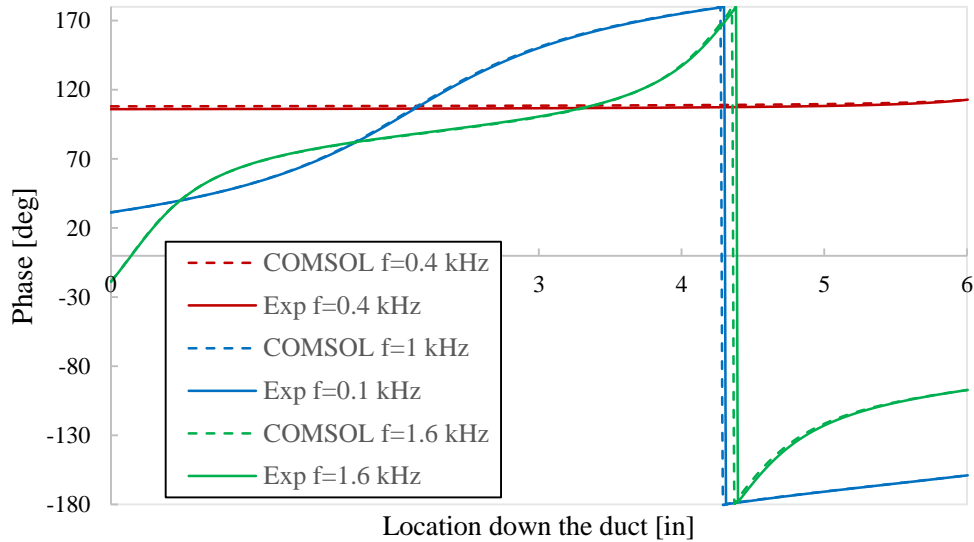


**Figure 37.** Phase plot for surface impedance NIT model

The phase at 400, 1000, and 1600 Hz matches up quite favorably as well. As noted for the SPL plots, right at  $x=6$  inches the phase matches up exactly for the experiment vs. COMSOL. There is a small shift at 400 Hz right at the liner only about 1 dB. The overall length of the NIT was much larger than 6 inches, as shown in the result. This is due to the fact that only 6 inches is necessary to model plane waves with a maximum frequency of 2600 Hz. This corresponds to a wavelength of approximately 5.2 inches. Therefore, 6 inches is plenty to capture the highest frequency.

### 3.6.2 3D CAD Sound Pressure Level and phase plot

Since the SPL and phase plots using the surface impedance values matched up, the correctness of the COMSOL propagation code is confirmed. The full 3D CAD of the optimized liner is then built and tested using the same boundary condition at the source plane. It is expected

that there will be some slight differences due to the code not accounting for viscous effects from the side walls of the duct, as well as possible dimension error of the 3D printed model. The sound pressure level plot is shown below.

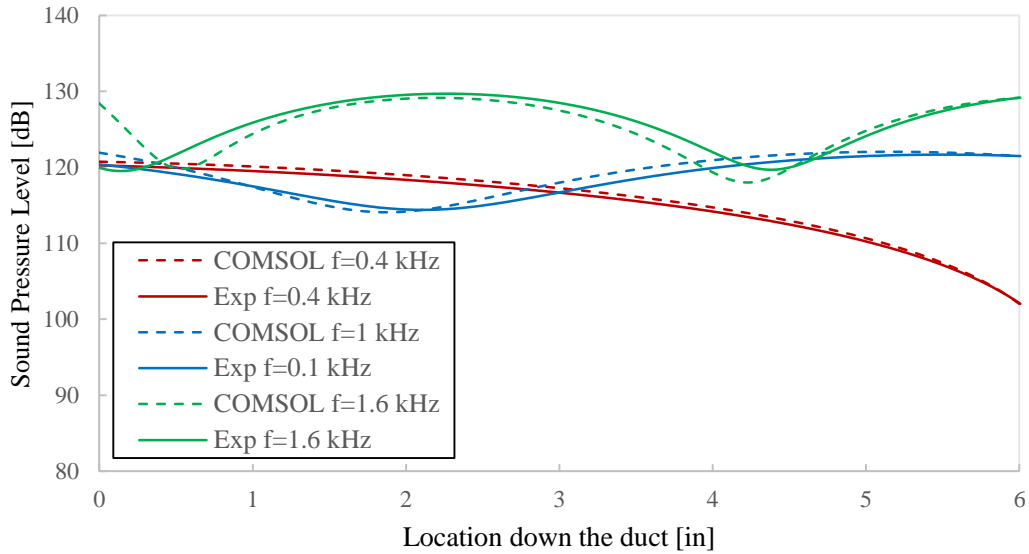


**Figure 38.** Sound pressure level plot for full 3D CAD NIT model

For all three frequencies there shows to be consistent trends as compared to the experimental results. At 1600 Hz however, right at the surface of the liner there shows to be a shift in SPL of about 8 dB. In the upper frequencies the standing wave pattern begins to offset due to the strictness of the bounded problem. The phase plot demonstrates the same behavior as well as seen in figure 39.

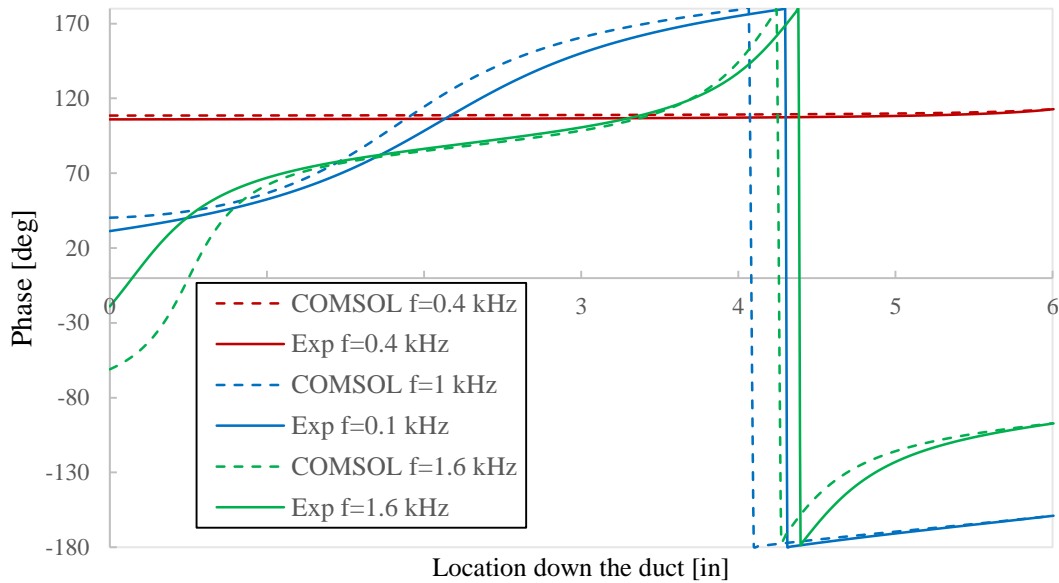


**Figure 39.** Phase plot for full 3D CAD NIT model

In order to examine how closely the measured impedance values matched the calculated impedance values, the resistance and reactance are plotted against each other. The experimental results measured impedance from the two parameter approach, while the analytical tool calculated the average admittance on the surface of the liner and then inverted the value to obtain the impedance. There are also two additional planes located 0.1” and 0.2” above the liner surface to show the impedance behavior as the wave travels farther away from the liner. The resistance and reactance are plotted below in figure 40. The trend shows that the impedance value measured does not identically match the analytical value. However, even by measuring 0.2” away from the plane, the behavior starts to match up more convincingly.

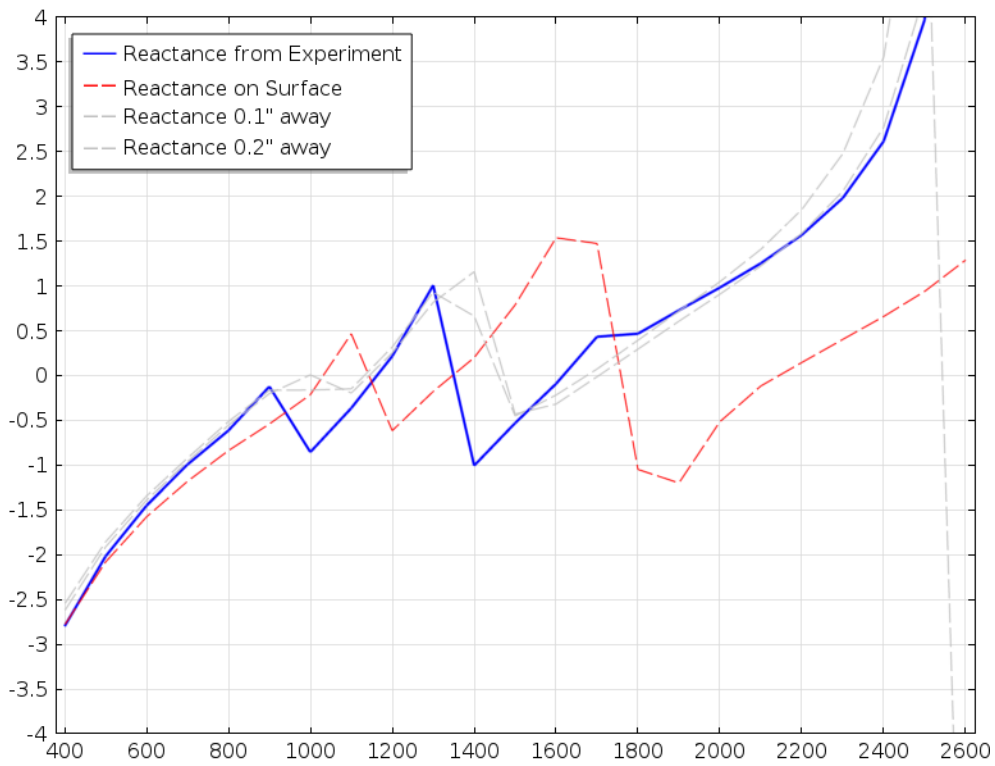
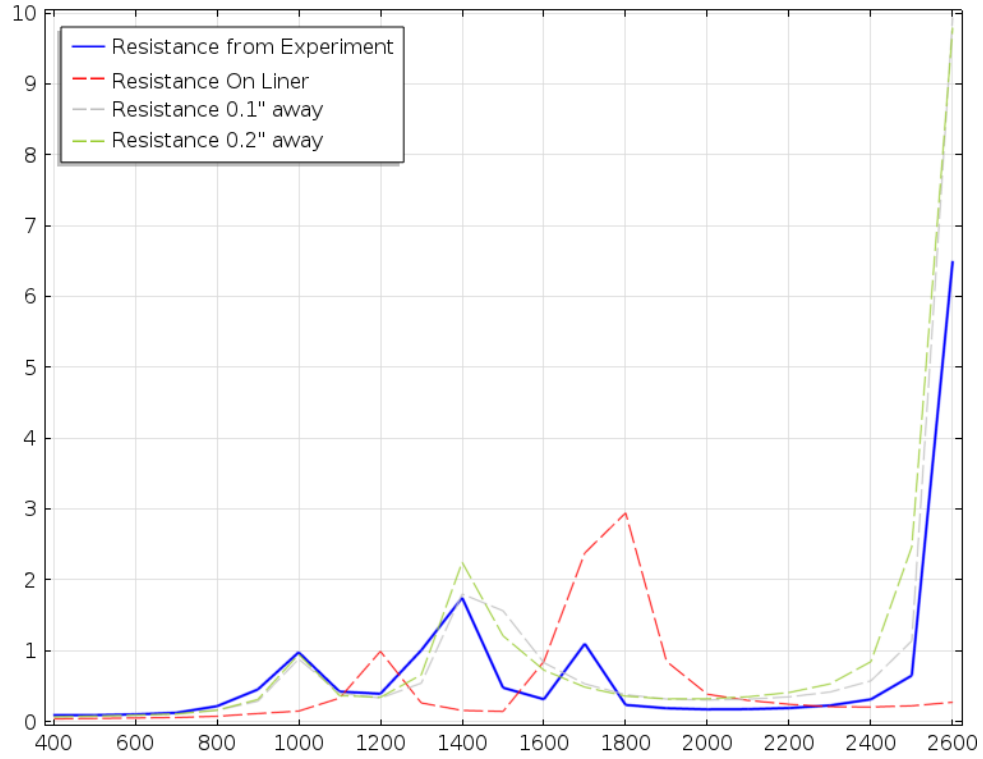


**Figure 40.** Resistance (top) and reactance (bottom) comparing the experimental to COMSOL results

Even though the measured experiment impedance values did not exactly match up to the measured impedance values in COMSOL, the results are still nearly perfect. As well, it takes only about 0.2” off the liner surface for the impedance to begin matching up to the measured impedance values. This error could be due to the constrained setup of the model. The interior perforated plate model in COMSOL that by default models the facesheet, does not take into account any nonlinear viscous effects, which could explain the behavior as well. In addition, this is most likely due to the varying chamber depth and a smeared impedance assumption. The sound pressure at 2500 Hz through the duct and liner is shown in figure 41.

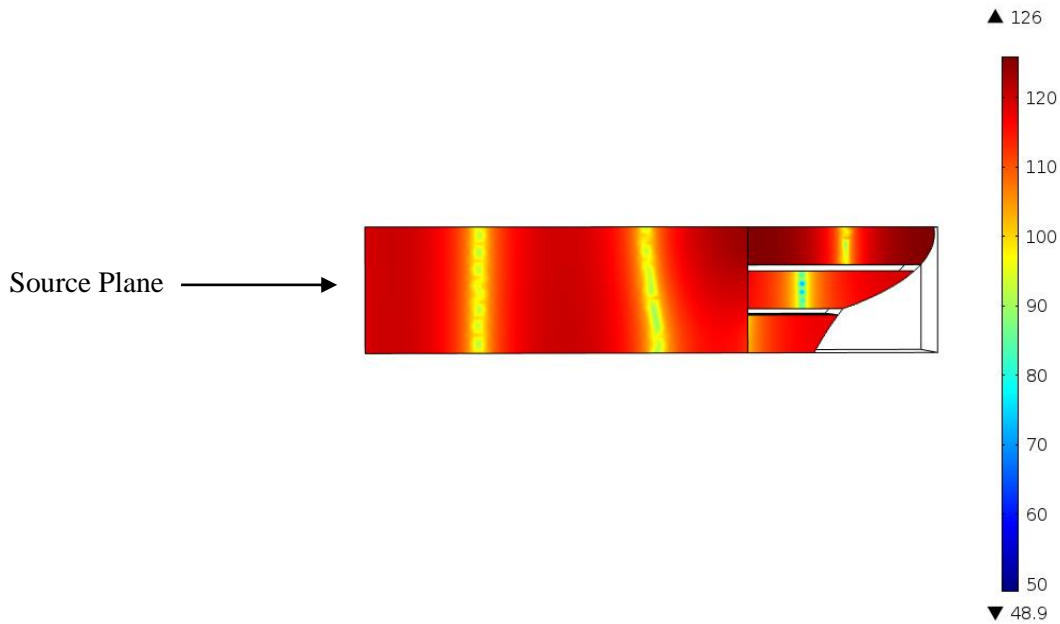


**Figure 41.** Sound pressure level 2D plot for NIT sample at 2500 Hz

## 4 PRELIMINARY STUDIES OF SYSTEM COMPONENTS

The components for noise treatment designs include an acoustic liner, microperforated plates, porous foams such as melamine and polyimide, as well as embedded masses including aluminum spheres that build up to the overall metamaterial system. The design stage begins with a basic shape study using just an acoustic liner and finally builds up to incorporating all components through sensitivity studies as well as optimization tests.

### 4.1. Shape and Optimization Study

Using the base model as a constant depth liner with the same parameters for the facesheet, wall thickness, etc., the study begins with a liner depth sweep. For each design, the broadband performance is quantified by summing the TL over the targeted frequency range as well as a scaled interpretation of the broadband performance by observing the low range from 400-800 Hz and high range from 2200-2600 Hz. The broadband analysis is done by evaluating how many frequencies give at least ~10 dB of attenuation. All models have the same geometric properties as the constant depth liner that was used for validation studies. Refer to table 2 for these properties.

#### 4.1.1. Constant Depth Extrusion

The initial test is a constant depth extrusion, varying the depth up to a maximum magnitude of 3 inches. In order to capture attenuation over an entire frequency range, it is necessary to understand how depth affects pressure loss. Figure 42 below shows the direction of extrusion in the model for reference.



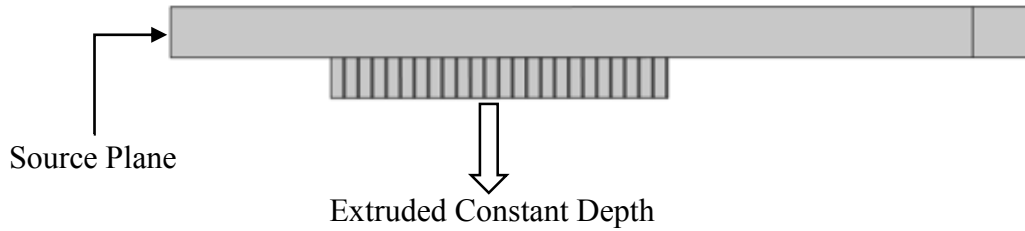


**Figure 42.** Constant depth extrusion liner

The depth varied from 1-3 inches in order to observe multiple behaviors. The transmission loss is evaluated at each frequency while varying the liner depth as shown below in figure 43.

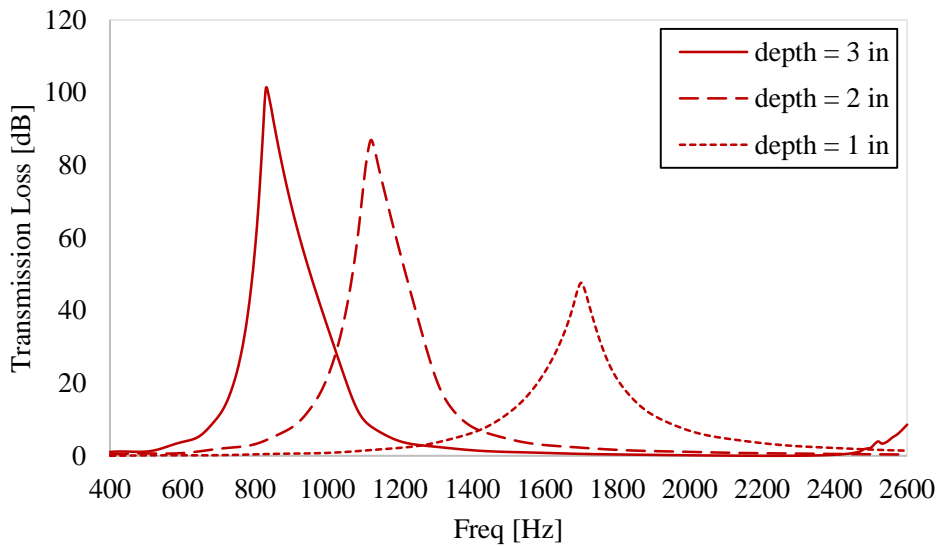


**Figure 43.** Transmission loss plot of constant depth extrusion study

As seen from figure 43 above, the maximum attenuation is reached at the maximum depth of 3 inches. As the depth increases, the peak of the TL plot shifts to lower frequencies. The increase in cavity depth moves the anti-resonance frequency to a lower frequency. Thus, the strong anti-resonance behavior of the reactance becomes apparent for the liner with a deeper cavity. At frequencies away from this anti-resonance, the resistance is unaffected by the depth change. There is at least a 20 dB drop as depth decreases within a 200 Hz range. Between a 2 inch and 3 inch

depth, the TL peak drops about 20 dB over 300 kHz, while the smallest depth peaks 600 kHz higher than the 2 inch depth. Therefore, this overall design shows poor performance broadband.

#### 4.1.2 Single Section Angled Study

Building on the observation above, an angled design is considered. The perceived benefit of angling the liner is that there will be increased sound wave reflection created over a broader frequency range resulting in an overall increased TL. A nonuniform depth can be tailored to regulate the direction in which the pressure waves reflect from the back wall. This effect in general will assist reflection from a wider range of wavelengths over the length of the liner. With a variety of different depths throughout the length of the liner, more resonance frequencies can be targeted. Two angled configurations will be considered as shown below in Figure 44 where the depths at the far end are fixed at 3 inch and 0 inch, respectively. Design optimization studies were performed to determine the best angle for each design and to assess the effect of including a minimum depth at the end of the liner. Note that a two-parameter optimization model could have been developed to optimize a linear profile allowing each end to vary in length; however, the increase in computational time was prohibitive for this study.

The attached table to the right in Figure 44 shows the final depths for each model.

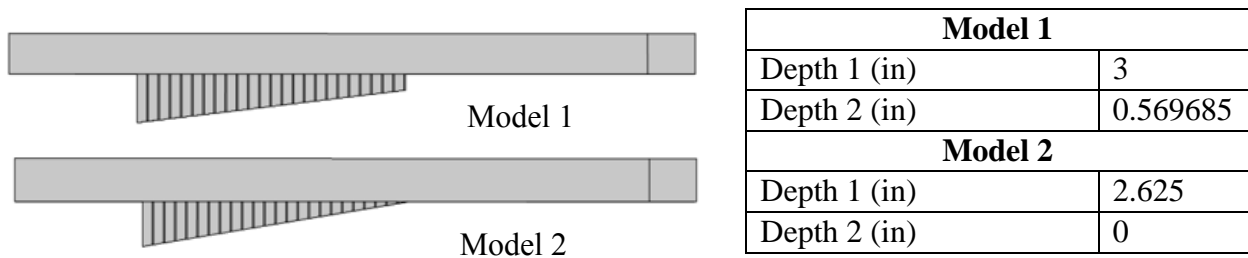


**Figure 44.** Single section angled designs with geometric parameters shown on right

To illustrate the convergence process during optimization, the objective variable histories are shown below in table 6. Starting with an initial guess for the height of the free (left) end, denoted as variable x, the optimization cycle calculates the total TL by correctly summing the TL over all frequencies and then updates the design variable and repeats the calculation until the objective function is maximized to a specified tolerance. For all cases that follow, the convergence history during optimization will not be shown; only the optimal value will be provided.

Table 6. Objective table display iteration through COMSOL for model 1 and 2

<b>Objective Table – Model 1</b>	<b>Objective Table – Model 2</b>
variable x (m)	variable x (m)
0.0508	0.0508
2.54E-04	0.0254
0.025527	0.0762
0.0508	0.0635
0.0128905	0.0508
2.54E-04	0.06985
0.01920875	0.05715
0.00657225	0.066675
0.016049625	0.06985
0.01920875	0.0650875
0.014470063	<b>0.066675</b>
0.0128905	
0.015259844	
<b>0.014470063</b>	

Figure 45 shows the TL over the studied frequency range for the optimized solutions for both angled designs. As seen from the figure, varying the depth of the liner improves the broadband performance significantly as compared to the constant depth extrusion. The reactance part of the acoustic impedance primarily is set by the depth of the liner. Therefore, when the depth varies throughout the length of the liner, the reflections created will cover a wider range of frequencies. Extending the angled concept further leads to a multiple section angled liner design presented next.

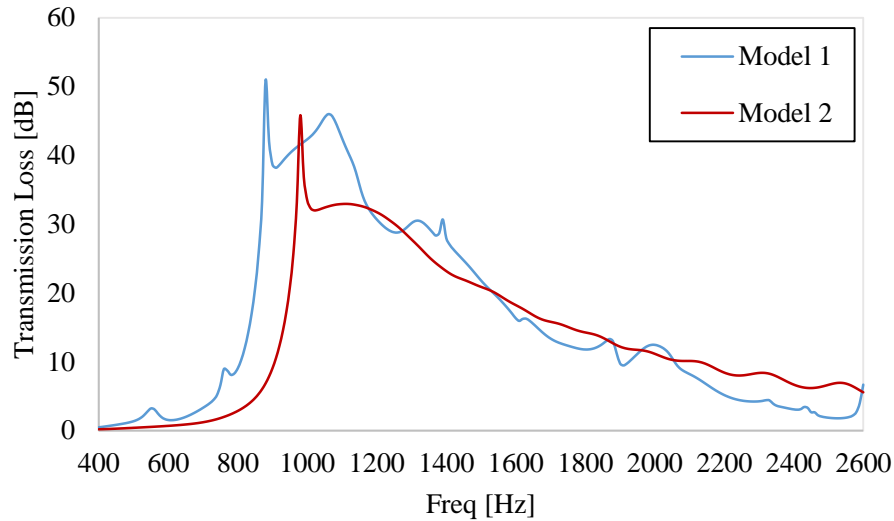


**Figure 45.** Transmission loss comparing models 1 and 2 for single sectioned angle study

#### 4.1.3 Four Section Angled Study

Building on the single section angled study above, a four section angled liner is designed with the goal of simulating a sinusoidal wave shape to further improve noise cancellation. The idea of creating multiple sectioned liners is to be able to mimic a varying depth liner while adding additional loss effects. Figure 46 shows the model using a maximum depth of 3 inches again and minimum of zero which is consistent with the dimensions from the prior study. Note the similarity between this profile and a sine wave. The TL result for the four-stepped design is shown in figure 47. The overall shape proves to capture additional high frequencies while continuing to benefit in the low frequencies. Since the shape of the extrusion causes reflections at multiple points down the length, a wider range of frequencies is captured. This trend of varying depths down the duct leads to the final study of a sine wave shape.

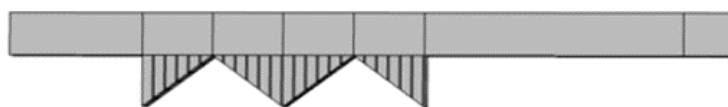


**Figure 46.** Four step design COMSOL model

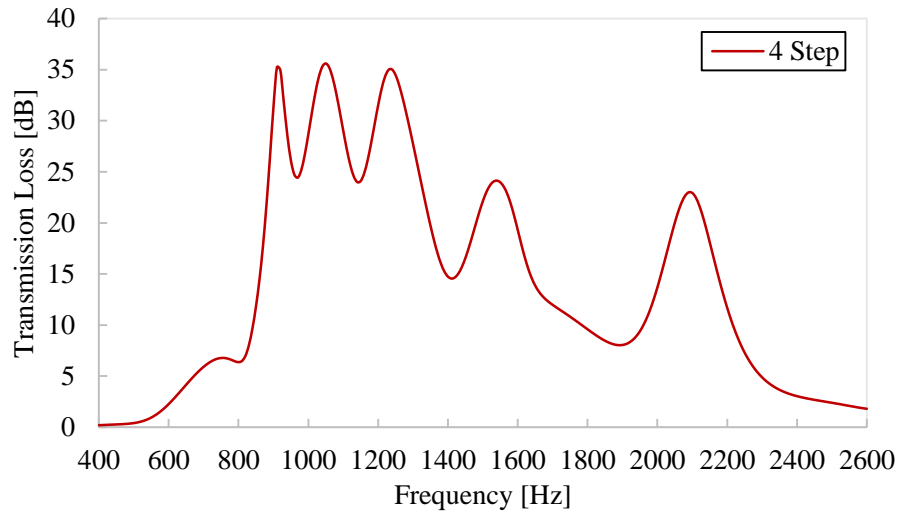


**Figure 47.** Transmission loss for four section angled design

#### 4.1.4 Sine Profile Study

The sine profile design in Figure 48 is analyzed with the goal of achieving greater sound cancellation using the (potential) benefits associated with a curved surface. Using the geometry limits throughout all investigations, the maximum depth will remain at 3 inches while varying the amplitude of the sine function between 0.75 inches and 1.5 inches. Two periods were modeled corresponding to a wavelength of 8.39 inches. An optimization study was performed to demonstrate the ideal amplitude for maximum attenuation over the specified frequency range.



**Figure 48.** Sine model displaying optimization variable amplitude movement

The top design in Figure 48 below displays the results from this analysis. The amplitude for peak performance was determined to be 1.25 inches. For comparison purposes, two additional models were analyzed by fixing the amplitude at 1.25 inches and maximum depth at 3 inches, and doubling and halving wavelengths. The TL plot over the entire frequency range for all three sine profile designs is shown in Figure 50.

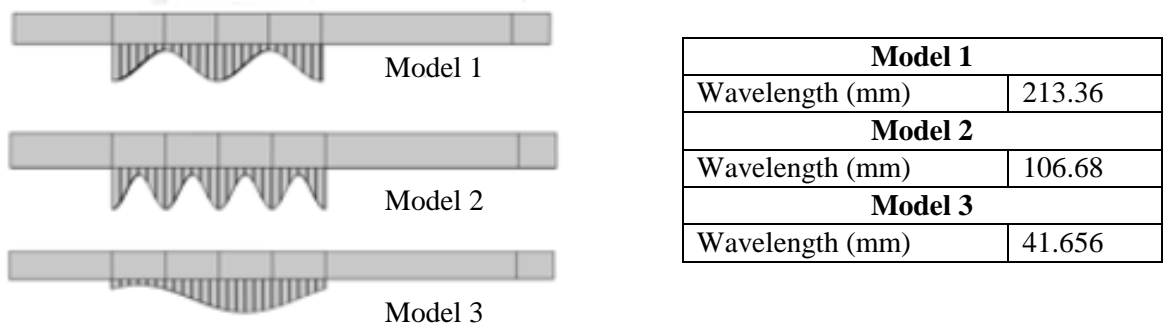


**Figure 49.** Three sine wave models used in wavelength study

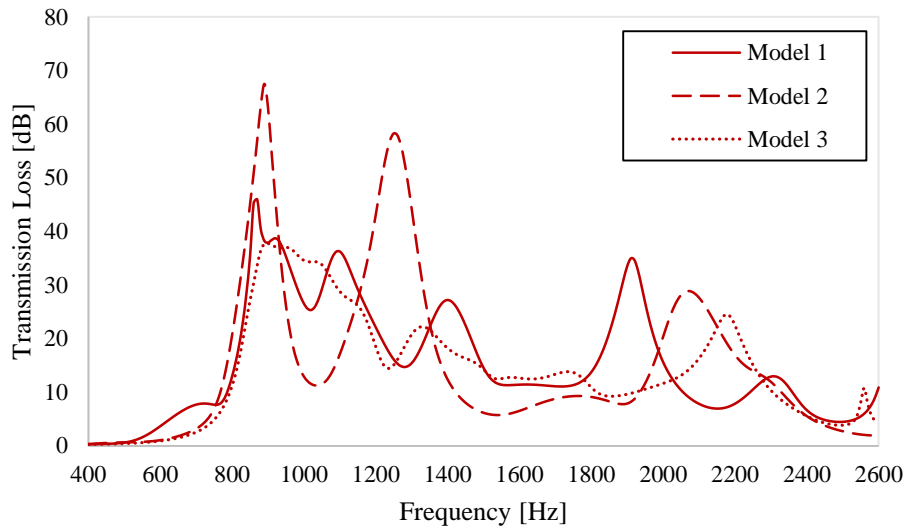


**Figure 50.** Transmission plot showing wavelength study

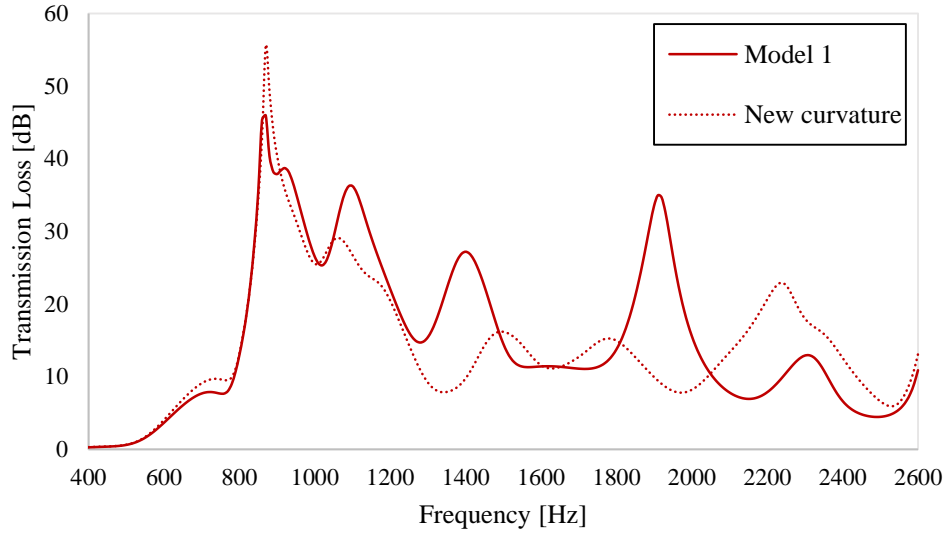
From Figure 50 above, model 1 with a wavelength of 8.39 results in most optimum design, producing broadband performance from approximately 800 Hz to 2300 Hz.

#### 4.1.5 Quadratic Profile Study

Building off of the last result, the final study looks at curvature effects of the original two period sine profile to target improved performance in the higher frequencies in the range of 2000-2400 Hz. This idea is to build a model with a ‘rounder’ design, potentially introducing increased reflection, and assess any upper-frequency performance benefits. A quadratic-shaped extrusion was selected as shown in Figure 51 and compared against the optimized sine profile.

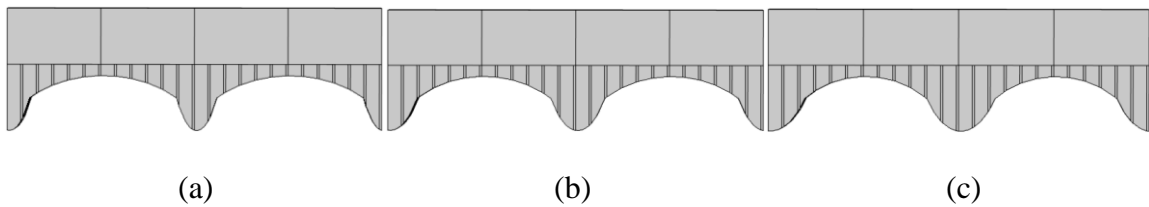


**Figure 51.** Model 1 geometry (left) and new curvature geometry (right)



**Figure 52.** Transmission loss of model 1 vs. new curvature model

Observing this graph, the quadratic shape showed to have more broadband benefit. Therefore, an optimization study is completed varying the distance between the center half-wavelength while keeping an overall quadratic connection shape. The figures below a-g demonstrate this variation from one extreme to the other.



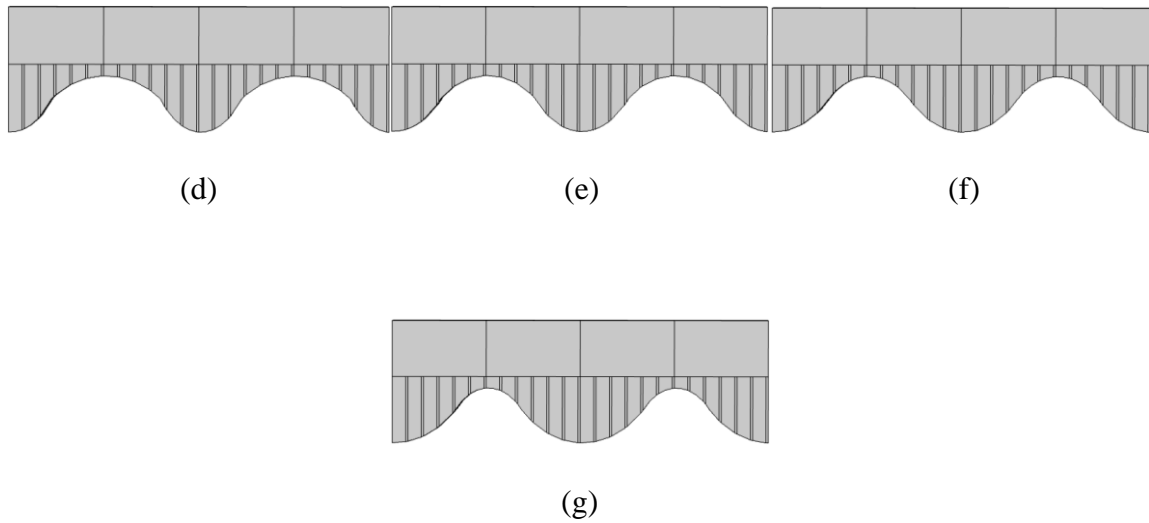


**Figure 53.** Models in the curvature study

The transmission loss of all of these figures is shown below.

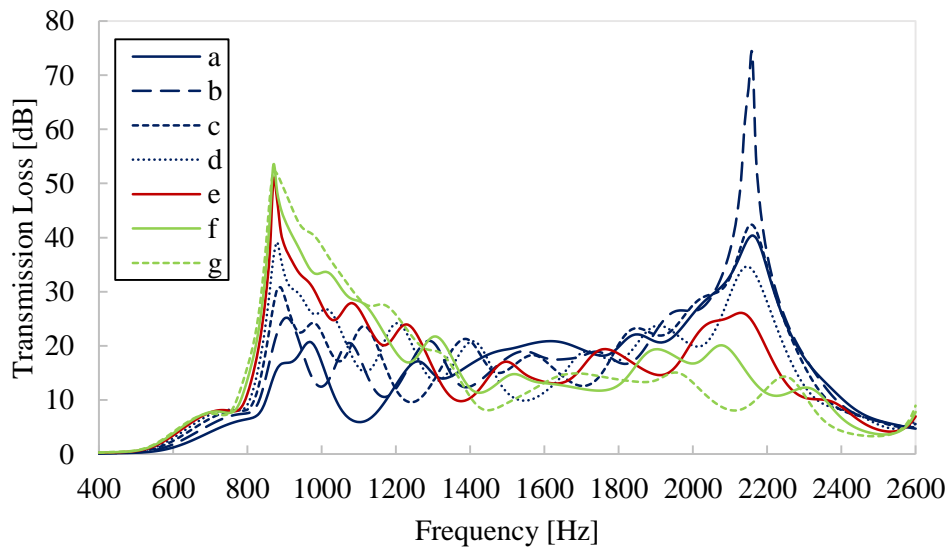


**Figure 54.** Transmission loss of quadratic optimization study

As shown, the figure ‘b’ proved to give the most transmission loss broadband while additionally having at least 68% of the frequencies resulting in at least 10 dB. This design is not only more successful in broadband performance, but it has a smaller overall volume and therefore is lighter and cheaper. The overall attenuation is calculated by the summation of each TL value at each frequency beginning at 400 Hz up to 2600 Hz, increments of 10 Hz. The table below shows the



percentage of frequencies that give at least 10 dB. The more variation within each design, the more efficient the models are for broadband performance.

Table 7. Design chart and corresponding amount of TL over a certain frequency range

Design	% > 10 dB
Constant Depth Extrusion	19.2
Single Section Angled	56
Four Section Angled	54.6
Sine Profile	63.2
<b>Quadratic Profile 'b'</b>	<b>68.2</b>

#### 4.1.6 Conclusions of Shape Study

The progression from a constant depth liner design to curved profile shapes was influenced by the idea of achieving greater wave reflection and hence potential cancellation. Different cavity depths give different resonances and hence an increased broadband effect [41]. Table 7 summarizes the results for the five liner designs in terms of broadband performance by quantifying the percentage of frequency range that exhibited TL improvement greater than 10 dB. The best design was the quadratic profile design with at least 10 dB of attenuation over 68% of the frequencies. The quadratic shape gives enough variation in depth down the length while in addition creating a reflective surface to lower the pressure transmission through the exit. If the requirement is to target certain frequencies that achieve at least 20-30 dB, the best design would be the single angled section. The single angled section does not target as many frequencies broadband; however gives enough depth and effective shape to capture a significant amount of attenuation for certain

frequencies. This design is also less volume than a constant depth extrusion liner and hence is cheaper and more efficient to employ.

#### 4.2 Porous Material Implementation

Observing broadband performance, in general it is difficult to improve performance in the frequency ranges of 400-1000 Hz. For this reason, the implementation of a porous material can be beneficial. A metamaterial is an engineered material that contains properties not found in nature. One of the basic designs consists of a porous material, microperforated plate, and an embedded high density mass. This system will behave overall similar to a spring-mass damper system. The metamaterials being used are melamine and polyimide including masses of aluminum and steel. Table 8 below shows the material properties used.

Table 8. Porous Material and embedded mass properties

<b>Material</b>	<b>Density [kg/m<sup>3</sup>]</b>	<b>Poisson's ratio</b>	<b>Young's Modulus [kPa]</b>	<b>Biot-Willis Coefficient</b>	<b>Porosity</b>	<b>Permeability</b>	<b>Tortuosity</b>	<b>Flow Resistivity (Pa·s/m<sup>2</sup>)</b>
Melamine	9.85	0.4	400+50i	0.99	0.99	1.5e-9	1.0059	10,000
Polyimide	9.6	0.45	60+20i	0.45	0.45	0.2e-9	3.25	29,000
Aluminum	2700	0.33	70e6					
Steel	7850	0.28	205e6					

##### 4.2.1 Melamine Foam

Melamine formaldehyde (MF) has created much attraction because of its physical properties. With its lightweight, low flame, high absorption, and high thermal stability qualities, it is very good for practical acoustic use. A figure of melamine is shown below in figure 55.



**Figure 55.** Melamine foam

Melamine has a flow resistivity of  $10 \text{ kPa}\cdot\text{s}/\text{m}^2$ ; which is a relatively low value. In general, any porous material that has similar properties of melamine will have difficulty in the interaction with wet fluids. The idea of perhaps placing this porous material in a different location within the engine looks very promising for future studies.

#### 4.2.2 Polyimide Foam

Polyimide is a polymer of imide monomers. It has a number of attractive attributes as well. It is desirable in sound transmission applications due to its stringent flammability requirements. In addition, it is resistant to wear, radiation, and many chemicals. It has a higher flow resistivity of  $30 \text{ kPa}\cdot\text{s}/\text{m}^2$ ; and higher density than melamine, therefore it is possible to explore different properties effects on absorption. A figure of polyimide is shown below.



**Figure 56.** Polyimide foam

### 4.2.3 Sensitivity and Optimization Study on Porous Material Properties

As mentioned above, a porous material can be implemented in two different ways in COMSOL: through a poroacoustics model in the pressure acoustics physics allowing the input of flow resistivity; or through the poroelastic waves physics. The latter includes the input of seven macroscopic parameters; all of which can be manipulated. The acoustic parameters include the porosity, Biot-Willis coefficient, and permeability. Three structural parameters include the density, Young's modulus, and Poisson's ratio. Finally, the only geometric parameter includes the tortuosity. A parameter sweep as well as an optimized design study is performed on each property while holding the others constant. Each optimized test requires an initial guess based off of the sweep, as well as a range and an optimality tolerance. This step is crucial in the design process in order to have the opportunity to create a material with the same sort of characteristics that have the same attenuation effects. In order to optimize, the same procedure is taken just as the optimized shape study was performed

The control model used for this examination is the constant depth model filled entire with melamine foam embedded within each chamber.

#### Sensitivity and Optimization of a Porous material to Flow Resistivity

Looking first at the poroacoustics model in pressure acoustics, the flow resistivity value effects are observed first.

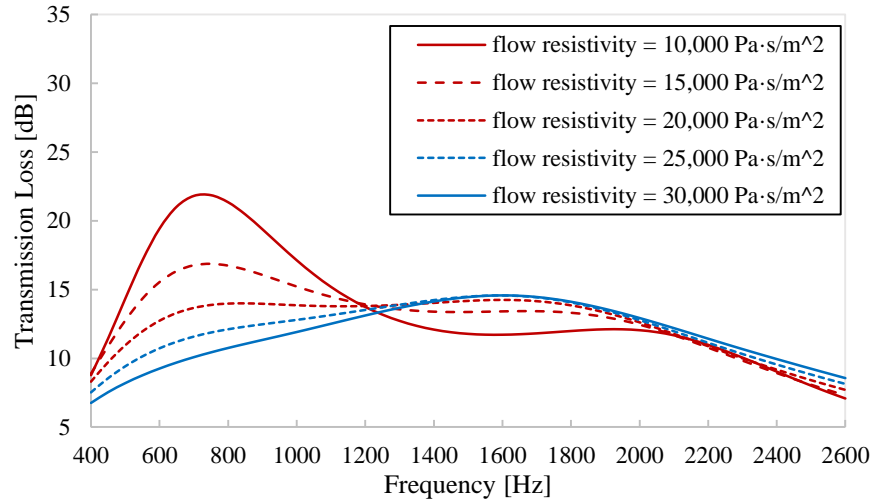


**Figure 57.** Transmission loss of flow resistivity of melamine sweep

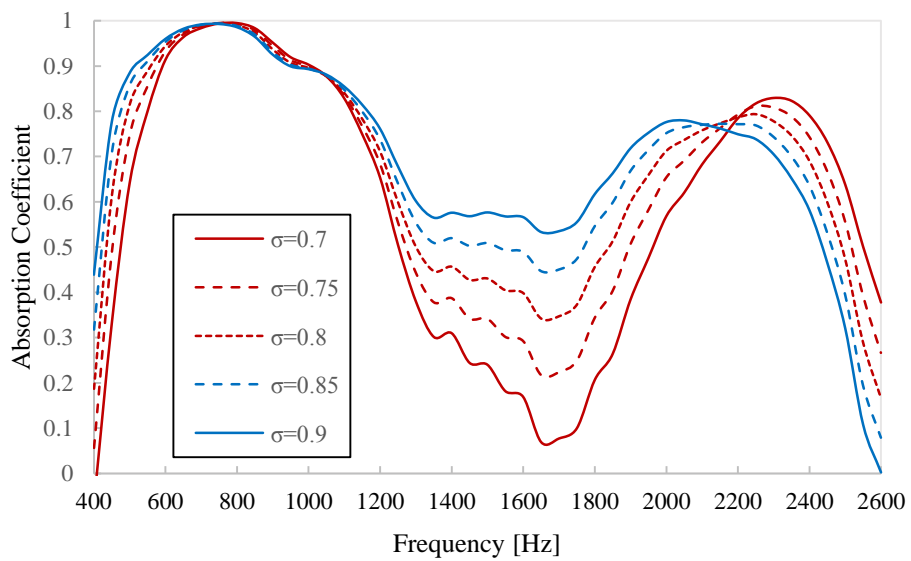
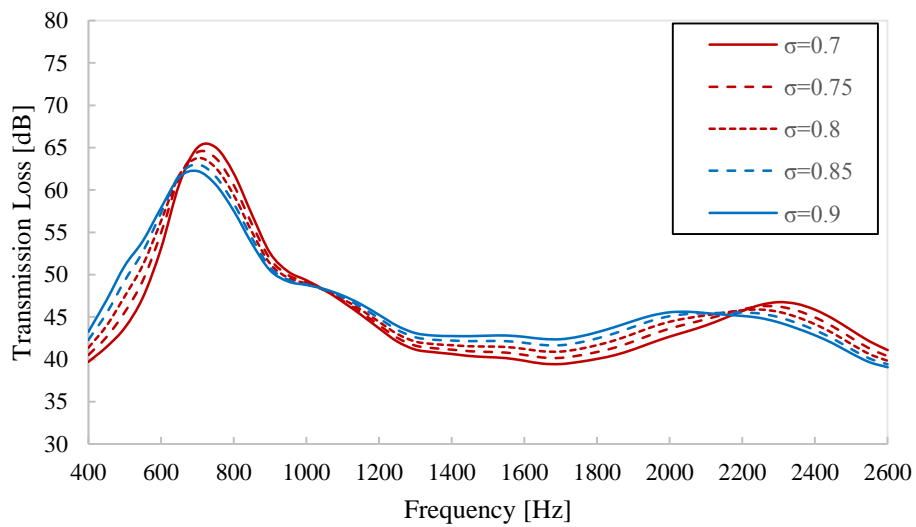
The optimized study results in a value of 10 kPa·s/m<sup>2</sup> giving the maximum transmission loss.

Table 9. Optimized flow resistivity values to give maximum TL

<b>Flow Resistivity Pa•s/m2</b>
13000
13150
12850
12700
12400
12100
11500
10900
10000
10450
10225
10112.5
10056.25
10028.125
10014.0625
10007.03125
10003.51563
<b>10000</b>

## Sensitivity and Optimization of a Porous Material to Porosity

The porosity is defined as the amount of void volume as compared to the total volume. Hence this value will vary from 0, where there only is fluid material, to 1, where the entire volume is a solid. The higher porosity, the easier interaction between the solid and fluid; which therefore physically would lead to more sound attenuation. The transmission loss plot as well as absorption are shown below in figure 58, varying the porosity from 70% to 90%.



**Figure 58.** Sensitivity study to porosity for transmission loss (upper) and absorption coefficient (lower)

Between the frequency ranges of 400-600 Hz and 1100-2100 Hz, the highest porosity shows to be most absorptive. In the range 2100-2600 Hz, the lowest porosity proves to give approximately 5 dB more attenuation. The absorption coefficient shows to be more sensitive to changes in the porosity.

Table 10. Optimized porosity values for maximum TL

Porosity Value
0.9
0.8
0.99
0.945
0.9675
0.97875
0.984375
0.9871875
0.98859375
0.989296875
<b>0.99</b>

The final optimized porosity is returned as 99% porous, giving the maximum transmission loss.

Sensitivity and Optimization of a Porous Material to Young’s Modulus

The Young’s modulus is a measure of the stiffness of an elastic isotropic material. The transmission loss and absorption coefficient plot are shown below in figure 59. The porous foam is not very sensitive to changes in the Young’s modulus. At high frequencies from 2000-2400 Hz it is shown that the natural frequency of the foam increases as the Young’s modulus increases.

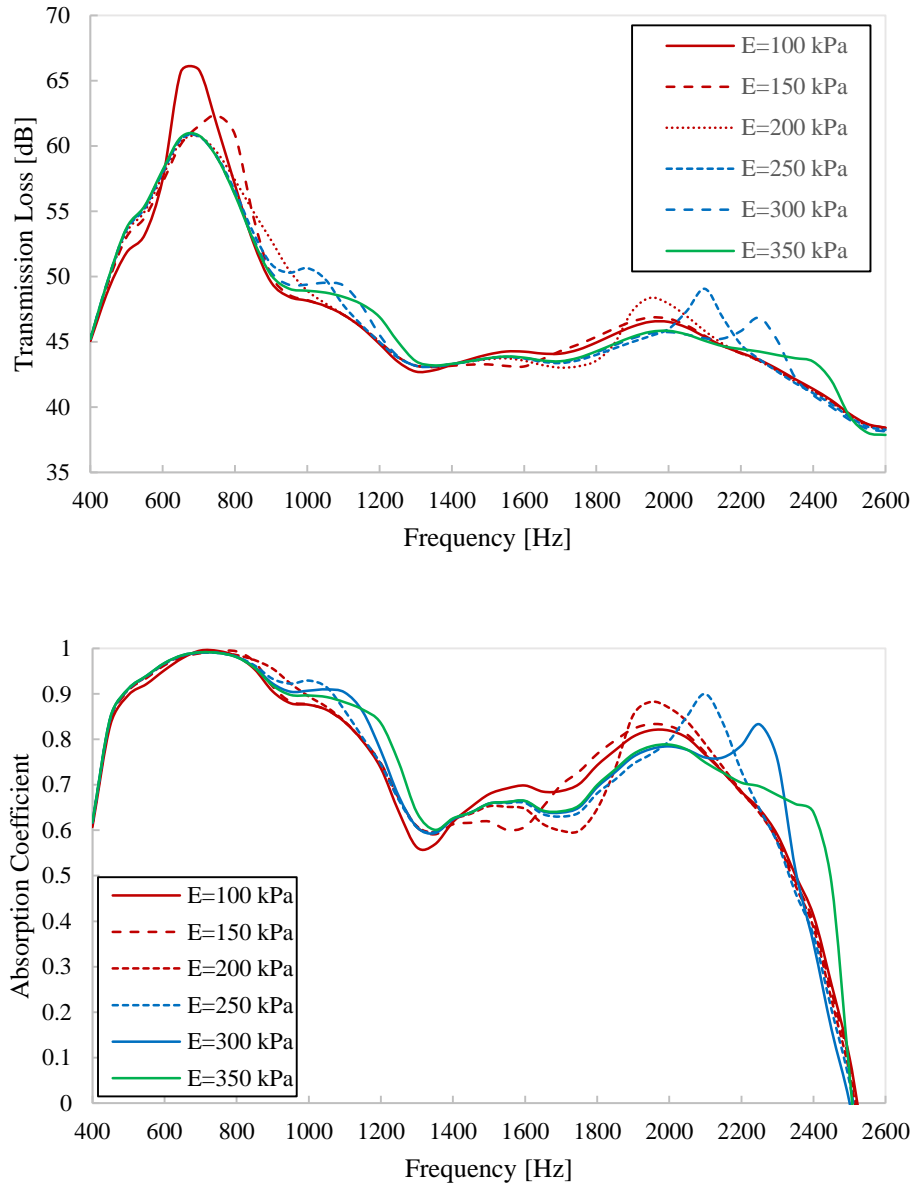


**Figure 59.** Sensitivity study to Young’s modulus for transmission loss (upper) and absorption coefficient (lower)

Sensitivity and Optimization of a Porous Material to Tortuosity

The tortuosity factor  $\tau$ , or the structural form factor, is a dimensionless number that depends on the microscopic geometry and distribution of the pores within the porous material. In general, the more complex the propagation through the porous material, the higher the absorption will be.



This number is independent of the solid and fluid properties and is normally greater than 1. The transmission plot and absorption coefficient plot for the permeability sweep are shown below.

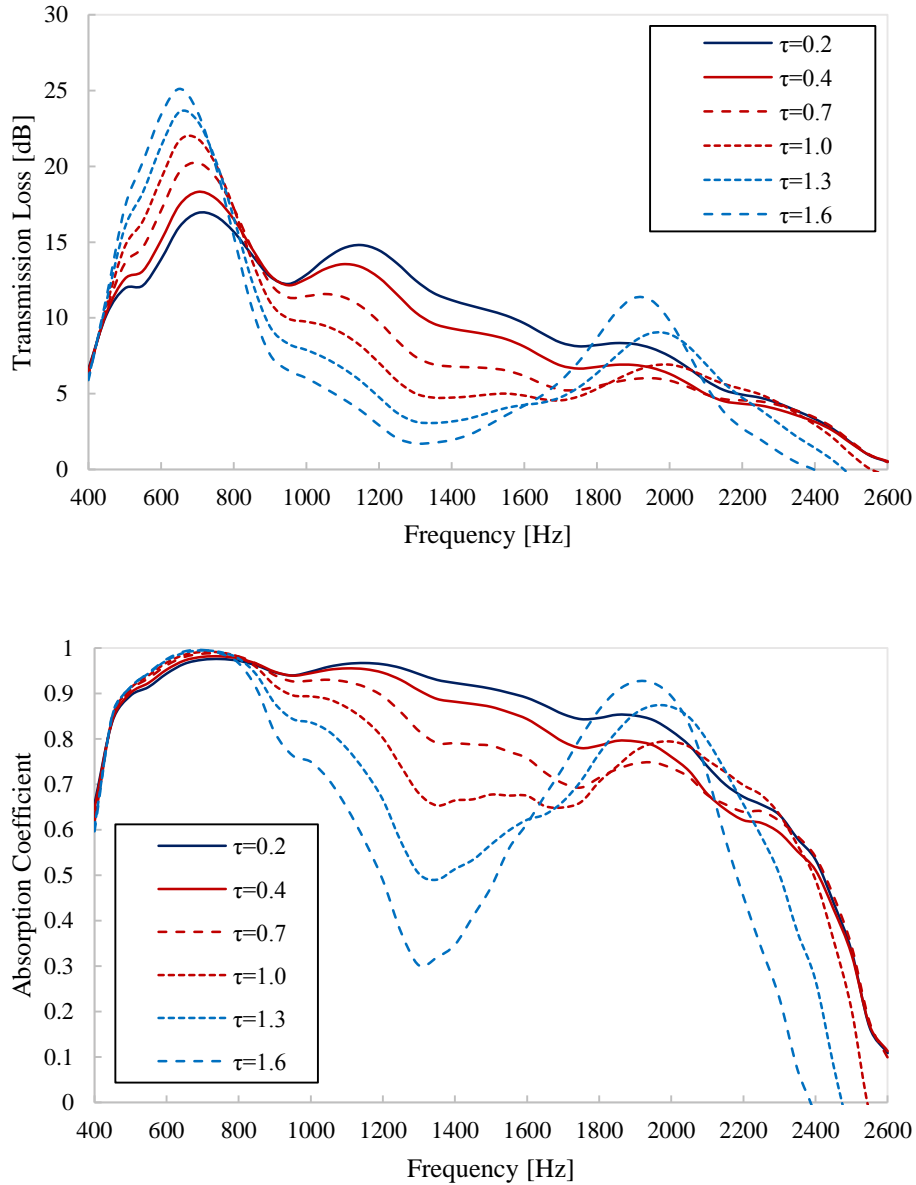


**Figure 60.** Sensitivity study to tortuosity for transmission loss (upper) and absorption coefficient (lower)

In the range of 400-800 Hz, the absorption coefficient appears to be maximized over all values of tortuosity, however the attenuation produced is much higher the higher the  $\tau$  value. Within the ranges of 800-1600 Hz, the lowest value of  $\tau=0.2$  demonstrates to attenuate about 8-10 dB more

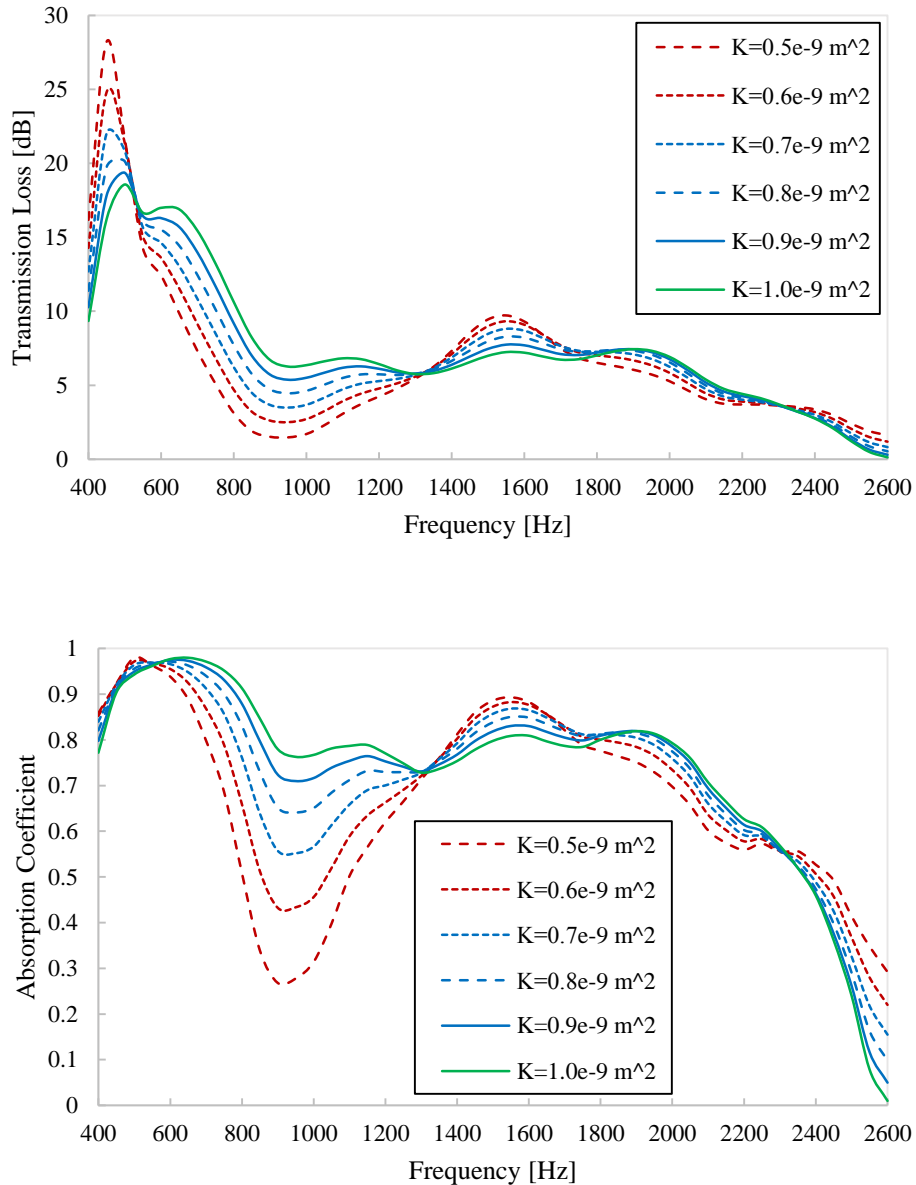
than the highest tortuosity. The optimized objective table is shown below, giving the final tortuosity value to be 0.2 for maximum attenuation.

Table 11. Optimized tortuosity values and corresponding TL

<b>Tortuosity</b>
0.4
0.7
0.2
0.3
0.25
0.225
0.2125
0.20625
0.203125
0.201563
0.200781
0.200391
<b>0.2</b>

#### Sensitivity and Optimization of a Porous Material to Permeability

Permeability is the capacity of the porous foam to allow fluids (air) to pass through it. The porosity will directly affect the permeability in that the porosity is the physical definition of space vs. structure, while the permeability explains the behavior of their interaction. The transmission loss plot as well as absorption plot for the permeability sweep are shown below.



**Figure 61.** Sensitivity study to permeability for transmission loss (upper) and absorption coefficient (lower)

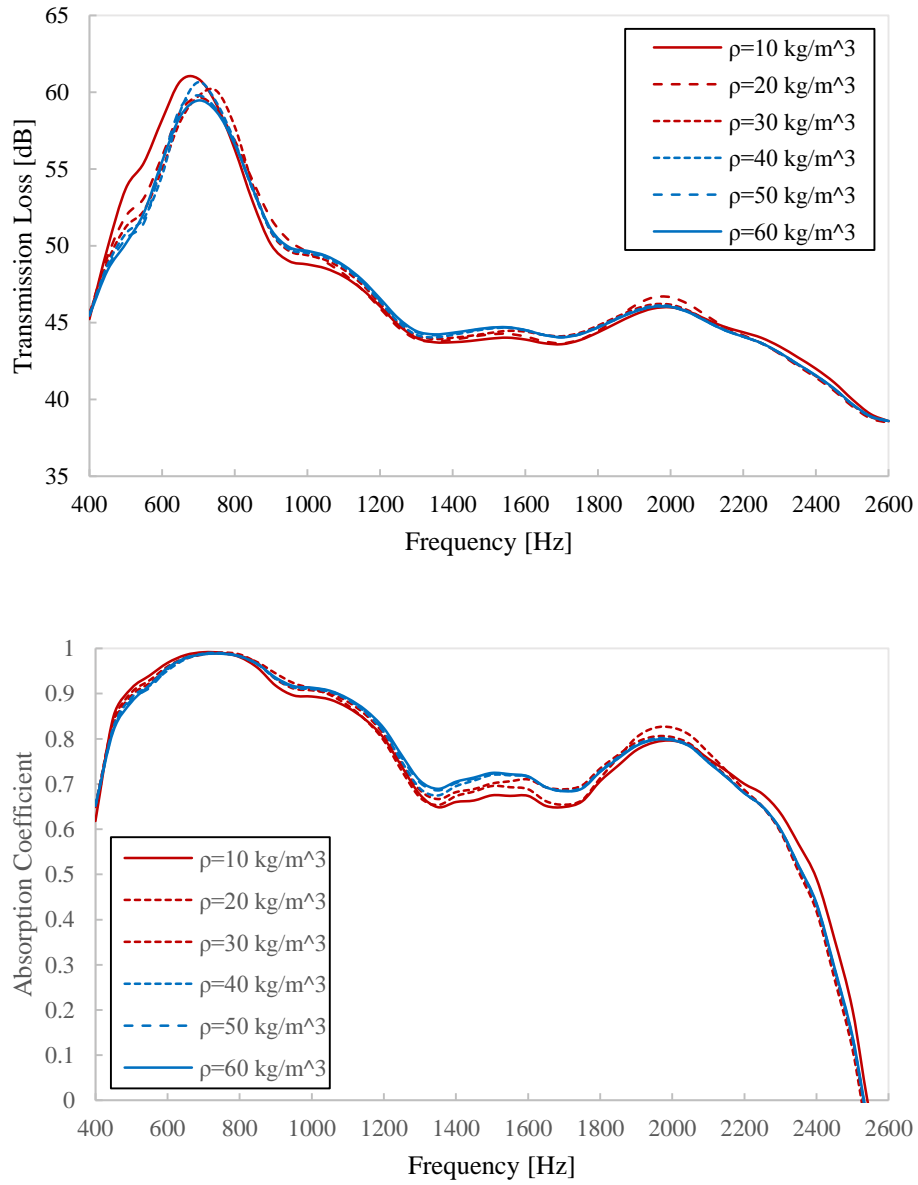
Within the frequency range of 600-1200 Hz, the higher the permeability, the greater amount of fluid is allowed to pass through it; hence more attenuation. From 1400-2600 Hz, there seems to be a **tradeoff** between the higher the permeability value and the highest absorption. The objective table below demonstrates the optimized value for permeability which was computed to be 1e-9.

Table 12. Optimized permeability values and corresponding TL

<b>Permeability Value [m<sup>2</sup>]</b>
6.0000E-10
1.0000E-09
8.0000E-10
9.0000E-10
9.5000E-10
9.7500E-10
9.8750E-10
9.9375E-10
9.9688E-10
9.9844E-10
9.9922E-10
9.9961E-10
<b>1.0000E-09</b>

Sensitivity and Optimization of a Porous Material to Density

The density is defined as the mass per unit volume. The transmission and absorption show to behave very similarly over all density values. This is a very good trait to have in that having a lower mass will benefit the overall efficiency of the design without affecting its ability to attenuate noise. With a lower overall mass, the weight of the entire system will decrease and the ability to add additional materials to the design will be easier. For example, adding aluminum masses to simulate the metamaterial design will up the weight of the system dramatically.



**Figure 62.** Sensitivity study to density for transmission loss (upper) and absorption coefficient (lower)

Table 13. Optimized study showing the density value and corresponding TL

Density [kg/m <sup>3</sup> ]
15
14.7
14.4
14.1
13.5
12.9
11.7
10.5
11.7
9.85
10.175
10.0125
9.93125
9.890625
9.85508125
9.852539063
9.851269531
9.850634766
9.850317383
<b>9.85</b>

The optimized density is 9.85 kg m<sup>-3</sup> corresponding to the maximized TL. In general, porous materials with higher porosity have a smoother absorption trend. As the porosity decreases to a fluid material, the peaks of the absorption are more pronounced. As the dimensions of the pores are smaller, losses occurs due to viscous friction and thermal conduction.

Sensitivity and Optimization of a Porous Material to Biot-Willis Coefficient

The Biot-Willis coefficient is a dimensionless number that relates the bulk modulus (or the compressibility) of the porous matrix to a block of solid material [42]. It is defined as

$$\alpha_B = 1 - \frac{K_d}{K_s} \tag{Eq. (44)}$$

Hence, a value closest to 1 signifies nearly a soft porous material, and a rigid porous material will have a Biot-Willis coefficient approximately equal to the porosity. Figure 63 below shows that varying this value does not affect the transmission or absorption across all frequencies.

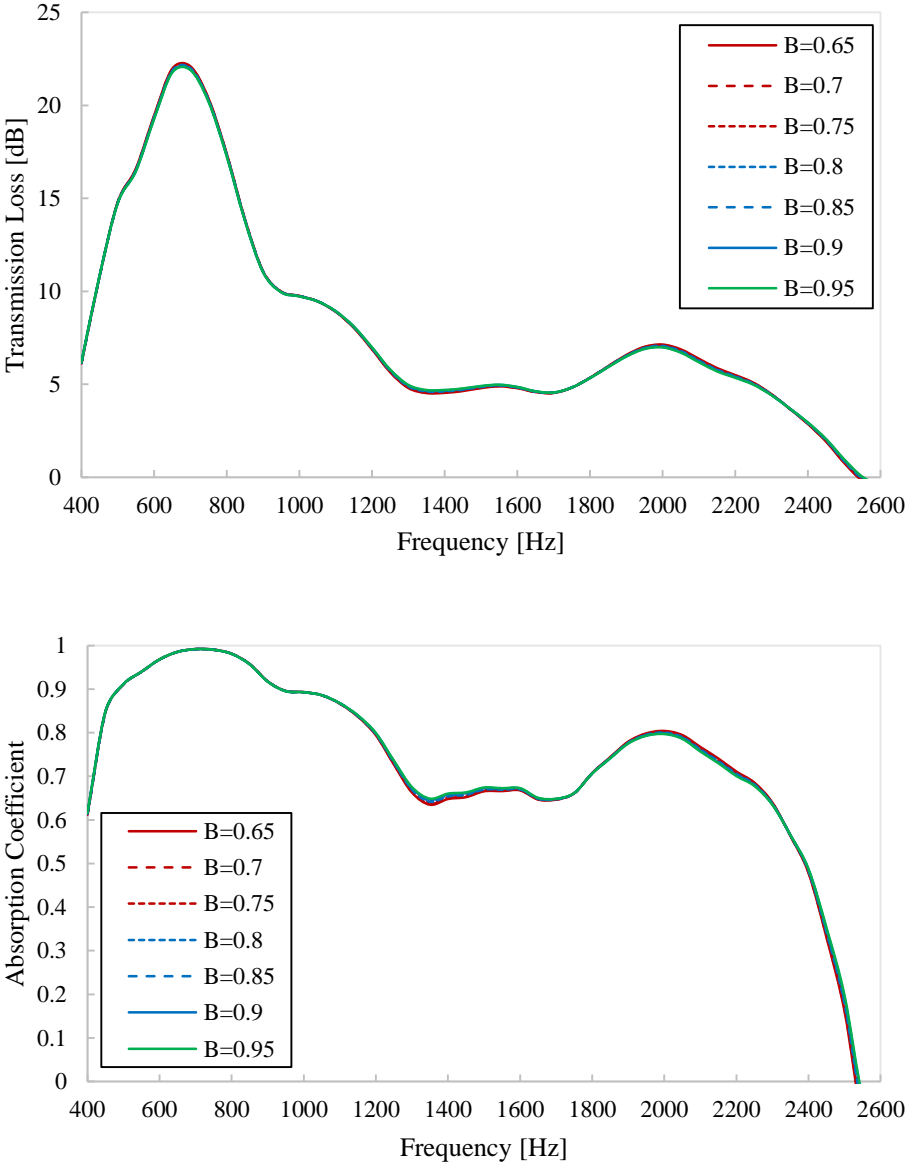


**Figure 63.** Sensitivity study to Biot-Willis coefficient for transmission loss (upper) and absorption coefficient (lower)

## Sensitivity and Optimization of a Porous Material to Poisson's Ratio

Poisson's ratio defines the transverse to axial strain. Figure 64 below shows the transmission loss and absorption coefficient plots. This results are unaffected by the changes in Poisson's ratio. While this may seem like an unsatisfying result, it is actually beneficial in that multiple materials can be used to produce the same attenuating effects even if they have different Poisson ratios.

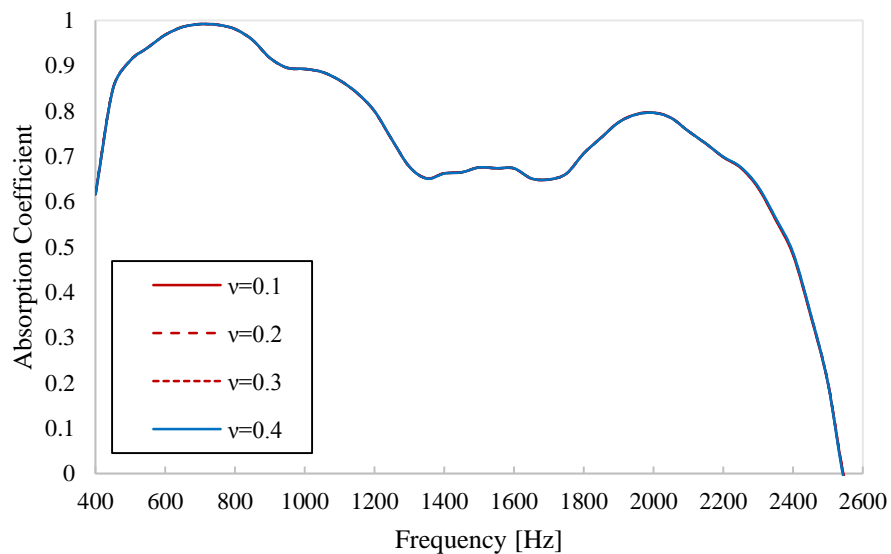
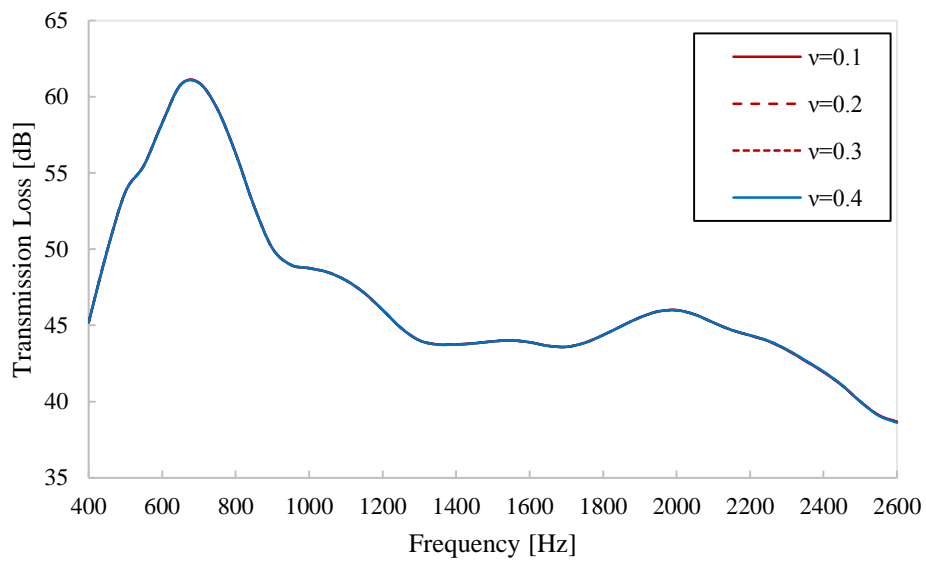




**Figure 64.** Sensitivity study to Poisson’s ratio for transmission loss (upper) and absorption coefficient (lower)

### 4.3 Microperforated Plate (MPP)

This section briefly examines the application of a microperforated plate as a form of noise suppression. The pores distort the flow of air in a thin region as the sound passes through the panel. Viscous dissipation increases as the velocity through the pores reaches a maximum. Microperforated plates are reclaimable, environmentally noncombustible, and offer an increase in lower frequency sound absorption. They can be constructed from a range of materials including plastics, thin metals, or fiberglass. Investigations will be shown using an MPP backed by an air cavity; but further tests will show a metamaterial addition as a backing as well.

The acoustic impedance at the front surface of an MPP backed by an air cavity is given as [43]

$$Z_{1s} = R_{1p} + j[X_{1p} - \cot(kD_1)] \quad (45)$$

where  $R_{1p}$  and  $X_{1p}$  are the resistance and reactance of a single MPP, and  $\cot(kD_1)$  is the reactance of the backing air cavity where  $D_1$  is the distance of air behind the cavity and  $k$  is the acoustic wave number in the fluid the wave is traveling through.

### 4.4 Acoustic Metamaterial

#### 4.4.1 Embedded Masses

The inclusion of aluminum and steel spheres inside a melamine-filled constant depth liner will be examined as to begin simulating a full metamaterial design. The passive elements in this design will utilize high-frequency absorption by dissipating acoustic energy, while the embedded masses will create dynamic vibration absorption. The first result consists of embedding one

aluminum sphere within each liner cell, placed right below the facesheet at a depth of 0.5". The radius of each sphere varies from 0.01" to 0.22" to not pass the maximum cell side length of 0.6" total. The transmission loss plot is shown below in figure 66, as well as absorption coefficient plot in figure 67.

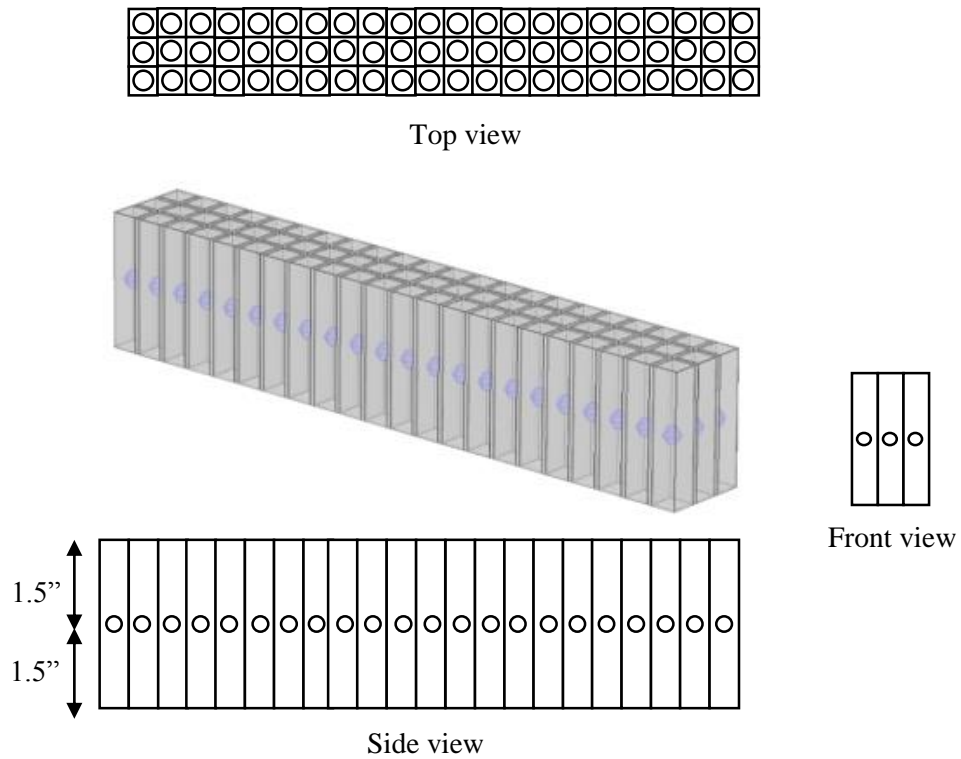


**Figure 65.** Liner domain and schematic figures from three views. Spheres highlighted in purple (one per cell)

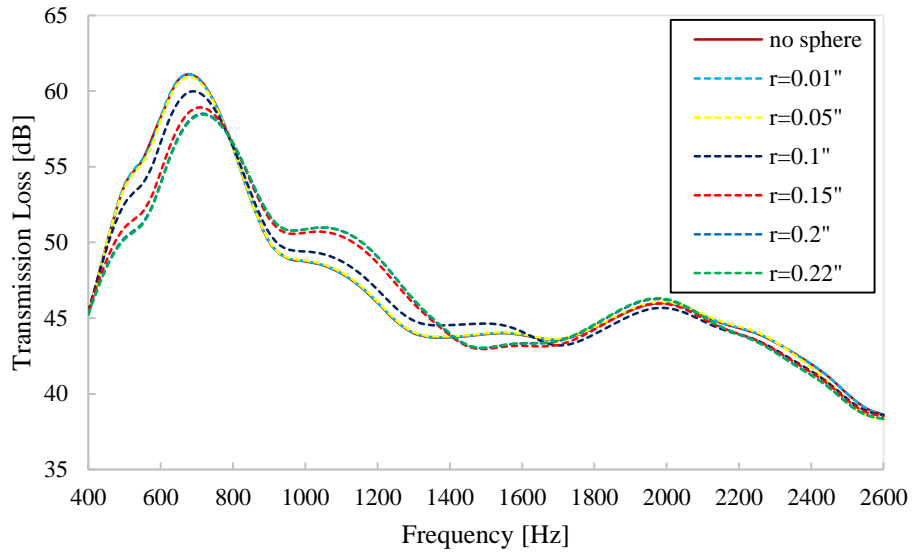


**Figure 66.** Transmission loss of 1 aluminum sphere embedded in melamine foam model

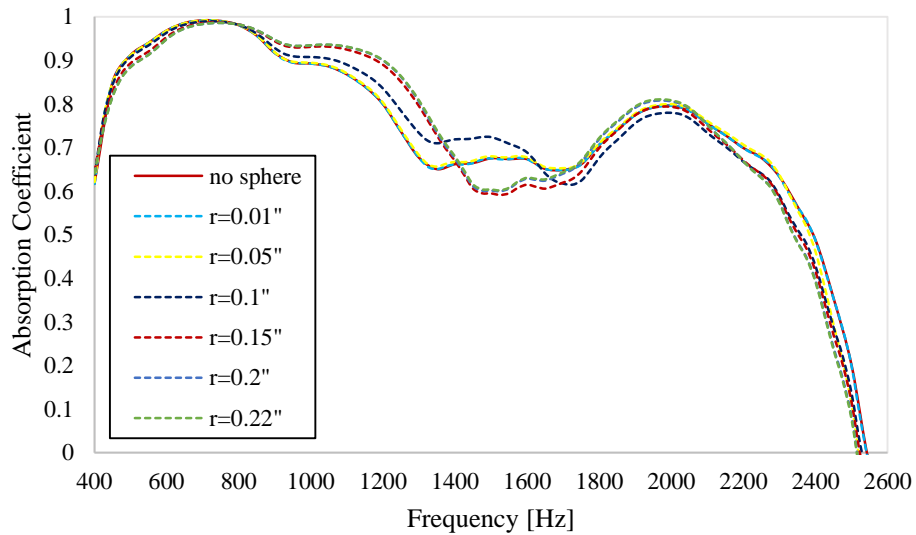


**Figure 67.** Absorption coefficient of 1 aluminum sphere embedded in melamine foam model

Adding one sphere does not show significant effects, therefore more spheres will be added. The interaction between the spheres will be an important factor in terms of creating a larger impedance mismatch between the masses. The transmission plot below shows two spheres embedded within each cell.

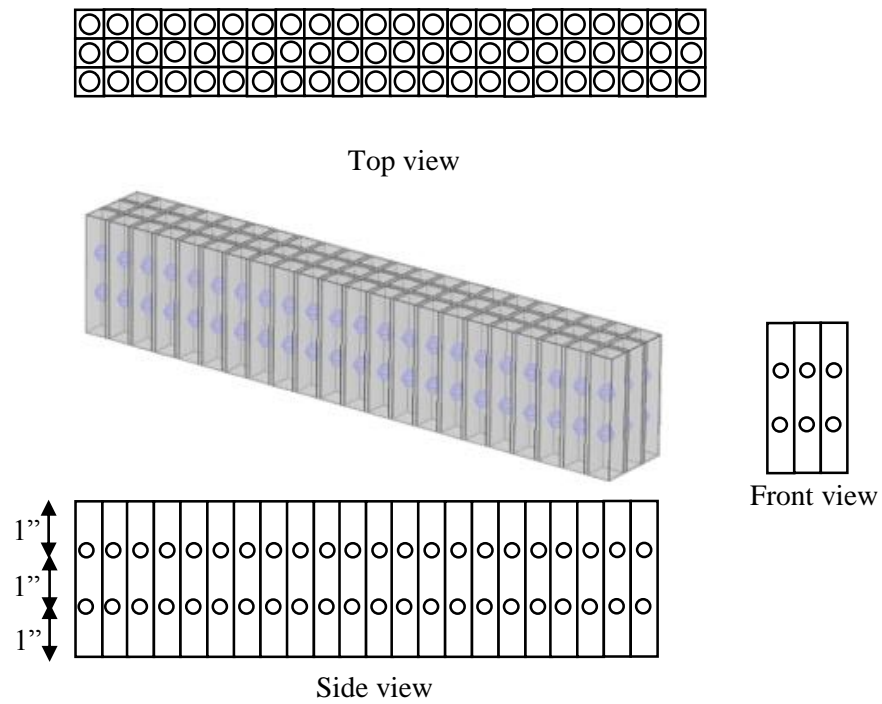


**Figure 68.** Liner domain and schematic figures from three views. Spheres highlighted in purple (two per cell)

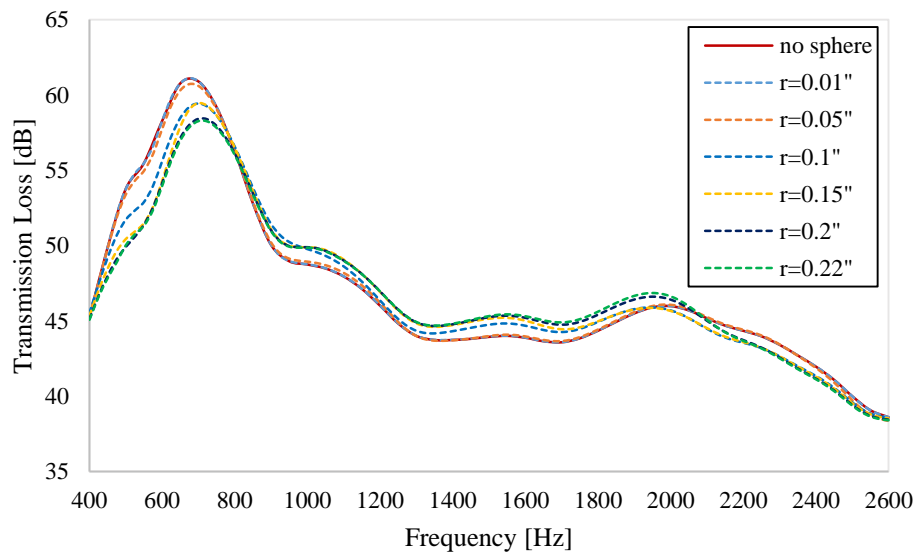


**Figure 69.** Transmission loss for 2 aluminum spheres embedded in melamine foam model

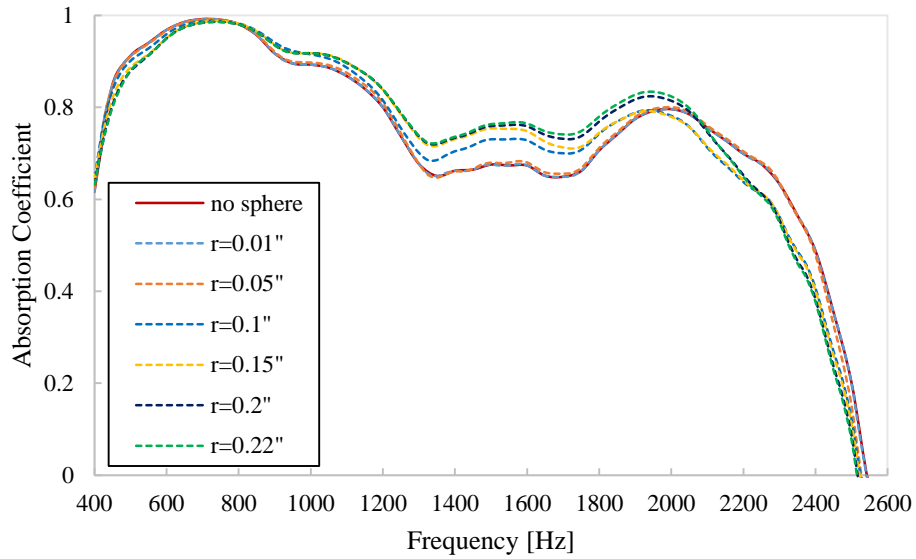


**Figure 70.** Absorption coefficient for 2 aluminum spheres embedded in melamine foam model. For this configuration between 1600-2000 Hz there shows to be significant effects from the embedded spheres. The interaction between the spheres assists dissipating the energy of the waves through this frequency range since the higher frequencies are able to see more of the interaction within the spheres. The increase in absorption at higher frequencies is due to diffraction effects between the porous foam and the spheres.

Moving on to three spheres per liner cell a schematic diagram is shown in figure 71 and the corresponding transmission plot and absorption coefficient are shown below in figures 72 and 73.

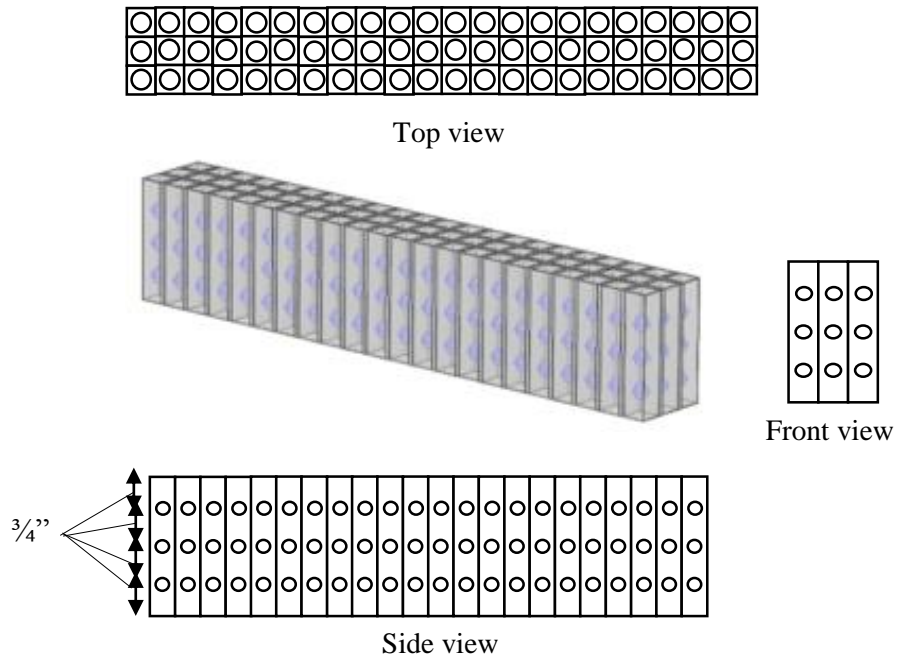


**Figure 71.** Liner domain with spheres highlighted in purple (3 per cell)

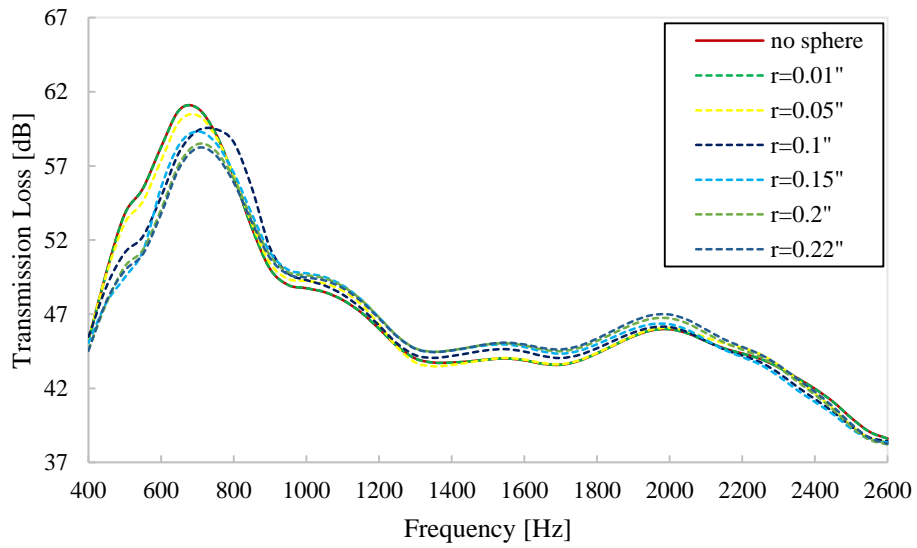


**Figure 72.** Transmission loss for 3 aluminum spheres embedded in melamine foam model

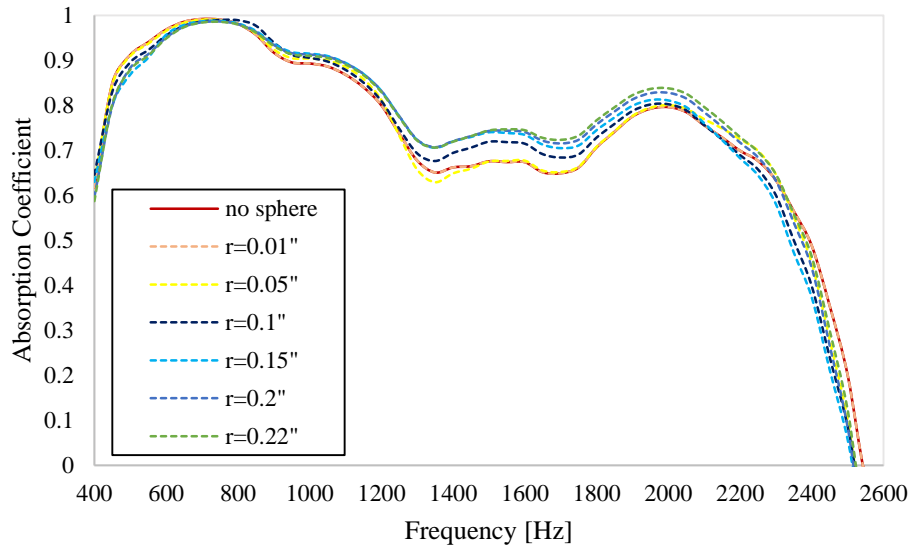


**Figure 73.** Absorption coefficient for 3 aluminum spheres embedded in melamine foam model. Again, within the frequency range of 1200-2000 Hz, the interaction between the spheres proves to create 2-5 dB more of attenuation than just the melamine embedded. The additional masses create more of an effect for the overall spring-mass damper system and hence creates more of a dissipating force from the spheres.

The addition of one final sphere is shown in figure 74 below, followed by the transmission loss and absorption coefficient plot in figures 75 and 76.

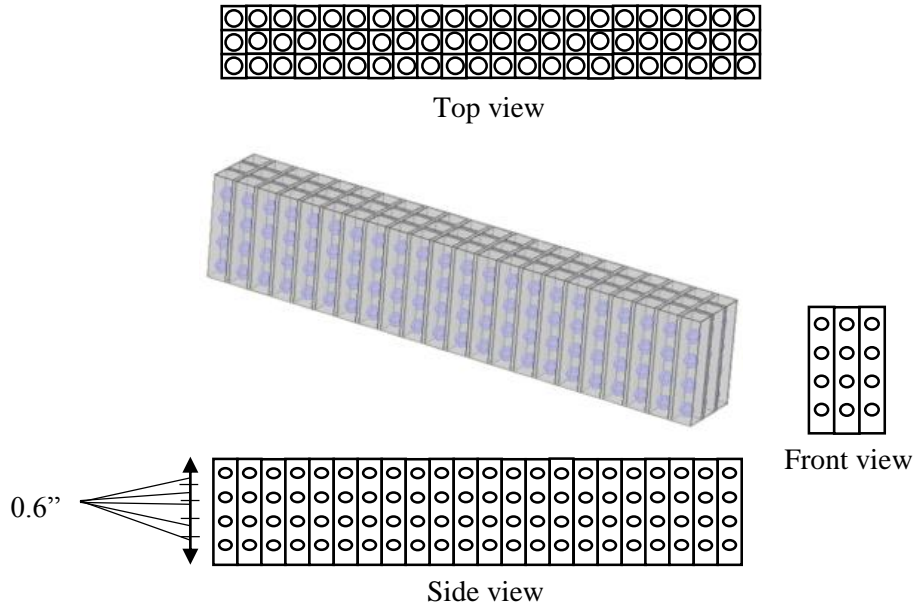


**Figure 74.** Liner domain with spheres highlighted in purple (4 per cell)

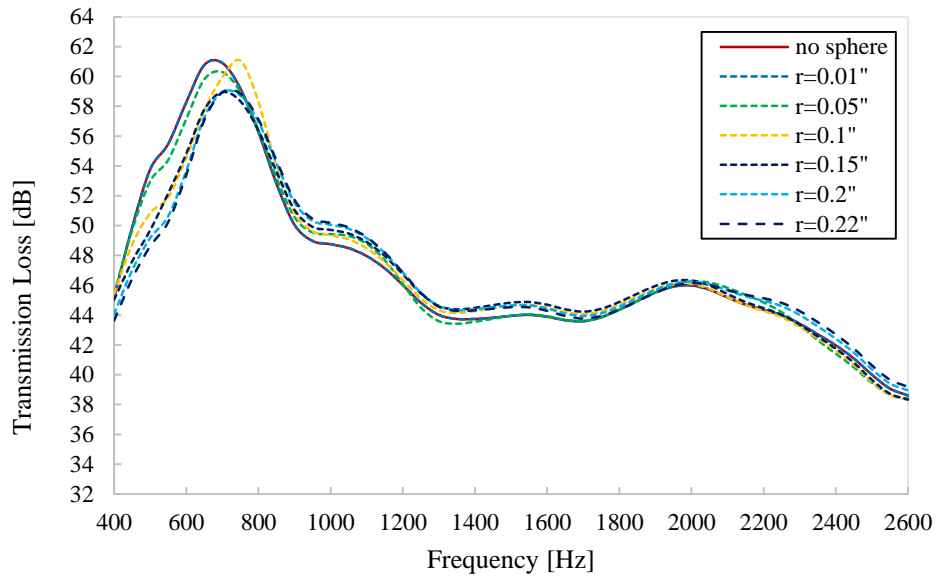


**Figure 75.** Transmission loss for 4 aluminum spheres embedded in melamine foam model



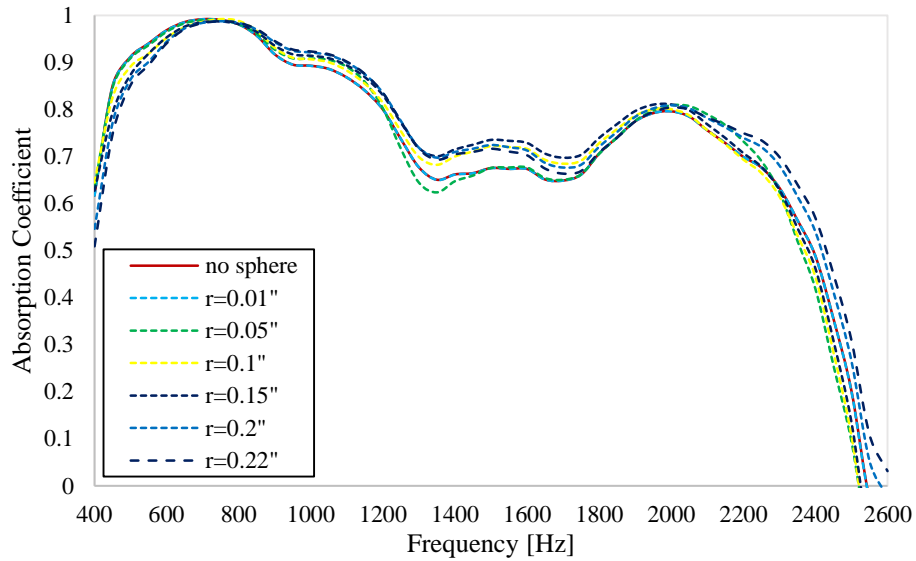


**Figure 76.** Absorption coefficient of 4 aluminum spheres embedded in melamine foam model. The addition of four spheres causes the absorption to increase over the entire range of 800 Hz – 2600 Hz. More of an effect is seen with the largest sphere radius. Finally, using a sphere radius of 0.22", the amount of spheres is varied and compared to each model from 1 sphere up to 4.

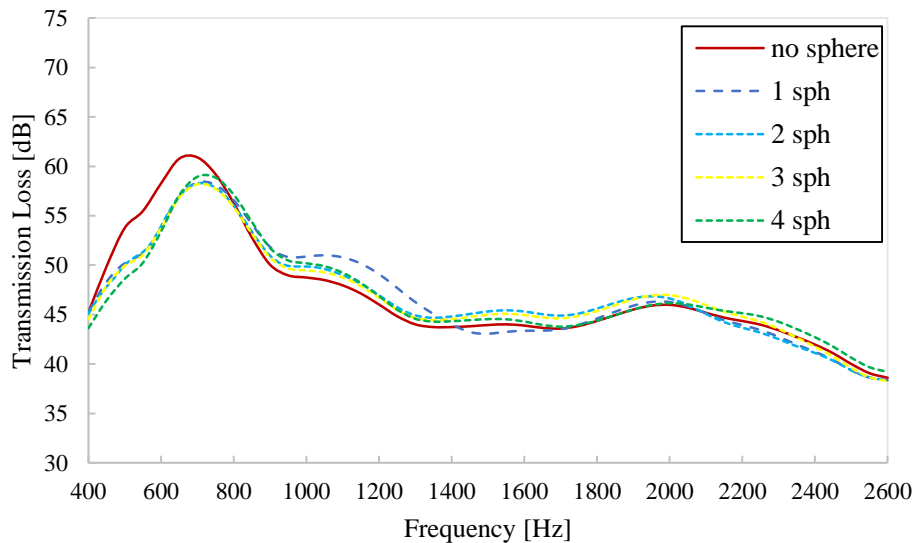


**Figure 77.** Transmission loss of 1-4 aluminum spheres embedded in melamine foam

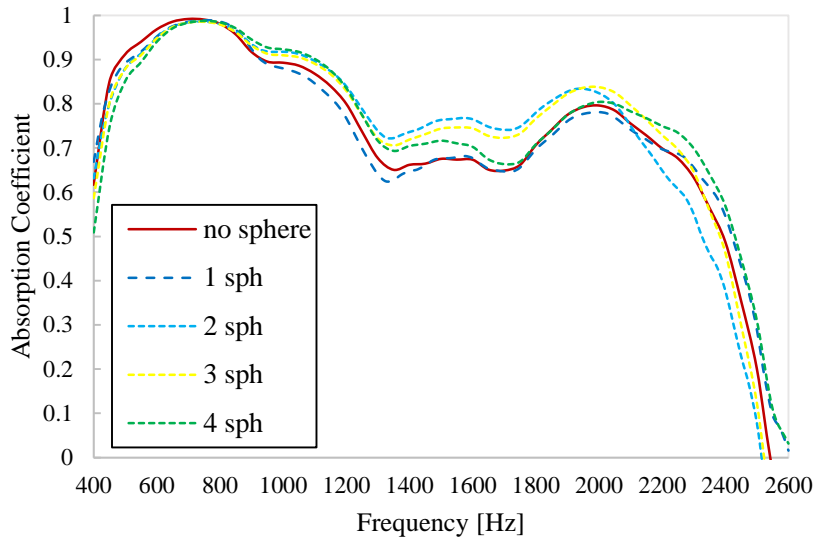


**Figure 78.** Absorption coefficient of 1-4 aluminum spheres embedded in melamine foam. From about 800-2500 Hz, the absorption was the highest when the model had two to three spheres placed inside. It is seen that the peak absorption coefficient is generally higher with a periodic arrangement and spacing within the masses. A higher number of spheres within each cell causes more diffraction effects to the impinging wave.

An additional sphere optimization study was performed, demonstrating the most effective position for one 0.2” radius sphere placed within each cell of the melamine-embedded liner. The optimum placement for the sphere resulted in 1.1 inches below the facesheet or top of the liner.

#### 4.5 Microperforated Acoustic Metamaterials

Initially, the three baseline liners (CD, VD, and PVD) are embedded with melamine foam within each chamber varying the height from 1 inch to the full 3 inches matching the liner depth in order to begin examining the effective behavior of foam. The inclusion of foam within each liner is built from the bottom of the liner up. The baseline models do not change their overall shape

or facesheet parameters, however. Hence, the partial variable depth liner filled with 2 inches of foam is shown in figure 79 below, where the foam is highlighted in purple.

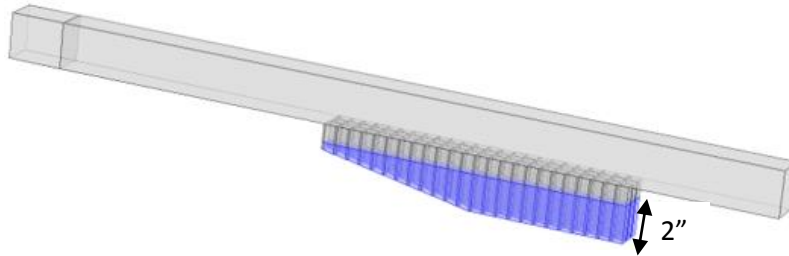
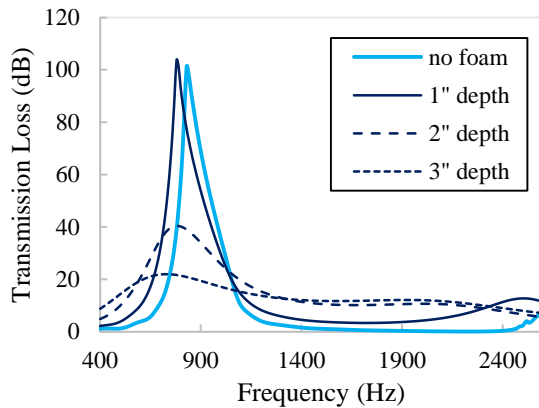
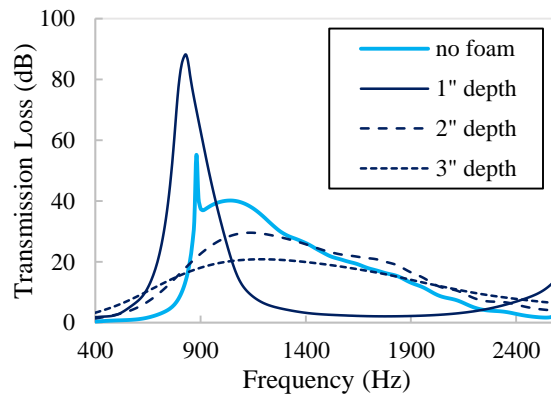


**Figure 79.** Partial variable depth with 2 inches of melamine embedded

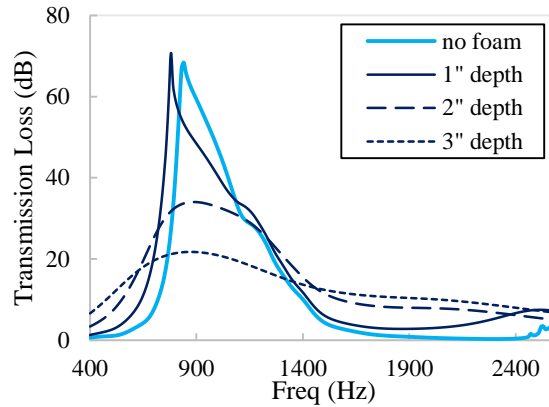
The figures below display the transmission loss of the three baseline models. With each baseline liner having a different general shape, the effect of the porous material will show diverse reactions depending on which liner is testing examined. Each case was tested with no foam as well and is plotted in light blue.



(a)



(b)



(c)

**Figure 80.** (a) Constant Depth liner embedded with melamine (b) Variable depth liner embedded with melamine and (c) Partial variable depth liner embedded with melamine

For the constant, variable, and partial variable depth liners, the addition of three inches of melamine foam proves to increase the attenuation broadband. The baseliner liners have the same parameters before, as well as the same facesheet. Increasing the amount of foam from 1 to 3 inches increases the TL about 10 dB in the frequency ranges from 400-700 Hz as well as 1400-2600. Specifically observing the CD liner versus the VD, the inclusion of the foam seems to show a more immediate effect on absorption in the VD liner since a wider range of depths are already being utilized. Since the results show that the more melamine embedded within each chamber the more broadband attenuation produced, the next step is to embed polyimide within each chamber which as a different flow resistivity of nearly  $30 \text{ kPa}\cdot\text{s}/\text{m}^2$ . The transmission loss plot of the CD, PVD, and VD liners embedded with melamine vs. polyimide is shown below in figure 81.

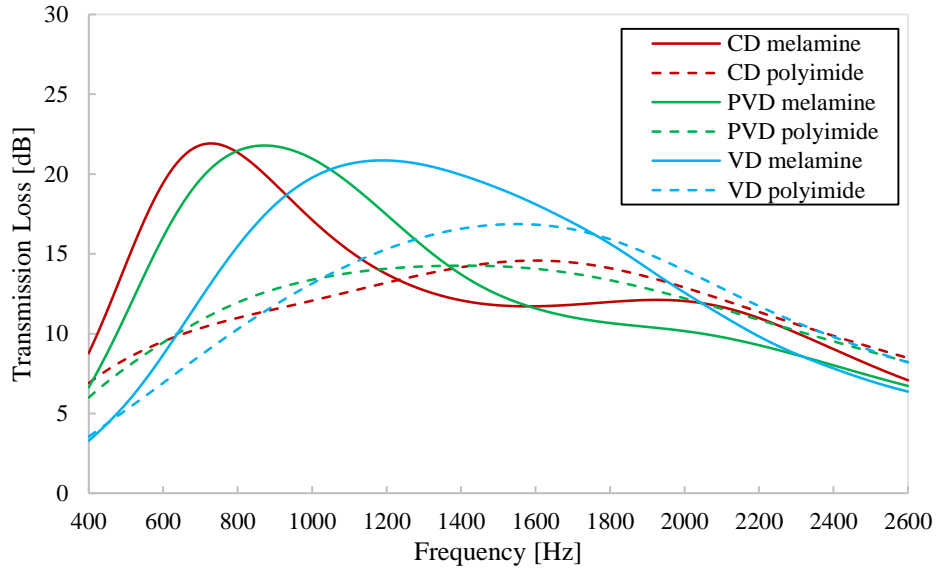


**Figure 81.** CD, VD, VD all embedded with melamine vs. polyimide

The melamine proves to be more effective at lower frequencies from approximately 400-1200 Hz. The polyimide acts as a better absorber in the higher frequencies from about 1400-2600 Hz. The equation for flow resistivity is effected by the parameters such as the porosity, as well as the density, therefore with these values will come different performance. Looking individually at the constant depth liner, the effect of the higher flow resistivity begins to take place at lower frequencies compared to the PVD and VD liners. Hence, the less variation in the shape of the liner, the more of an effect the higher flow resistivity has.

#### 4.5.1 Facesheet Studies

Sensitivity studies of the facesheet properties help explore the idea of controlling and manipulating its attenuation effects. In order to properly test these effects, the baseline model of the constant depth is used in varying these parameters. While keeping all other parameters constant, the porosity is varied first, followed by the plate thickness. The parameters for each facesheet are given below in table 14.

Table 14. Facesheet parameters for study

<b>Facesheet thickness</b>	0.0313''
<b>Porosity</b>	5.5%
<b>Hole diameter</b>	0.0385''
<b>Number of Holes</b>	1452

Figure 82 below demonstrates these effects.

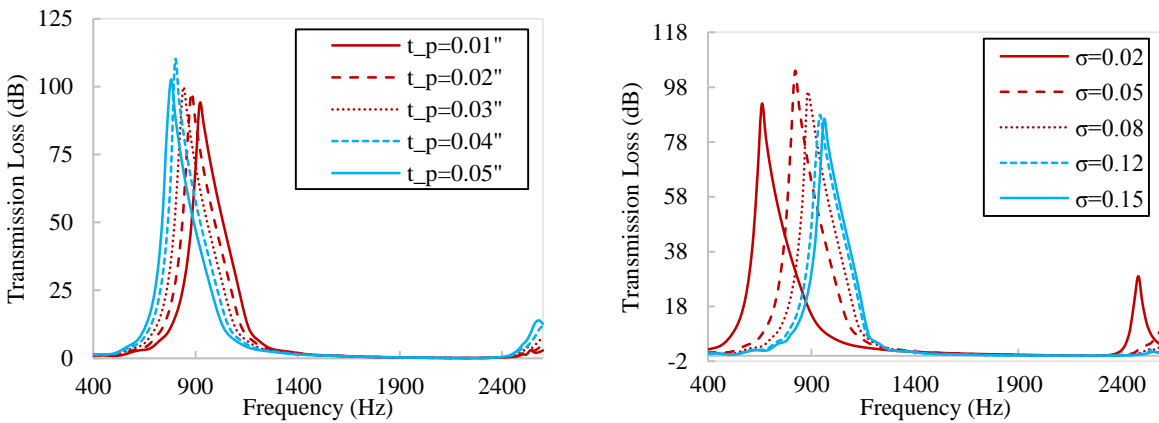


**Figure 82.** Transmission loss plot for constant depth plate thickness sweep (left) and porosity sweep (right)

By adjusting the porosity and plate thickness, it is possible to shift the curve to a desired resonant frequency. Acoustic resistance increases with decreasing porosity due to the increase in mass reactance. This then shifts the peak to a lower frequency. When the plate thickness increases, the peak of the transmission loss spectrum shifts to lower frequencies. In addition, the frequency region of high loss decreases as well.

#### 4.5.2 Microperforated Panel (MPP) Studies

Not only is there a need for sound absorbing materials, but also a need for a reclaimable, environmentally noncombustible attenuating materials. Microperforated panel (MPP) based metamaterials offer an increase in lower frequency sound absorption. They are rugged and cleanable and have been used in equipment, buildings, and silencers [43]. Their submillimeter size pores distort the flow of air and causes increased viscous friction. This translates to additional acoustic resistance therefore giving a highly effective absorber. Placement of the MPP will directly affect certain frequency bands. When the backing cavity is approximately one-quarter of the acoustic wavelength, the MPP absorbers are most effective. Therefore, the cavity depth indicates frequency at which the particle velocity is a maximum. The parameters for the MPP are shown below in table 15.

Table 15. Geometrical parameters for MPP

<b>Porosity [%]</b>	0.773
<b>Plate thickness [in]</b>	0.015
<b>Hole Diameter [in]</b>	0.008267717
<b>Flow Resistance</b>	0.4

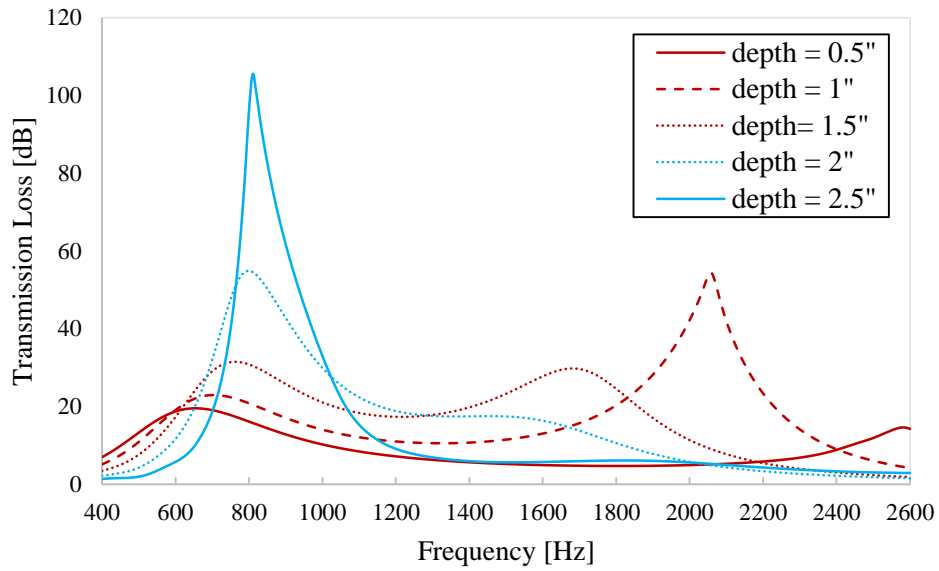


**Figure 83.** Constant depth MPP study examining MPP placement without melamine

Figure 83 shows that the closer the MPP is to the surface of the liner as the flow grazes it, the more effective it is broadband. As the air cavity backing the MPP embedded into the liner **increases in depth**, the peak attenuation and absorption shifts to lower frequencies.

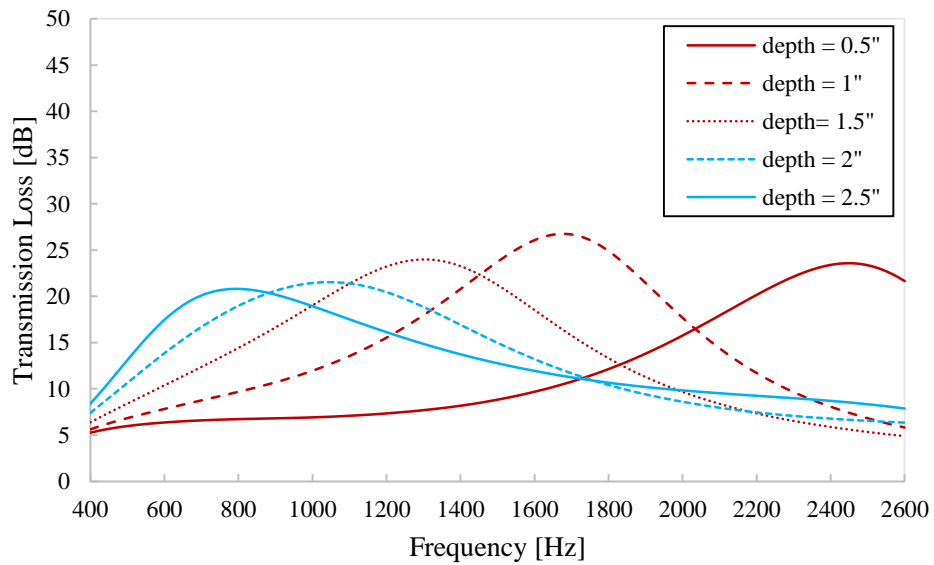


**Figure 84.** Constant depth MPP study examining MPP placement with melamine



The addition of melamine within each liner chamber gives more resistance and reactance therefore resulting in a more effective absorber. As MPP's are placed farther towards the bottom of the liner, the peak of the attenuation graph shifts to lower frequencies. This opposite effect is created with the addition of melamine. An image of the COMSOL models with 1 vs. 2 MPP's are shown below in figure 85.

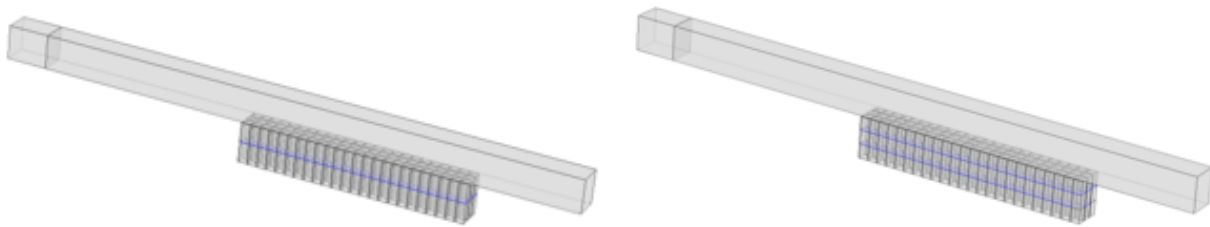


**Figure 85.** 1 MPP embedded within liner (left) and two MPP's embedded within liner equally spaced (right)

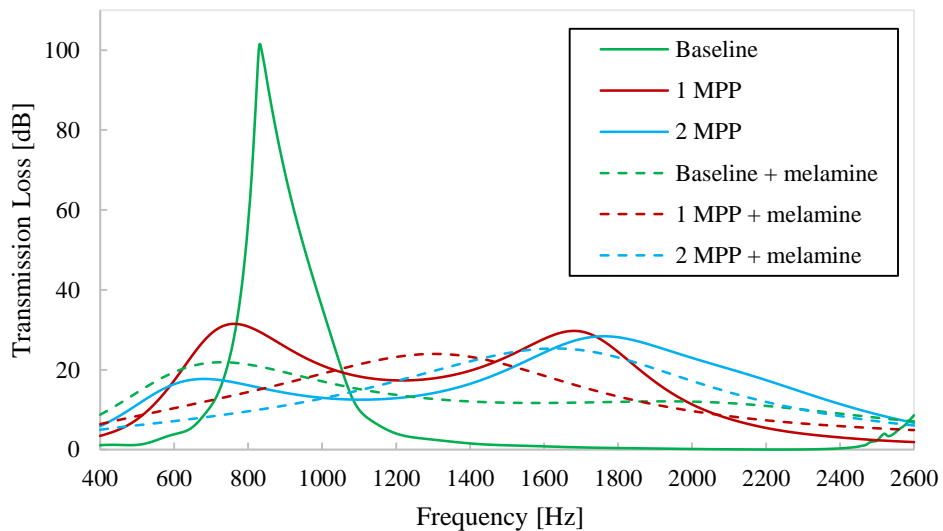


**Figure 86.** Constant depth MPP study with single and multiple MPP layers with and without melamine

When adding multiple MPP's into the liner with air as the surrounding domain as seen in the right figure in figure 85, the higher frequencies produce more attenuation. When there is melamine as

the surrounding domain, the peak merely shifts to the higher frequencies when more MPP's are added.

An additional optimization study was performed to find the most optimum location for the MPP that would result in the most attenuation. The initial guess for placement based on preliminary studies was 1 inch below the facesheet. After many iterations, the optimizer gave a location of 0.85938 inches below the facesheet, resulting in the maximum TL. The objective table showing the iterations for the maximum TL is shown below.

Table 16. Optimized location for MPP and corresponding TL

<b>Location (from facesheet)</b>
-1.00000054
-1.800000972
-1.400000756
-0.700000378
-1.300000702
-0.850000459
-0.700000378
-0.9250005
-0.775000418
-0.887500479
-0.812500439
-0.868750469
-0.887500479
-0.859375464
-0.850000459
-0.864062967
<b>-0.859375464</b>

#### 4.5.3 Additional Foam Designs

The final designs discussed involve placing the foam either above or below the liner; not embedding the melamine in between the liner walls. Model 1 is in the order of the facesheet, foam,

extruded cells; while model 2 is facesheet, extruded cells, and then foam. In general, a typical definition of a liner ‘system’ consists of the embedded facesheet; however with these varying designs, the facesheet is perhaps defined separately. The amount of foam for each model is 0.5 inches thick as well as 0.25 inches for both models designed. The transmission loss as well as absorption coefficient are shown below in figure 88.

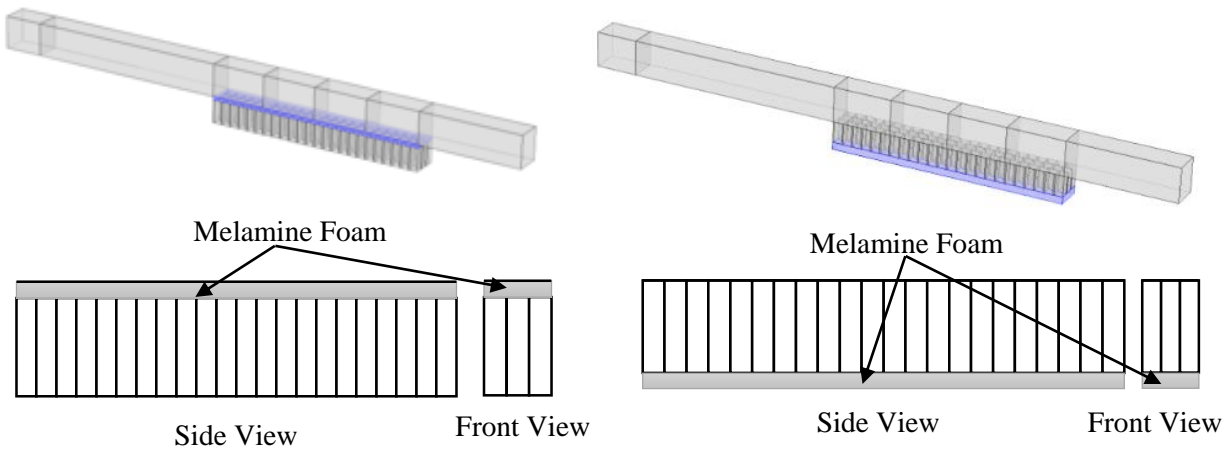


**Figure 87.** Model 1 (left) and Model 2 (right) with melamine highlighted in purple along with schematic diagram

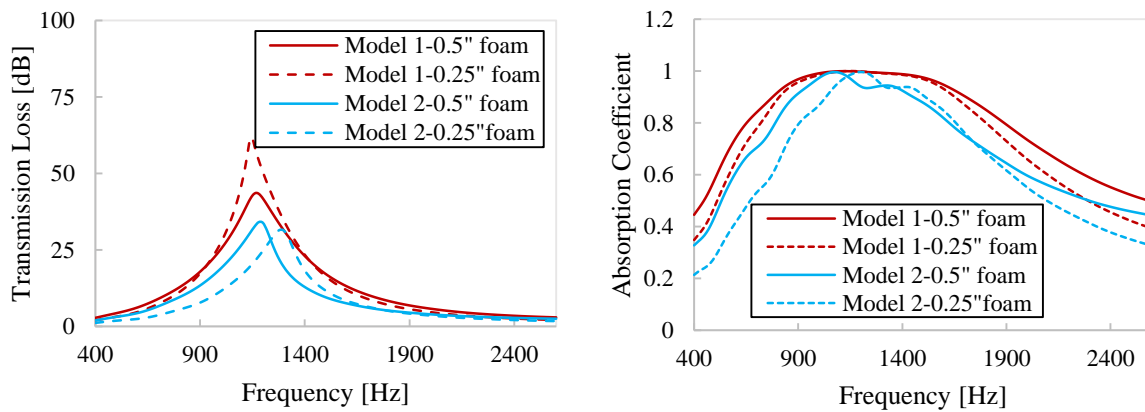


**Figure 88.** Transmission loss (left) and absorption coefficient (right) comparing models 1 and 2 with 0.25” and 0.5” melamine

Observing these graphs, the placement of the foam either on top of or below the liner shows significantly different effects as compared to the foam embedded within the cells. With the

melamine directly below the facesheet in model 1, the sound pressure travels through an immediate impedance change which shows to increase the TL in the range of 900-1500 Hz by at least 10 dB. By increasing the amount of foam from 0.25" to 0.5", the peak of the TL plot drops to only 50 dB rather than nearly 60, however it increases the absorption in the higher frequencies. When the foam is underneath the liner, the broadband absorption is not nearly as high. Increasing the depth of the foam from 0.25" to 0.5" shifted the peak to the left as if to simulate a deeper liner, however while keeping the overall depth constant. These different designs are also easier to manufacture since the porous material does not have to be directly placed within each cell.

The final design includes a combination of the spheres and MPP in order to maximize the absorption using the most optimized design. From the previous sections, the two studies on the optimized placement of the MPP and the sphere location are taken into account. The optimum MPP placement within the constant depth liner is at a location of 0.85938 inches below the facesheet, and the location for the optimum sphere is at a depth of 1.1 inches below. This design is seen below in figure 89.

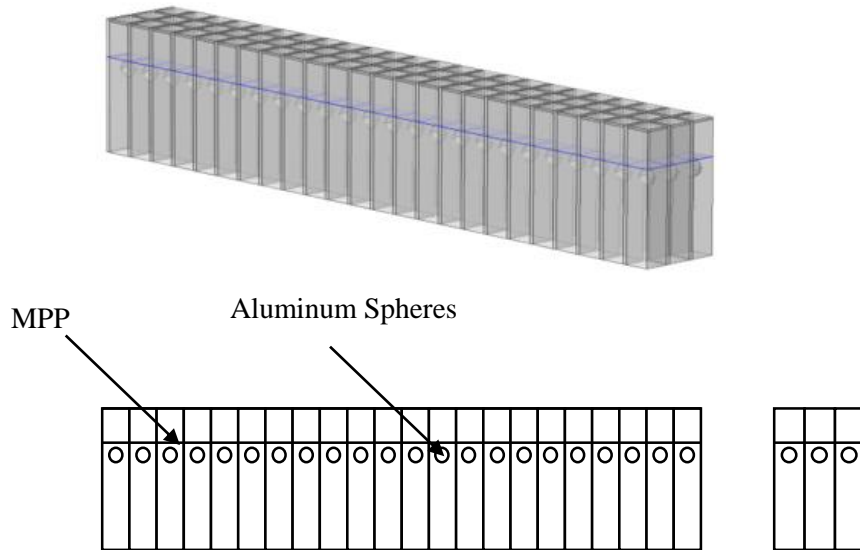


**Figure 89.** Optimized design with MPP highlighted in purple

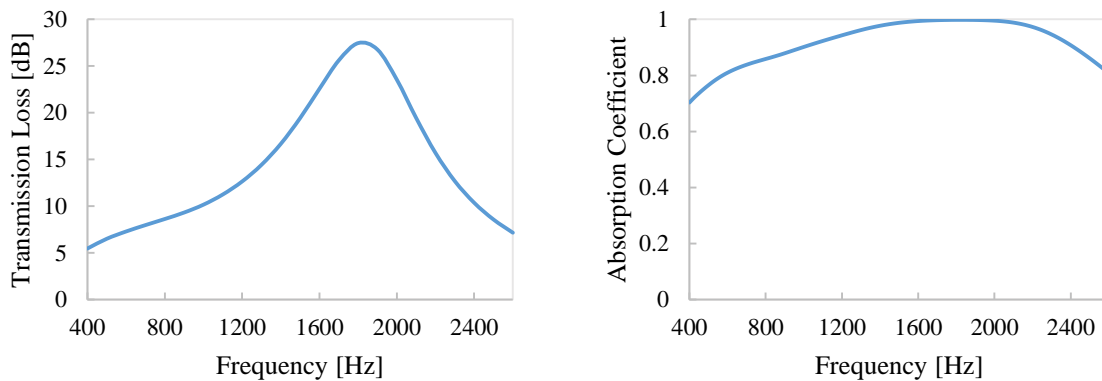


**Figure 90.** Transmission loss and absorption coefficient of optimized design

The model shows to produce at least 8 dB of attenuation of 80% of the frequencies. Nearing 2000 Hz the model is most absorbing, resulting in about 30 dB. A 3D total pressure plot at 1800 Hz where maximum attenuation is reached is shown below to demonstrate the effectiveness of the MPP and spheres.

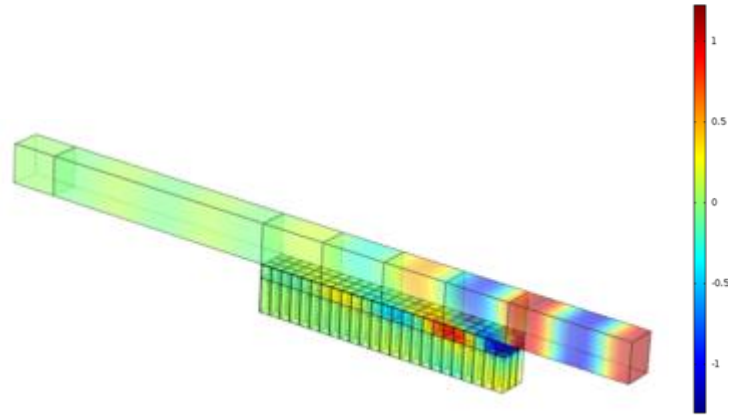


**Figure 91.** Total pressure propagation down the duct for optimized design at 2000 Hz

As seen from this pressure plot, as the pressure reaches the MPP there is a large drop in pressure as well as change in phase. The immediate impedance change causes this pressure drop and phase shift. When the sound wave has grazed approximately halfway down the liner, the pressure nearly dropped already 70%.

## 5 ADDITIONAL OPTIMIZATION STUDIES USING A SUMMED INTENSITY OBJECTIVE FUNCTION

### 5.1 Power output

An additional optimization study was performed by minimizing the linear intensity exiting the normal plane of the duct. By minimizing the sum of the intensity over the design frequency bandwidth over the exiting surface, the problem was able to be optimized in a way that observes the linear energy rate of flow. Observing the equation for intensity,

$$Intensity = \frac{Power}{Area} \propto P_{rms}^2, \quad \text{Eq. (45)}$$

it can be noted that these two values are directly proportional, but will have different values when optimized. The designs that result in the lowest amount of summed intensity (over the design frequency bandwidth) are therefore termed optimized and the corresponding total transmission loss is computed from these transmitted frequency summed intensity along with the incident frequency summed intensity. Images of the COMSOL interface where the defined objective function and corresponding summation are shown in the appendix for further guidance.

#### 5.1.1 Optimized MPP location

The constant depth liner embedded with melamine is the baseline model used to determine the optimum location for one MPP within the liner. Refer to table 15 for the parameters of the MPP. The resulting location for minimized frequency summed intensity resulted in a location of 2.58 inches below the facesheet and is seen in the table below.

Table 17. Optimization solver for optimum MPP location and corresponding intensity level

MPP Placement [in]	Intensity [W/m <sup>2</sup> ]
-1.400000756	5.05536E-03
-2.581103756	3.57299E-03
-1.990552256	4.72398E-03
-2.285828006	4.08420E-03
-2.433465881	3.79246E-03
-2.507284819	3.67202E-03
-2.544194287	3.61968E-03
<b>-2.581103756</b>	<b>3.57299E-03</b>

The corresponding intensity plot for the optimum MPP placement is shown below at all frequencies.

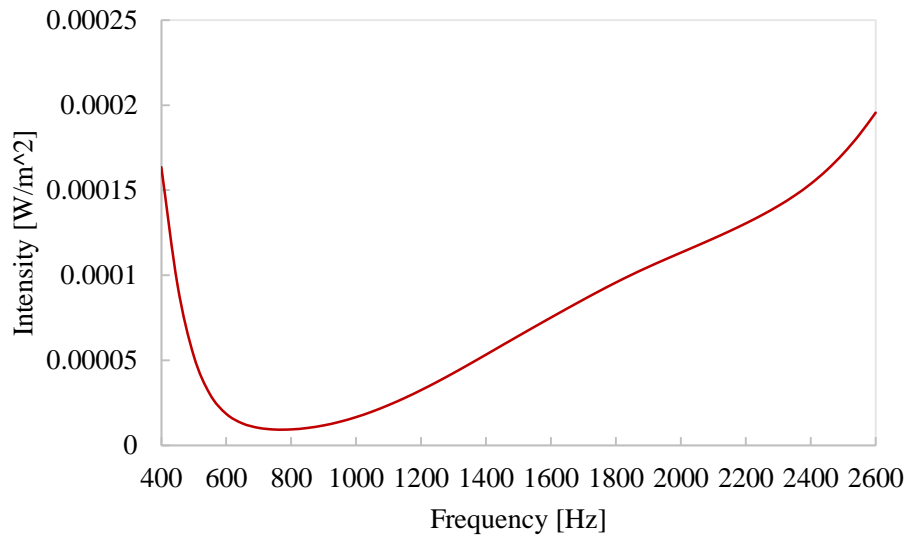


**Figure 92.** Intensity level across all frequencies for optimized MPP placement study

The corresponding transmission loss plot is shown below in figure 93.



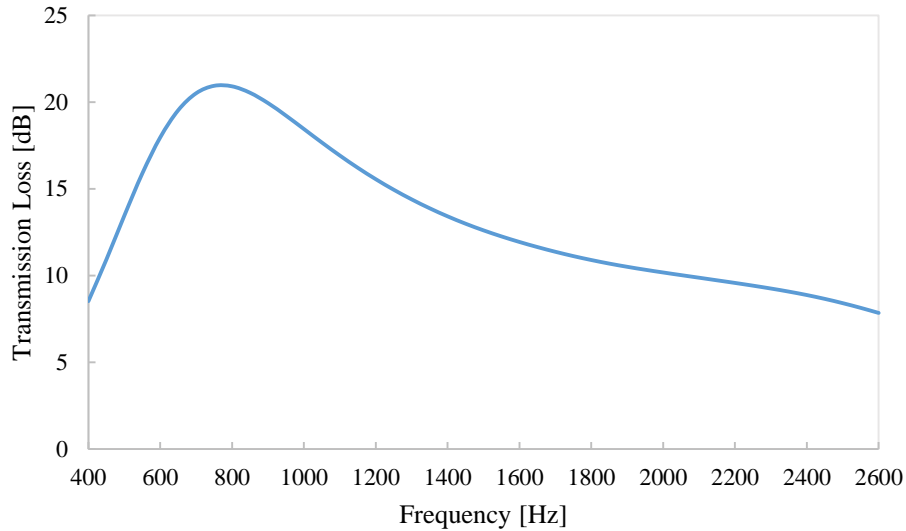


**Figure 93.** Transmission Loss of optimized MPP design

The overall total transmission loss over the design frequency bandwidth is computed to be a value of 24.9 dB summed across all frequencies in 25 Hz increments. This design gives 10 dB across nearly 90% of the frequencies tested. By adjusting the parameters of this MPP, the higher frequencies could be targeted more effectively by altering the plate thickness or porosity. Note that this value of 2.58 inches below the facesheet was very different from the location that the earlier optimization procedure (which summed the TL's directly) resulted in a value of approximately 0.9 inches.

### 5.1.2 Optimized Sphere location

The constant depth liner embedded with melamine and no MPP's was used as the baseline model to determine the optimum location for one aluminum sphere. The sphere was given a radius of 0.22" and could vary within the entire range of the depth of the liner which was up to 3 inches in depth. The optimization table is shown below.

Table 18. Optimization solver for sphere location and corresponding intensity level

Sphere location [in]	Intensity [W/m <sup>2</sup> ]
-1.10000594	4.0254E-02
-2.281103594	5.0925E-02
-1.690552094	2.9142E-02
-1.985827844	1.6826E-02
-2.50000135	7.9251E-02
-2.062205838	4.3012E-02
-2.390552472	1.3888E-02
-2.50000135	8.5221E-03
-2.335828033	7.9128E-03
-2.445276911	6.6020E-03
<b>-2.390552472</b>	<b>2.2117E-03</b>

The corresponding intensity plot is shown below across all frequencies.

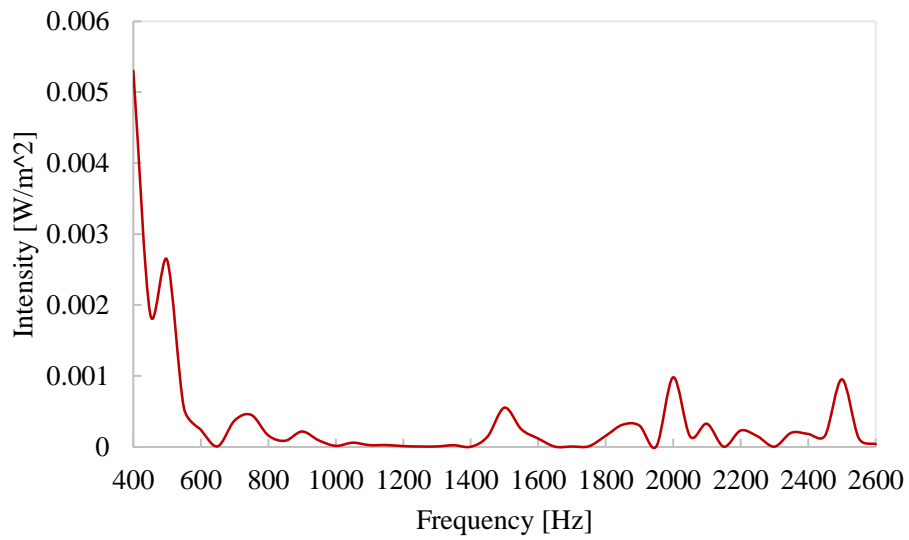


**Figure 94.** Intensity across all frequencies for optimized sphere placement study

The transmission loss plot is shown below in figure 95.

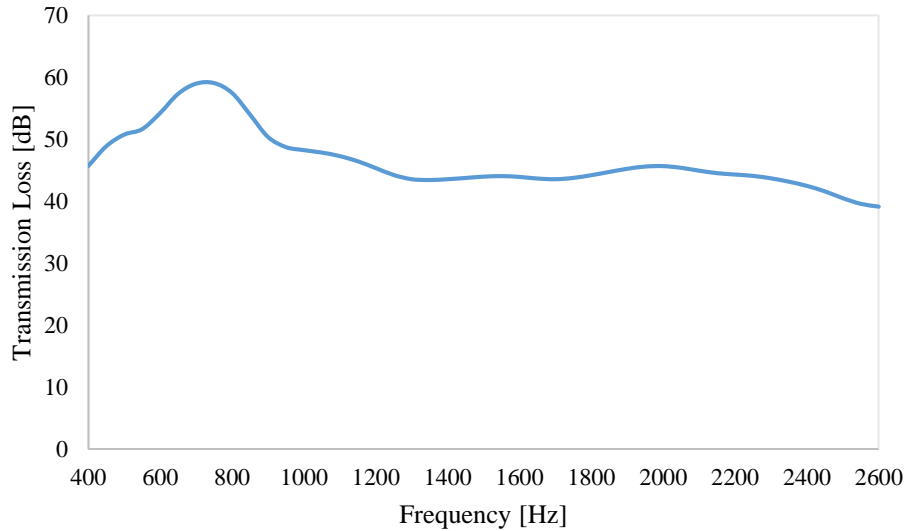


**Figure 95.** Transmission Loss of optimized sphere location

The total transmission loss results in a value of 66.8 dB summed across all frequencies in 25 Hz increments. This result shows very significant broadband performance, achieving around 40 dB for each frequency tested. The sphere is optimized to a location of 2.39 inches below the facesheet. Additional tests can be performed using multiple spheres where the varying parameter is the distance between each sphere.

### 5.1.3 Optimized MPP and Sphere Location Design

Looking at an entire metamaterial design, one MPP and one sphere are embedded within each liner cell to simulate the full spring-mass damper system. The system chosen to optimize uses the set location for the MPP placement and varies the sphere location. Since the optimum MPP placement was nearly 2.58 inches below the facesheet, the sphere was given a range of positions from 0.5 inches up to a depth of 2.3 inches approximately. An optimum location is calculated to be about 1.17 inches below the facesheet. The intensity level table is shown below.

Table 19. Optimization solver for sphere location with constant MPP and corresponding intensity level

Sphere placement [in]	Intensity [W/m <sup>2</sup> ]
-1.00000054	4.192754E-03
-1.700000918	5.007882E-03
-0.50000027	5.001665E-03
-1.50000081	4.793799E-03
-1.250000675	4.434739E-03
-1.181103	4.218773E-03
<b>-1.171260475</b>	<b>4.190492E-03</b>

The corresponding intensity plot is shown below across all frequencies.

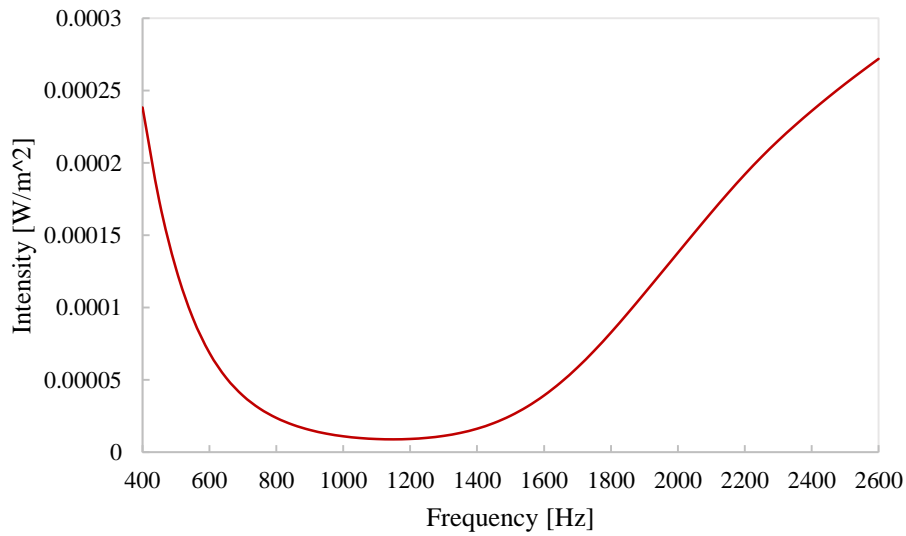


**Figure 96.** Intensity across all frequencies for optimized sphere placement study

The transmission plot is shown for this design below.

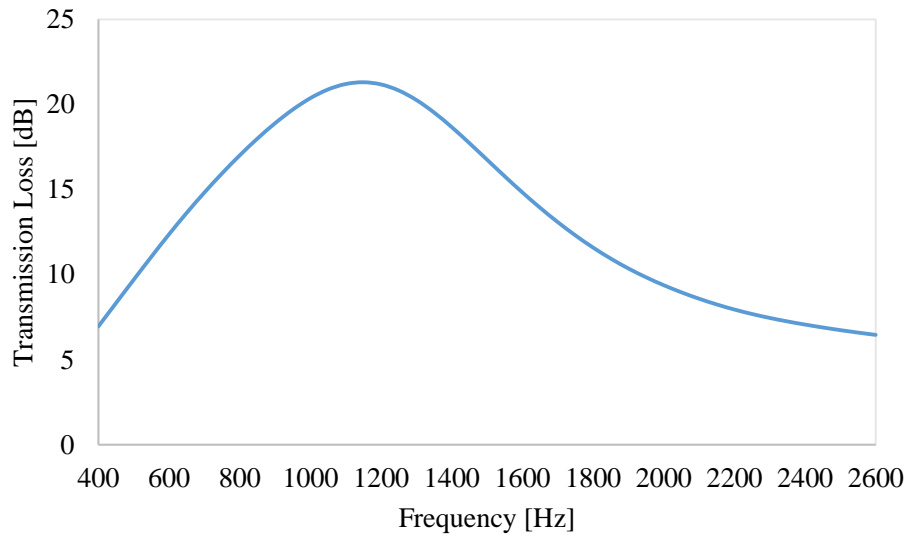


**Figure 97.** Transmission loss plot showing the optimum sphere and MPP design

The total transmission loss results in a value of 26.9 dB summed across all frequencies in 25 Hz increments. The peak TL is reached near 1200 Hz, resulting in a maximum TL value of 22 dB. Additional tests can be completed where the sphere remains in a fixed optimum location and the MPP is moved about the depth of the liner.

#### 5.1.4 Optimized Sinusoidal Shape

In addition, the sinusoidal shape in section 4.1.5 was optimized using this same minimizing intensity function. The point that varied within the shape had the same geometric bounds as did using the alternative summed transmission loss maximized approach. The corresponding table demonstrates that the most optimum point for minimized output power is at a location of -0.075 inches.

Table 20. Optimization solver for optimum design point and corresponding intensity level

Point [in]	Intensity [W/m <sup>2</sup> ]
-0.9	8.47018E-03
1.300001	1.35972E-02
0.2	7.98418E-03
1.300001	1.35972E-02
-0.35	7.85809E-03
-0.9	8.47018E-03
-0.075	7.82623E-03
0.2	7.98418E-03
-0.2125	7.82737E-03
<b>-0.075</b>	<b>7.82623E-03</b>

The corresponding intensity plot is shown below across all frequencies.

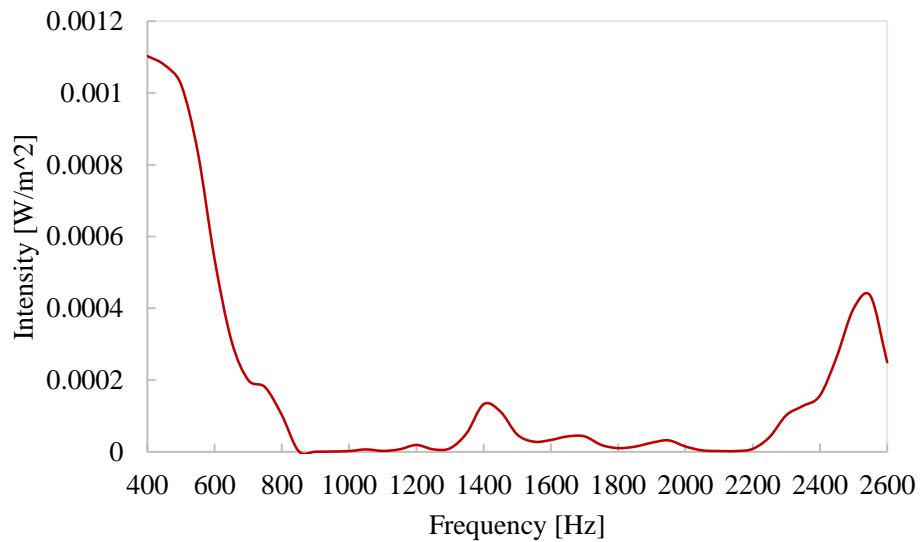


**Figure 98.** Intensity level across all frequencies for optimized point for sinusoidal design

The transmission loss plot is shown below in figure 99.

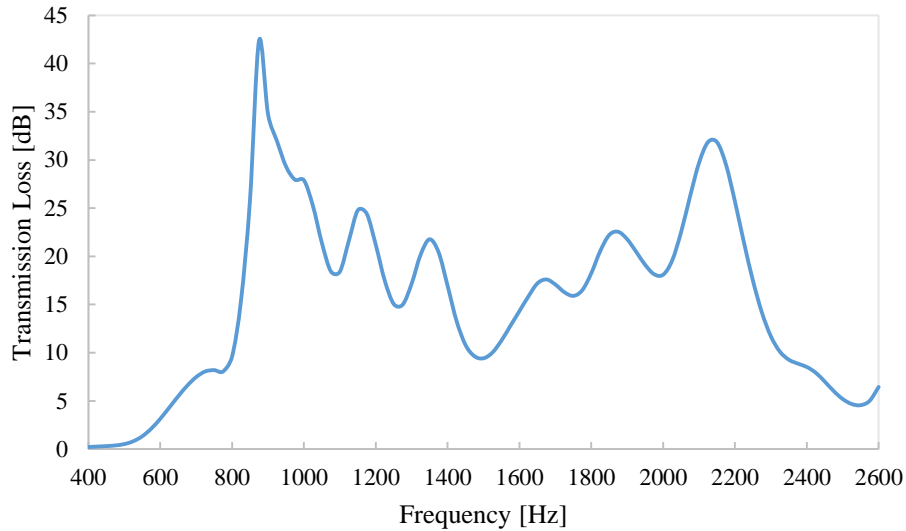


**Figure 99.** Transmission Loss of optimized sinusoidal design

The total transmission loss results in a value of 45.4 dB across all frequencies in 25 Hz increments. The plot peaks at a TL value of nearly 44 dB right around 900 Hz. This design performs very effectively broadband and achieves nearly 10 dB across 80 % of the frequencies tested. Note that this design does not include any sort of porous material. Within the range of 400-800 the design is not very effective, thus the design would benefit from the inclusion of a porous material since it is highly effective at absorbing within this range.

#### 5.1.5 Optimized Flow Resistivity Value

Looking specifically at just the melamine model where a block of foam is embedded within each constant depth cell, the flow resistivity is varied. An initial guess of 12 kPa·s/m<sup>2</sup> is used, and a final value of 10 kPa·s/m<sup>2</sup> is concluded to give the minimum power outputted. The table below demonstrates the iterations from the optimized solver.

Table 21. Optimization solver for optimum flow resistivity and corresponding intensity level

Flow Resistivity Pa·s/m <sup>2</sup>	Intensity [W/m <sup>2</sup> ]
12000	4.8686E-03
12150	4.8892E-03
11850	4.8484E-03
11700	4.8286E-03
11400	4.7900E-03
11100	4.7531E-03
10500	4.6843E-03
10000	4.6328E-03
10550	4.6898E-03
10275	4.6605E-03
10137.5	4.6464E-03
10068.75	4.6396E-03
10034.375	4.6362E-03
10017.1875	4.6345E-03
10008.59375	4.6336E-03
10004.29688	4.6332E-03
<b>10000</b>	<b>4.6328E-03</b>

The corresponding intensity plot is shown below across all frequencies.

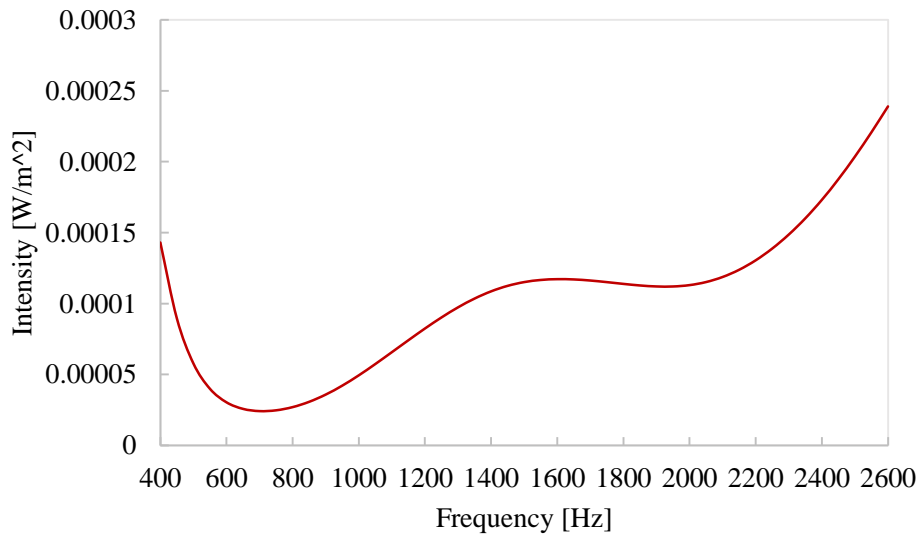


**Figure 100.** Intensity plot across all frequencies for optimized flow resistivity design

The transmission loss plot is shown below in figure 101.



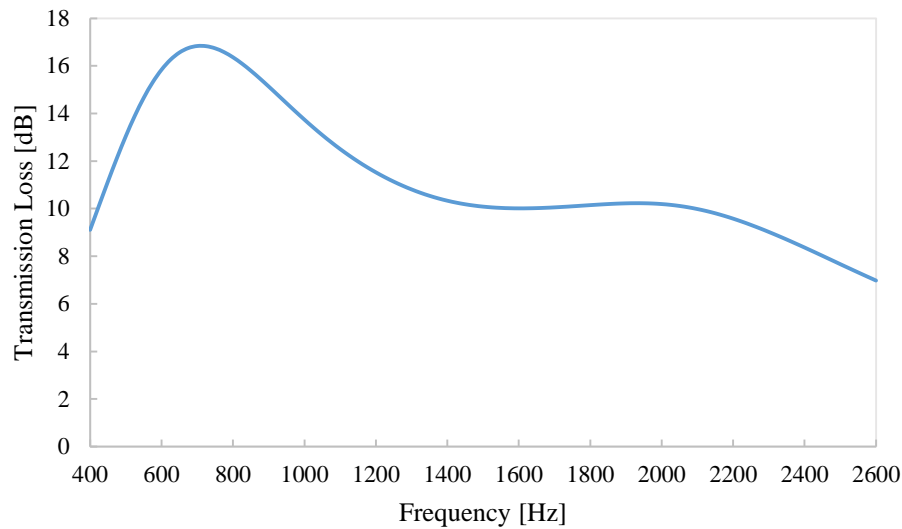


**Figure 101.** Transmission Loss of optimized flow resistivity result

The total transmission loss results in a value of 28.7 dB across all frequencies in 25 Hz increments. The TL plot peaks right around 700 Hz. In general the lower the flow resistivity, the higher the absorption within the lower frequency range. There is nearly 10 dB achieved for almost 80% of the frequencies tested. Note that this is only for this specific configuration. Future work can be done that will include embedded masses as well, before the flow resistivity is varied.

Multiple optimization problems can be setup using this finite element solver. The most physically correct way to maximize attenuation and reduce overall acoustic power is to use this optimization procedure which utilizes minimizing an objective function based upon transmitted intensity summed at all frequencies of interest in the design process.

## 6 AEROACOUSTIC STUDIES

Sound propagation with flow interaction over a liner is more indicative of its behavior inside a moving engine. Recent efforts provide advancements in accurately modeling a liner in the presence of flow. This current section briefly discusses the effects of flow up to speeds of  $M=0.3$  on conventional acoustic liners. The downstream flow travels in the same direction as the sound propagation through the duct.

### 6.1 Flow Design Studies

In this section, some of the same models tested without flow will be analyzed with the inclusion of flow up to speeds of  $M=0.3$ . Parameter studies on the facesheet properties such as porosity, plate thickness, and hole diameter will be observed as well. The constant depth, variable depth, and partial variable depth will initially be tested comparing speeds of  $M=0$ ,  $0.15$ , and  $0.3$ . These transmission loss plots are shown below.

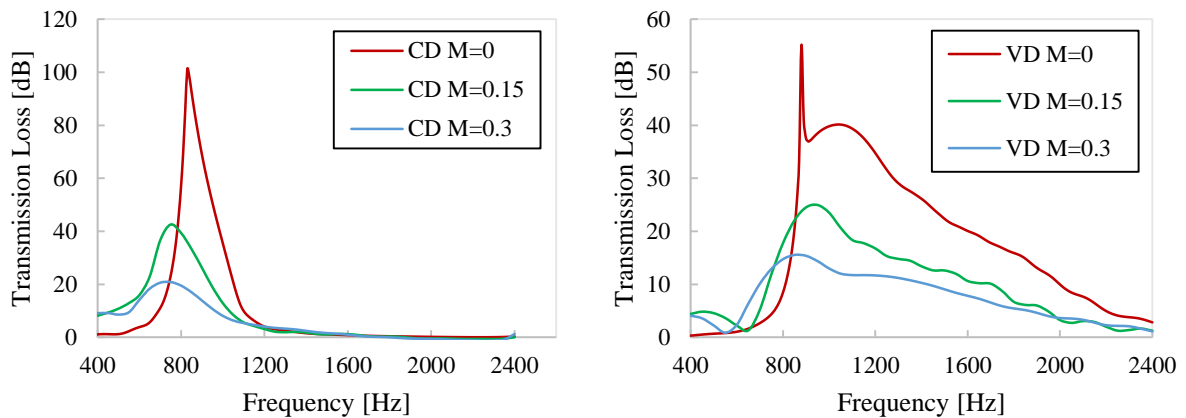


**Figure 102.** Transmission plot of the constant depth liner (left) and the variable depth liner (right) for speeds of  $M=0-0.3$

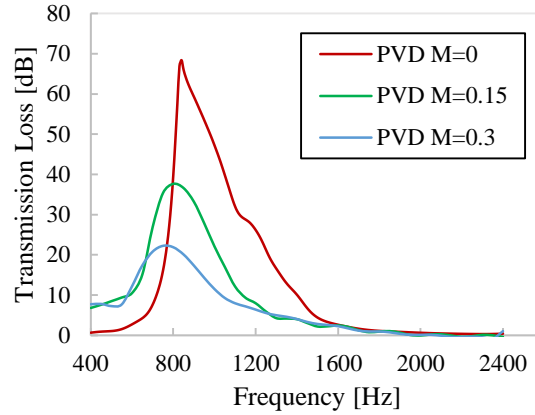


**Figure 103.** Transmission loss plot of the partial variable depth liner for speeds  $M=0-0.3$

The addition of flow tends to affect all three conventional liners in the same manner in this current liner investigation. While the flow speed is increasing, the amount of attenuation gradually decreases. As the flow speed gradually increases, the aeroacoustic behavior causes the sound. The peak attenuation also shifts to the lower frequencies with increasing Mach number.

The main absorption mechanism is the acoustic-vortex interaction. Therefore, varying any of the facesheet parameters will have a direction effect on the absorption. The acoustic resistance is dependent upon the boundary layer thickness  $\delta$ , hole diameter  $d$ , Mach number  $M$ , and porosity  $\sigma$ , based on the Rice and Homyak modification [44] and is given as below,

$$\theta = \frac{Mgf}{\sigma(2+1.256\frac{\delta}{d})} \quad \text{Eq. (46)}$$

demonstrating that the increase in porosity will in general decrease the resistance. In addition, the increase in boundary layer thickness will also decrease the resistance [45]. The porosity and plate thickness were examined for  $M=0.3$  flow. The porosity varied from 5.5% to 15%, and the plate thickness from 0.02” to 0.07”.

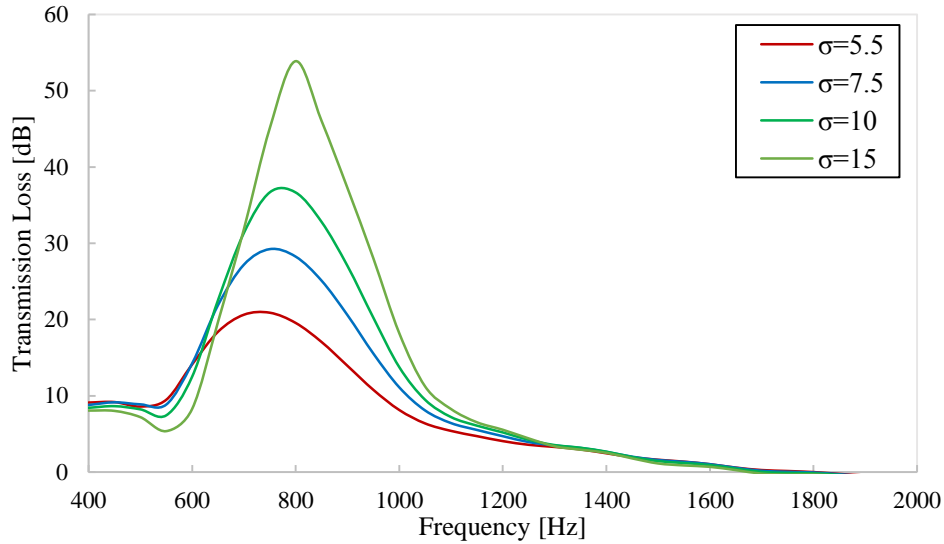


**Figure 104.** Transmission loss plot of constant depth liner with porosity sweep

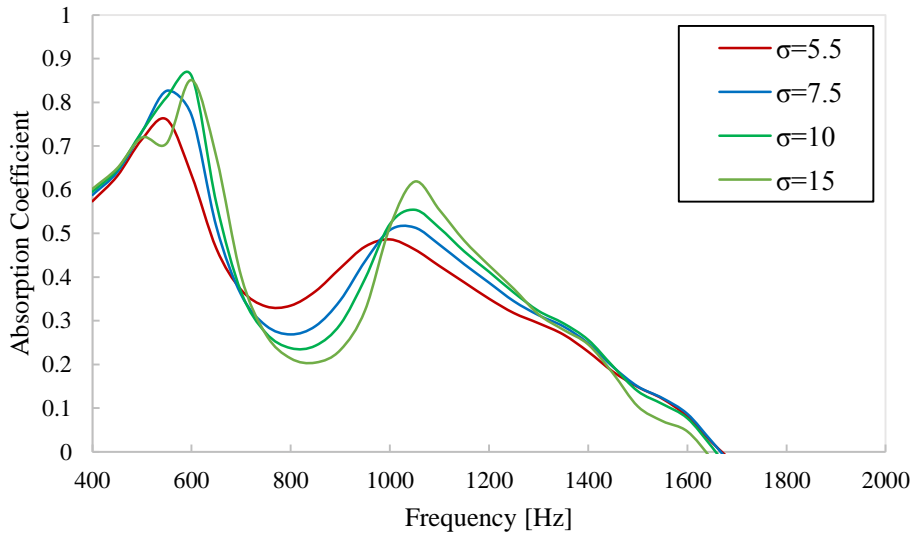


**Figure 105.** Absorption coefficient of constant depth liner with porosity sweep

As the porosity increases, within the range of 600-1200 Hz, the transmission loss increase at least 10 dB each porosity value. With a higher porosity, the flow will be able to travel into the facesheet due to the additional resistance and reactance. This behavior is increasingly significant over the porosity values at hand. The absorption coefficient, however, is negatively affected within the

range of 700-1000 Hz due to the inability for the liner to intake and absorb the flow due the decrease in boundary layer thickness.

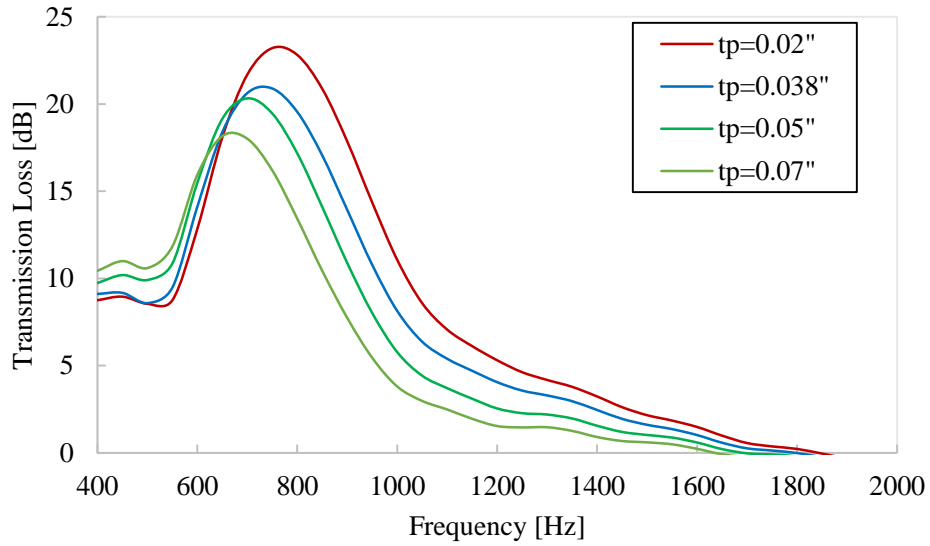


**Figure 106.** Transmission loss plot of constant depth liner with plate thickness sweep

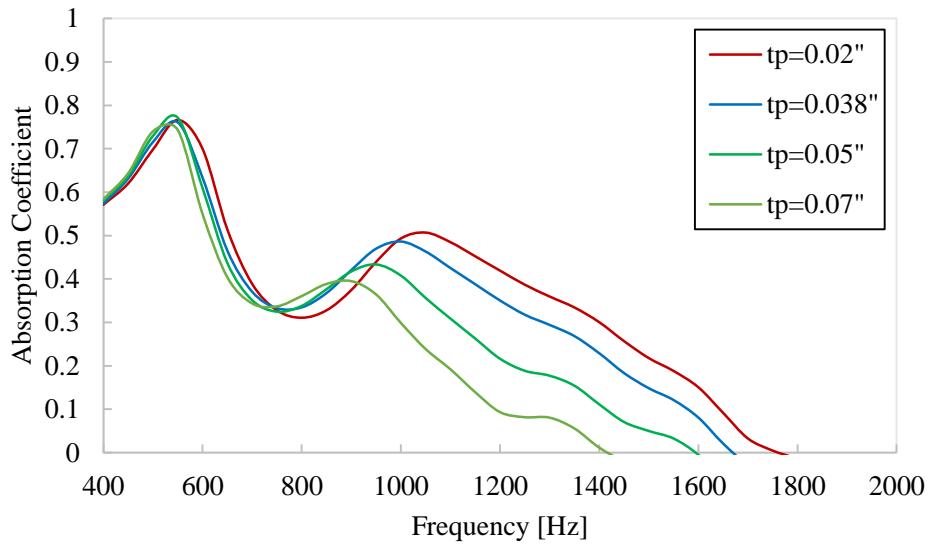


**Figure 107.** Absorption coefficient plot for the constant depth liner with plate thickness sweep

These results show that the larger the plate thickness, the less transmission loss produced. A thicker plate would require more material but it would also create a greater boundary layer thickness due

to the increase in hole depth. It is seen in the absorption coefficient that the higher frequencies are only significantly affected by the change in plate thickness.

6.2 Optimum Flow Design Comparison

Finally, the optimized liner discussed in the previous chapter was run in  $M=0.3$  flow as to compare with the no flow case. The TL and absorption plot are shown below.

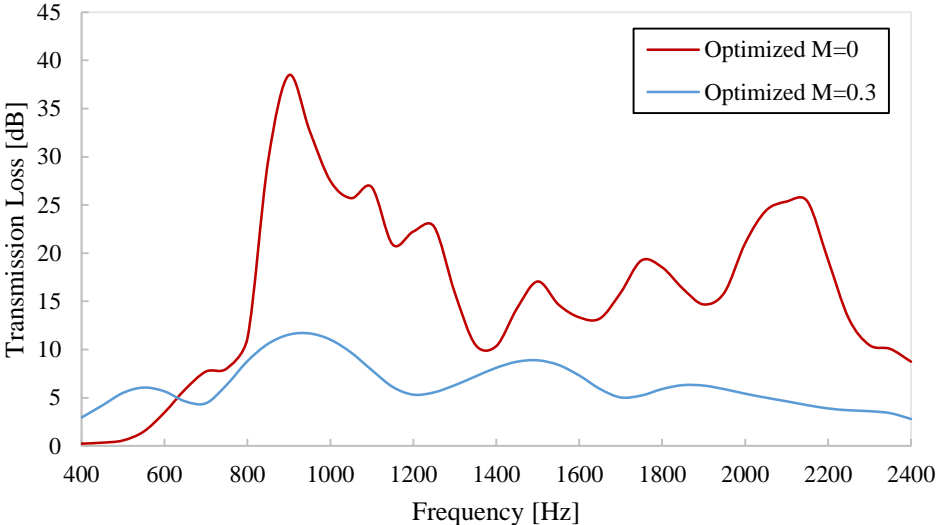


**Figure 108.** Transmission loss plot for optimized design at  $M=0$  and  $M=0.3$  flow

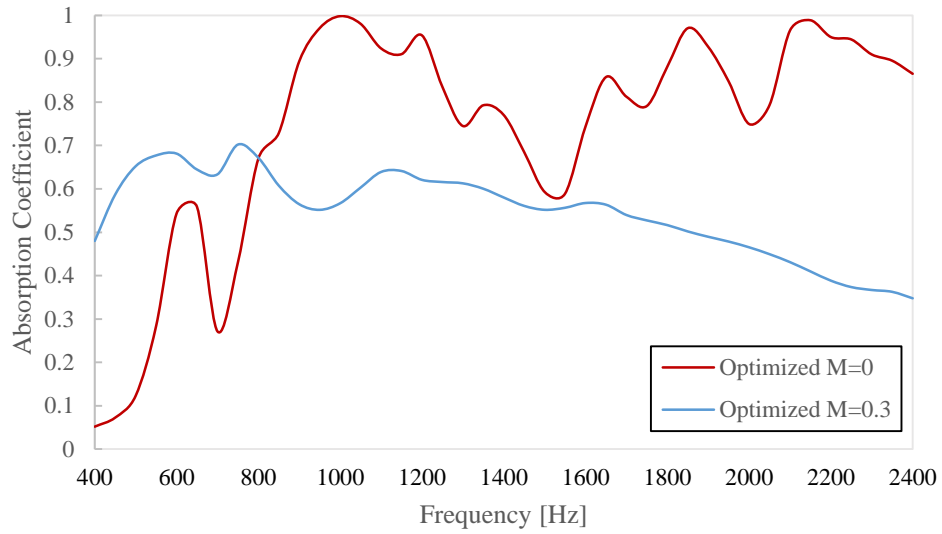


**Figure 109.** Absorption coefficient plot for optimized design at M=0 and M=0.3 flow

This trend follows previous explanation of the inclusion of flow decreasing the over attenuation from a liner. The transmission loss plot smoothens out as well, causing less peaks. The 3D total pressure plots at 2100 Hz are shown below demonstrating how much more effective the liner is without flow.

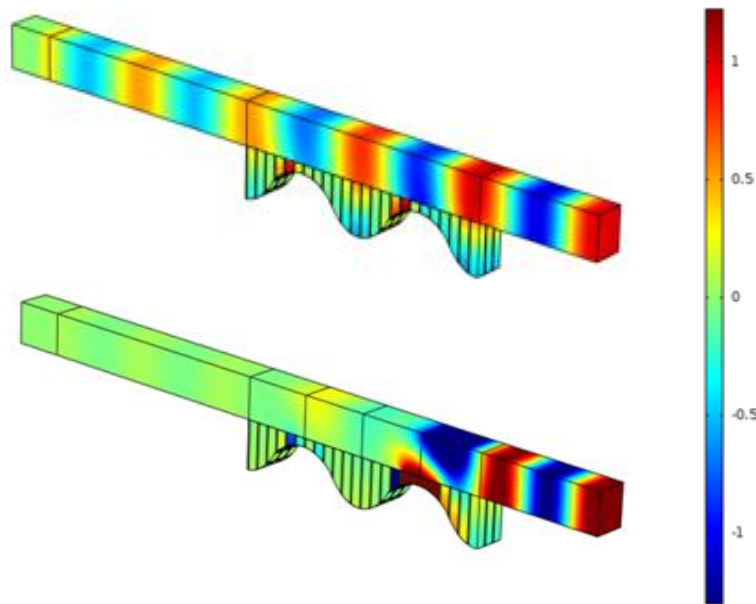


**Figure 110.** Total pressure for  $f=1200$  Hz with flow (above) and without flow (below)

Observing the top liner where flow is included, the maximum pressure amplitude does not nearly decrease as quickly as the model without flow. In general this is a consistent trend within each liner tested.



## 7 CONCLUSIONS

Throughout this research, acoustic liners have been investigated and designed with and without a metamaterial incorporation to achieve broadband attenuation within the range of 400-2600 Hz. Porous foams, microperforated plates, as well as aluminum spheres have been implemented as a form of acoustic metamaterials that can be optimized to create broadband absorption and attenuation.

Beginning with an acoustic liner shape study, a conventional constant depth liner was tested with zero flow within the frequency range of 400-2600 Hz. This led to a variable depth study that used the optimization tool to give final geometric dimensions as to minimize the sum of the intensity and hence maximize the transmission loss. The maximum depth allowed for any part of the extrusion was kept at a set amount of 3 inches. The final optimized shape looks similar to a sinusoidal wave extrusion throughout the length of the duct.

In order to begin simulating a full metamaterial design, a porous foam was embedded within the liner at different locations with different properties. Melamine and polyimide proved to have effective absorbing material properties that provide flow resistivity to dramatically suppress sound radiation. Sensitivity studies were then performed on the seven properties that define a porous material. From here the addition of microperforated plates was then studied within the porous-filled liner. By specifically placing the MPP at certain depths within the liner, desired bandwidths could be targeted. The inclusion of embedded aluminum spheres within the porous foam was the final step in creating an acoustic metamaterial. The radius of the sphere as well as the placement of the sphere within each cell was varied. While holding all other parameters constant, sensitivity studies on the geometric parameters for the facesheet were then analyzed to

show their tunability. The optimization solver was used on these porous designs to give the most effective parameter value to minimize the exiting power and maximize the attenuation.

The incorporation of flow was an additional study used on the three baseline acoustic liners in order to observe flow effects on liner performance. The resistive facesheet was the main system component that defined the behavior of the overall acoustic liner with flow. Final conclusions of the work are shown below in bulleted format.

- The constant depth showed poor broadband performance with the lack of depth variation down the duct
- The optimized sinusoidal model was able to produce 10 dB across nearly 80% of the frequencies
- Melamine proved to be more effective within the frequency range of 400-1800 Hz, while polyimide resulted in better absorption from 1800-2600 Hz
- A flow resistivity of 10,000 Pa·s/m<sup>2</sup>, porosity of 0.99, tortuosity of 0.2, permeability of 1e-9 m<sup>2</sup>, and density of 9.85 kg/m<sup>3</sup> resulted in the maximum amount of attenuation possible with the foam embedded with each constant depth chamber
- The addition of microperforated plates caused an increase in resistance within the liner and therefore produced more attenuation over the frequency range
- When there were air cavities separating the MPP from the facesheet, two MPP's spaced evenly were most productive in absorbing sound
- When the MPP's were surrounded by melamine, the more MPP's added, the higher the absorption in the upper frequencies
- When placing the MPP at a certain depth within the liner, the transmission loss would increase in the upper frequencies the closer the MPP was to the facesheet of the liner

- An optimization study that placed the MPP in the position for least power outputted resulted in a location of 2.58 inches below the facesheet
- Decreasing the porosity increases the acoustic resistance due to the increase in mass reactance. As well, an increase in plate thickness causes the transmission loss peak to shift to lower frequencies
- The inclusion of embedded aluminum spheres are effective between the frequency ranges of 1000-2600 Hz by acting as dynamic vibration absorbers
- By increasing the amount of spheres within the melamine foam, as well as the sphere radius, more absorption was produced in the higher frequencies
- An optimization study located the depth at which one sphere within each liner cell would produce the minimum power which resulted in a location of 2.39 inches below the facesheet
- For the constant depth, variable depth, and partial variable depth liners, the higher the flow speed, the lower the transmission loss broadband
- An increase in plate thickness causes a decrease in absorption due to the increase in boundary layer thickness as the flow passes over deeper holes within the facesheet

## 8 FUTURE WORK

Future work will consist of additional metamaterial designs that vary the parameters of the material in which the masses are embedded in. By exploring other foam concepts that have the foam sitting as a block below the liner or directly below the facesheet but above the extruded cells will also provide good feedback as to how avoid such an increase in mass and manufacturing costs. Additional MPP studies including embedding up to 5 or 6 plates within a liner and performing sensitivity studies on those parameters will extend this work as well.

By utilizing the optimization tool in COMSOL, the metamaterial design can be explored with flow. This will allow a more realistic interpretation on how the porous foam will behave with different temperatures, Mach, etc. In addition, the embedded masses will tend to vibrate inside the foam with high flow speeds grazing it, which could cause dramatic effects.

Future work will also include large-scale modeling using the same finite element tool in order to make sure the correct impedance values are captured over a larger frequency range. At NASA Langley they are focusing on the advancement of the GFIT in order to include frequencies up to 6000 Hz rather than the maximum as 3000 Hz. The inclusion of higher order modes will have a different effect on the performance which will be inclusive if the test section is larger and different frequencies are tested. By incorporating a third dimension within the liner design, a multiple degree of freedom (MDOF) liner can be explored as well.

## APPENDIX

### REFERENCES

- [1] "Aircraft Noise Issues," April 2015. [Online]. Available: [https://www.faa.gov/about/office\\_org/headquarters\\_offices/apl/noise\\_emissions/airport\\_aircraft\\_noise\\_issues/](https://www.faa.gov/about/office_org/headquarters_offices/apl/noise_emissions/airport_aircraft_noise_issues/).
- [2] A. Kempton, "Acoustic Liners for Modern Aero-engines," University of Southampton, 2011.
- [3] C. L. Barnobi, *Improvement in Acoustic Liner Attenuation In Turbofan Engines by Means of Plasma Synthetic Jet Actuator*, Blacksburg: Virginia Tech Institute and State University, 2010.
- [4] C. R. F. a. R. L. Harne, "Advanced Passive Treatment of Low Frequency Sound and Vibration," *ACOUSTICS*, 23-25 November 2009.
- [5] K. K. V. a. S. A. Nayfeh, "Vibration Damping by Coupling to Lossy Low-Wave-Speed Media," in *Smart Structures and Materials*, 2003.
- [6] B. T. M. W. R. W. a. T. P. M. G. Jones, *Effects of Liner Geometry on Acoustic Impedance*, Hampton : AIAA, 2002.
- [7] J. A. P. M. Rie Sugimoto, "Low Frequency Liners for Turbofan Engines," *20th International Congress on Acoustics*, pp. 1-4, 2010.
- [8] A. Slagle, *Low Frequency Noise Reduction Using Novel Poro-Elastic Acoustic Metamaterials*, Blacksburg, Virginia : Virginia Tech , 2014.
- [9] M. M. Light, "Our Perspective on Optimal Metamaterials".
- [10] S. W. R. & A. Hirschberg, *An Introduction to Acoustics*, Eindhoven University of Technology, 2004.
- [11] K. J. Bauemeister, *Optimized Multisectioned Acoustic Liners*, New Orleans, 1979, p. 10 .
- [12] A. H. J. Y. J. K. G. Bielak, "Advanced Nacelle Acoustic Liner Concepts Development," Hampton , 2002.
- [13] F. H. S. C. S. A. S. M. J. Paul T. Soderman, "Design and Development of a Deep Acoustic Lining for the 40- by 80-Foot Wind Tunnel Test Section," NAAA/TP-2002-211850, Moffett Field, 2002.
- [14] G. G., "Propagation of Acoustic Waves in a One-dimensional Macroscopically Inhomogeneous Poroelastic Material," *Acoustical Society of America*, September 2011.
- [15] P. Marcotte, *A Study of Distributed Active Vibration Absorbers (DAVA)*, Virginia: Virginia Tech , 2004.

- [16] S. Zhang, *Acoustic Metamaterial Design and Applications*, University of Illinois at Urbana-Champaign, 2010, p. 3.
- [17] K. Idrisi, *Heterogeneous (HG) Blankets for Improved Aircraft Interior Noise Reduction*, J. C. R. C. Marty Johnson, Ed., Blacksburg, 2008.
- [18] D. L. a. M. G. J. Sufliiff, "Foam-Metal Liner Attenuation of Low-Speed Fan Noise," in *AIAA*, NASA Glenn and NASA Langley.
- [19] J. Nichols, "Theoretical and Experimental Comparison of Pressure in a Standing Wave Tube with Attenuation".
- [20] D. M. N. a. M. G. Jones, *Broadband Liner Optimization for the Source Diagnostic Test Fan*, Colorado Springs, Colorado, 2012.
- [21] J. H. Lan, *Turbofan Duct Propagation Model*, NASA , 2001.
- [22] H. C. L. a. T. L. Parrott, "Application of Finite Element Methodology for Computing Grazing Incidence Wave Structure in an Impedance Tube: Comparison with Experiment," 5th AIAA Aeroacoustics Conference, AIAA Paper, 1979.
- [23] J. F. Betts, "Finite Element Study of Plane Wave Acoustic Phenomena in Ducts," Blacksburg, 1998.
- [24] COMSOL, "Introduction to Acoustics Module," COMSOL, 2013. [Online]. Available: <http://www.comsol.com/models/acoustics-module> .
- [25] Berkeley, "Introduction to Finite Element Modeling".
- [26] C. H. Hansen, *Fundamentals of Acoustics*, South Australia: Department of Mechanical Engineering, University of Adelaide .
- [27] A. Färm, *Analysis of Acoustic Absorption with Extended Liner Reaction and Grazing Flow*, Stockholm : Licentiate Thesis , 2013.
- [28] D. M. N. a. M. G. J. W. R. Watson, *Assessment of 3D Codes for Predicting Liner Attenuation in Flow Ducts*, NASA Langley Research Center, Hampton, pp. 3-4.
- [29] COMSOL, "Tutorial: Computational Methods for Aeroacoustics," COMSOL , 2012. [Online]. Available: <http://www.bu.edu/ufmal/files/2011/08/tutorial.pdf>.
- [30] T. L. P. a. W. R. W. M. G. Jones, "Uncertainty and Sensitivity Analyses of a Two-Parameter Impedance Prediction Model," *AIAA*, May 2008.
- [31] A. F. A. C. a. J. S. L. Kinsler, *Fundamentals of Acoustics*, Fourth Edition, John Wiley & Sons, Inc. , 1999.
- [32] COMSOL, "Optimization Module," COMSOL , 2015. [Online]. Available: <http://www.comsol.com/optimization-module> . [Accessed 2014-2015].

- [33] USNA, "Transmission Loss," [Online]. Available: <http://www.usna.edu/Users/physics/ejtuchol/documents/SP411/Chapter10.pdf>.
- [34] B. Beck, "Grazing incidence modeling of a metamaterial-inspired dual-resonance acoustic liner," *SPIE Proceedings*, vol. 9064, p. 10, 2014.
- [35] W. R. W. a. D. M. N. M. G. Jones, "Effects of Flow Profile on Educued Acoustic Liner Impedance," in *AIAA*, Hampton .
- [36] J. Kemp, "Multimodal Propagation," 2003.
- [37] W. R. W. a. M. G. Jones, *Evaluation of Wall Boundary Conditions for Impedance Eduction Using a Dual-Source Method*, Hampton: 33rd AIAA Aeroacoustics Conference , 2012.
- [38] M. J. F. L. Todd Schultz, *A Comparison Study of Normal-Incidence Acoustic Impedance Measurements of a Perforate Liner*, Hampton , Virginia: NASA Langley Research Cetner.
- [39] S. M. a. J. D. Edlredge, *Acoustic Modeling of Perforated Plates with Bias Flow for Large-Eddy Simulations*, Los Angeles: Elsevier, 2009.
- [40] T. U. N. S. Wales, "Acoustic Impedance," [Online]. Available: <http://newt.phys.unsw.edu.au/jw/z.html>. [Accessed August 2014].
- [41] M. G. J. a. B. M. Howerton, *Evaluation of Parallel-Element, Variable Impedance, Broadband Acoustic Liner Concepts*, NASA Langley Research Center, Hampton.
- [42] COMSOL, "Biot Poroelasticity," COMSOL , 2013. [Online]. Available: [https://www.comsol.com/model/download/178623/models.ssf.biot\\_poroelasticity.pdf](https://www.comsol.com/model/download/178623/models.ssf.biot_poroelasticity.pdf).
- [43] J. L. a. A. S. David Herrin, "Properties and Applications of Microperforated Panels," Lexington, Kentucky .
- [44] E. J. R. a. L. H. L. J. Heidelberg, *Experimental Evaluation of a Spinning-Mode Acoustic Treatment Design Concept for Aircraft Inlets*, NASA Technical Paper 1613, 1980.
- [45] C. M. a. S. Carbonne, *Acoustic Impedance Measurement with Grazing Flow*, Maastricht, Netherlands: AIAA, 2001.

▼ Optimization Solver

Method:

Optimality tolerance:

Maximum number of objective evaluations:

Maximum number of simultaneous objective evaluations:

▼ Objective Function + ▼ ▶ ▼

▶▶ Expression	Description	Evaluate for
comp1.aveop9(acpr.ly)		Frequency Domain {freq} ▼
		Frequency Domain {freq} ▼

↑ ↓ ☰

Type:

Multiple objectives:

Solution:

▼ Control Variables and Parameters

▶▶ Parameter name	Initial value	Scale	Lower bound	Upper bound
<input type="text" value="location"/>	-1.4[in]	0.1	-2.6[in]	-1[in]

**Figure 111.** COMSOL interface of optimization solver